A NUMERICAL HYDRODYNAMIC STUDY OF COALESCENCE IN HEAD-ON COLLISIONS OF IDENTICAL STARS

F. G. P. SEIDL
Programming Methods, Inc., New York, N.Y., U.S.A.
and
A. G. W. CAMERON
Belfer Graduate School of Science, Yeshiva University, New York, N.Y., U.S.A.
and
Goddard Institute for Space Studies, NASA, New York, N.Y., U.S.A.

(Received 24 November 1970; in revised form 14 July, 1971)

Abstract. A two-dimensional hydrodynamic code has been developed for numerical studies of stellar collisions. The motivation for the study has been the suggestion by Colgate that collisions among stars in a dense galactic core can lead to growth of stellar masses by coalescence and thus to an enhanced rate of supernova activity. The specific results reported here refer to head-on collisions between identical polytropes of index 3 having solar mass and radius. If the polytropes were initially at rest at infinity, then about five percent of the combined mass is lost by ejection following collision. The volatilized mass fraction rises to about 18% for an initial relative collision velocity of 1000 km s^{-1} at infinite separation, and to about 60% for the 2000 km s^{-1} case. Since the initial kinetic and gravitational energies balance for a relative velocity of 1512 km s^{-1} at infinity, it may be seen that net coalescence persists to velocities somewhat in excess of this figure. Mass ejection takes place in two ways simultaneously: (1) by a rapid sideward expulsion of fluid in a massive lateral sheet normal to the collision axis, and (2) as a result of two recoil shocks which lead momentum flows backwards along this axis. The lateral effect has similarities to the expansion of gas into a vacuum; that is, shocks are not involved. However, the ejection of material from the rear colliding hemisphere due to the recoil shocks predominates at low collision velocities. As the velocity increases, both effects strengthen, but the lateral expulsion intensifies more rapidly than the recoil shocks.

1. Introduction

Until lately, there has been very little theoretical investigation of the physics of stellar collisions. This may be attributable to the complexity of the hydrodynamics involved. However, it is probably also partly due to the realization that stellar collisions within our own galaxy must be exceedingly rare. More recently, it has been realized that stellar collisions may be responsible, though indirectly, for very energetic processes that are sometimes observed in association with distant galaxies and quasars. Very strong radio galaxies are usually observed to have extremely bright point-like centers, where the density of stars must be extremely high. Similarly, high densities seem to exist in quasars, which appear to have masses of galactic order associated with volumes having radii of at most a few parsecs. This mass may be present mostly as stars in the general range of one solar mass with a smaller amount of associated interstellar gas of relatively high density.

Astrophysics and Space Science **15** (1972) 44–128.

In such dense systems, stellar collisions must occur frequently. It has been suggested by Woltjer (1964), Gold *et al.* (1965), and by Spitzer and Saslaw (1966), that stellar collisions may be the principal sources of energy input required to account for the tremendous energy emissions from strong radio sources and from quasars. In these cases it was suggested that the stellar system was sufficiently dense and massive so that the collisions would occur at a very high velocity and hence, be essentially disruptive. The high stellar velocities would result from the very deep gravitational potential well in which the stars move, the basic source of energy to the system being gravitational in origin. On the other hand, Colgate (1967) has pointed out that an equally high energy input may be obtained from many fewer collisions in less dense stellar systems, where the impact velocities are much slower so that the collisions are most often amalgamative. In this case the collision products would tend to build up large masses ($\sim 50\ M_\odot$) through successive coalescence.

The basis for Colgate's theory is the assumption that the dense stellar system is, in fact, the core of a larger system which has evolved with the production of a density-distribution cusp at the center. Such evolution takes place through relatively close stellar encounters which redistribute the energies and momenta of the stars in the system, feeding some of them towards the center where eventually they will be destroyed by collisions. However, Colgate envisions a different end point; viz., before the stars attain kinetic energies sufficient to disrupt one another, they undergo collisions which instead lead to coalescence. Under conditions where typical stellar velocities are estimated to be ~ 800 km s^{-1}, he has imagined that a collision between two stars of roughly solar mass should be highly inelastic, leaving more than 50% of the combined mass in a single final object. As stars evolve inward in the stellar system, they will be largely engulfed in such amalgamative collisions before the stellar density at the center of the system becomes high enough for the local stellar velocities to reach the disruptive range. Thus, stars of roughly solar mass may coalesce into larger bodies, say of the order of 50 solar masses, which then evolve quickly to the supernova state and shortly thereafter release great quantities of energy.

This paper presents some initial calculations designed to clarify the question of coalescence resulting from a stellar collision. The intent has been not only to determine the coalescent mass fraction as a function of initial approach velocity, but also to uncover physical characteristics of the collision process with a view towards gaining additional insight into the hydrodynamics involved. Recently, numerical capabilities have been developed which allow head-on collisions of stellar bodies to be handled within the framework of multi-dimensional hydrodynamics. Careful treatment has been necessary since stars are self-gravitating bodies with free-moving boundaries and include many orders of magnitude of density change between center and photosphere. Moreover, the gaseous stellar configurations undergo extreme distortions during a collision process; so, it seemed natural to use an Eulerian rather than Lagrangian representation. This means that a stellar model together with its large density gradients must be able to move during the calculations across an Eulerian finite-difference network without developing appreciable spurious distortions. The

problem becomes much more tractable when limited to head-on collisions between identical stars; the symmetry thereby introduced enables the basically three-dimensional spatial problem to be handled by only two independent space variables.

A previous attempt to calculate the effects of relatively slow head-on collisions between identical solar-type stars has been made by Mathis (1967). Because of practical limitations, he was unable to adopt a fully two-dimensional approach, but introduced an approximation in which the forward and lateral motions of fluid were decoupled to some extent. The collisions were imagined to take place between a largely unperturbed star and an immovable rigid plane, the plane of mirror symmetry normal to the collision axis of the colliding stars. A typical star was sliced by planes that were passed through it parallel to the mirror. Stellar gas between any two successive planes was in the form of a disk, which could approach or recede from the mirror and simultaneously expand laterally, but only in a way that the disk did not bend. Using this model, Mathis carried out one-dimensional hydrodynamic calculations of fluid motions along the direction of collision, and coupled these to one-dimensional motions perpendicular to the collision axis. Certain results of his highly approximate treatment agree with our own calculations. In particular, when the colliding stars started from rest at infinite separation, Mathis found that roughly 7% of the total mass escaped from the system following the collision. Moreover, relatively little sideward expansion occurred, most of the ejected material being thrown back along the collision axis. Another interesting result – somewhat to be expected – is that the effects of collision-enhanced nuclear burning and radiation flux were found to be relatively small.

In another series of investigations involving stellar collisions, Sanders (1970) as well as Spitzer and Saslaw (1966) have made rough estimates of mass loss per collision including off-axis collisions between stars of unequal mass. Although ingenious, these estimates made use of certain simplified models proposed by Spitzer and Saslaw (1966) which are even more approximate than that introduced by Mathis.

Collisions at much higher relative velocities have been discussed by De Young and Axford (1967) and by De Young (1968). Here gravitational effects were neglected; and, the ensuing collisions were completely disruptive. Extremely high ejection velocities following collisions were achieved, particularly back along the collision axis. However, their objectives were totally different than ours, being rather to study the possibility of producing relativistic ejecta.

In this paper we first give a brief account of our model and the numerical method for handling it; details of the method are relegated to the Appendix. We then consider a series of computer runs on head-on stellar collisions using three different initial collision velocities (*zero*, 1000 km s^{-1}, and 2000 km s^{-1} relative velocities at infinite separation); and, the results are displayed in proper time sequence by means of machine-generated pictures. From these we are able to gain some insight into the hydrodynamic mechanism of the collision process. Finally, the main results are presented: the mass fraction at three different collision velocities that escapes from

the gravitational field of a final object. Some remarks about the convergence of the numerical method appear in the Appendix as well as a detailed discussion of the computational errors.

2. Method

Considerable attention was given to the numerical method although only an approximate model was assumed for the colliding stars. Such emphasis seemed justifiable because certain features of the difference scheme were new, and subtle errors are sometimes obscure in nonlinear numerical calculations. On the other hand, the errors introduced through use of standard approximate stellar models are widely recognized.

Prior to collision, the stars were assumed to be polytropes of index 3.0; but, as the collision process proceeded, all changes were imagined to take place according to the equation of state for an ideal gas, i.e.

$$\varrho E = P/(\gamma - 1), \tag{1}$$

where ϱ denotes fluid density, E internal energy per unit mass, P total pressure, and γ the effective ratio of specific heats, which was set equal to $\frac{5}{3}$. Equation (1) is a sensible approximation when the gas pressure greatly exceeds the radiation pressure, as in the Sun.

Polytropes comprise a family of self-gravitating spherical fluid masses in hydrostatic equilibrium (Chandrasekhar, 1939) where pressure P is simply related to ϱ [i.e., $P=K\varrho^{(n+1)/n}$, n being the index]. Those of index 3.0 have been widely used to approximate stars in which energy transport is due mainly to radiation, a condition largely valid for the Sun. It was convenient in our case to normalize the model by setting its radius and mass equal to that of the sun, the values for $R_\odot$ and $M_\odot$ being taken from Allen (1963), viz., $R_\odot = 6.9598 \times 10^{+10}$ cm and $M_\odot = 1.989 \times 10^{33}$ g. Then, assuming the gravitational constant to be $G = 6.668 \times 10^{-8}$ dyn-cm^2 g^{-2}, it followed from well-known relations (Chandrasekhar, 1939) that the central density and central pressure for the normalized polytrope of index 3.0 are $\varrho_c = 76.3$ g cm^{-3} and $P_c = 1.242 \times 10^{17}$ dyn cm^{-2} respectively. These values are somewhat less than the density and pressure currently believed to exist at the center of the sun. The gravitational binding energy of the normalized polytrope is also readily attainable and turned out to be $5.685 \times 10^{+48}$ erg, as compared to some 7.4×10^{48} erg for the Sun.

The initial configuration (or machine-zero configuration) involved two identical polytropes approaching each other head-on at a prescribed velocity. Obviously the system had a high degree of symmetry which persisted throughout a calculation. The principal symmetry, of course, lay about the line of approach; but, there was also a central lateral plane of symmetry perpendicular to this axis at the center of mass of the system. Because of the axial symmetry, it was appropriate to use cylindrical coordinates r and z, the z-axis coinciding with the line of approach and r being measured normal to this axis. Due to the additional symmetry about the central

lateral plane, only one quadrant of the physical space had to be handled formally, where the actual physical space considered was a cylindrical region symmetric about the z-axis and of height equal to diameter – either 6.4 $R_\odot$ by 6.4 $R_\odot$ or 12.8 $R_\odot$ by 12.8 $R_\odot$ depending upon the number of finite-difference steps per $R_\odot$. Incidentally, the initial configuration afforded an opportunity to test the accuracy of the numerical calculations for gravitational potential (cf. Figures 2A and 3A of the Appendix), since at any point the field produced by two or more *undeformed* polytropes can be calculated from exact equations (Chandrasekhar, 1939).

The numerical calculations were carried out on the IBM 360/95 computer at the Goddard Institute for Space Studies, New York. The machine program, summarized below, has been set up to handle initial-value problems which involve compressible self-gravitating fluids moving in three-dimensional space and subject to cylindrical symmetry. Eulerian coordinates are used. The fluids have free-moving boundaries and may evolve shocks; the latter must be allowed to play a role in stellar collisions. The difference formulas are based on local conservation of mass, momentum, and energy, and include an equation of state [Equation (1)]. They are developed to second-order accuracy in the small quantities Δr, Δz, Δt. The gravitational potential is obtained from a numerical analogue of the integral satisfying Poisson's equation; expressed in terms of cylindrical coordinates r, z, θ, and time t, the θ-dependence vanishes due to symmetry so that

$$\Phi(r, z, t) = G \int^{V(t)} \frac{\varrho(r', z', t)}{|\mathbf{r}(r', z') - \mathbf{r}(r, z)|} \, \mathrm{d}V(r', z', t), \tag{2}$$

where $\Phi(r, z, t)$ denotes the gravitational potential at the point r, z, t; and, $V(t)$ is the space including all non-zero values of the density $\varrho(r', z', t)$. Since the calculations are formally restricted to one quadrant, $\Phi(r, z, t)$ must be computed so as to yield the physically-correct field consistent with the complete model. Note that this integral method avoids any need for the explicit matching of Laplace and Poisson solutions at free-moving surface boundaries.

Free-moving boundaries, however, have caused difficulties, and at present are handled by a direct but approximate approach. Accordingly, the dependent variables are always calculated from the complete set of difference formulas; but, whenever the computed density ϱ at an arbitrary point falls below a certain small value, all dependent variables including ϱ are immediately set to zero at that point. If the ϱ cutoff is sufficiently small (e.g., 10^{-6} of the initial central density of a stellar model), negligible loss in mass results and only a slight depreciation in energy. Since the procedure allows considerable freedom of motion, spurious fluctuations often appear at the leading and trailing edges of moving boundaries where the density is both very small and changing rapidly. However, such fluctuations can be suppressed by means of artificial dissipation.

Two types of artificial dissipation are used: (1) The first type (flow-bias) affects values of the flow terms in the difference analogue of the divergence and slightly

modifies their values in the direction of upstream values, the amount of change being proportional both to the local fluid velocity and the time step Δt. (2) The second type is an artificial viscosity consisting of two parts, one like that introduced by von Neumann and Richtmyer (1950), the other similar to certain third-order terms proposed by Lax and Wendroff (1960). When suitably applied, all artificial dissipation is very small except (1) around shock fronts, (2) about large fluctuations, and (3) at the center of impact during compression. Besides damping spurious fluctuations, the artificial viscosity acts to induce very nearly the correct entropy jump across numerically simulated shocks. More is said about this last effect in a paper by von Neumann and Richtmyer (1950).

At prescribed intervals, the mass and total energy are summed over all netpoints. These sums do not enter directly into the difference calculations but serve as a control on the running of the program; i.e., a run is automatically terminated whenever either the overall mass or overall energy differs from its initial value by more than a certain percent. Both (1) the conservation of mass and (2) the conservation of energy in the large are necessary for the correctness of our calculations as well as for numerical stability. Conservation of mass generally remains very precise since the finite-difference scheme itself satisfies this exactly – except for a trivial mass loss at moving boundaries due to the density cutoff. Conservation of total energy is less precise; but, it often can be improved by small adjustments of the constant factors in the expressions for the flow-bias [cf. Equations (A35) and (A39), Appendix]. Such adjustments have been made whenever considerable changes were introduced in the starting conditions, as the three widely different initial collision velocities, or in the Courant factor $\dagger$ relating the time steps Δt and the mesh width $\Delta r = \Delta z = h$ [cf. Equation (A70), Appendix]. This procedure is a bit disturbing in that just sufficient artificial dissipation, including flow-bias, should be added to control spurious fluctuations at the moving boundaries and during maximum impact but not enough to appreciably affect the course of a calculation. However, despite the need for readjustment, the current form of flow-bias apparently caused little error in our principal numerical results (cf. Section 8 of the Appendix).

Besides total mass and energy, another quantity is determined at prescribed intervals; this is the *volatile mass*, a measure of the total material having sufficient local energy to escape gravitational binding. The volatile mass is calculated at an arbitrary time by summing all mass elements whose *outgoing* kinetic energy plus internal energy exceed their gravitational energy. The process is handled in the difference program as follows: Let u and w denote respectively the r and z components of fluid velocity, ϱ the fluid density, and T the *outgoing* kinetic energy. The spatial net-points are identified by the indices i, j, and the time steps by a superscript n ($n = 1, 2, \cdots$); e.g., in difference notation the equation for internal energy per unit volume at the point r_i, z_j, t^n becomes [cf. Equation (1)]

$$(\varrho E)^n_{i,j} = P^n_{i,j}/(\gamma - 1). \tag{3}$$

The machine instructions which determine the *outgoing* kinetic energy $T^n_{i,j}$ at the

space point r_i, z_j for time $t=t^n$ are equivalent to the formula

$$T^n_{i,j} = \begin{cases} 0 \quad \text{if} \quad u^n_{i,j} < 0 \\ 0 \quad \text{if} \quad w^n_{i,j} < 0 \\ \varrho^n_{i,j}[(u^n_{i,j})^2 + (w^n_{i,j})^2]/2, \ \text{otherwise}. \end{cases} \tag{4}$$

If $\Delta V_{i,j}$ denotes the finite-difference volume element properly associated with the netpoint i, j [cf. Equation (A27), Appendix] and $\Phi^n_{i,j}$ the gravitational potential at the nth time step, then a mass element $\varrho^n_{i,j}\Delta V_{i,j}$ is stored as a volatile mass element labeled $(\varrho_{i,j}\Delta V_{i,j})^*$, whenever

$$T^n_{i,j} + P^n_{i,j}/(\gamma - 1) > \varrho^n_{i,j}\Phi^n_{i,j} \tag{5}$$

otherwise, $(\varrho_{i,j}\Delta V_{i,j})^*$ is set to *zero*. Hence, the volatile mass M^n_v at a time corresponding, say to the nth time step is given by

$$M^n_v = 2\pi \sum_{i,j} (\varrho^n_{i,j}\Delta V_{i,j})^* \tag{6}$$

while, the total mass M^n, which should remain constant for all n, can be written

$$M^n = 2\pi \sum_{i,j} \varrho^n_{i,j}\Delta V_{i,j}, \tag{7}$$

During a typical collision calculation, M^n_v was found to stay essentially zero until some time after maximum impact when it increased rapidly at first, later more slowly, approaching and leveling off at a value which thereafter remained largely constant (cf., Figures 12, 13, and 14). The leveling-off value, M^∞_v, is a measure of the mass which escapes gravitational binding; the ratio

$$F = M^\infty_v/M^n \tag{8}$$

might be called the mass-escape fraction. The principal objective of the present study was to investigate this mass-escape fraction F as a function of the initial approach velocity in head-on collisions.

A test which the difference program must satisfy in order to be correct is discussed in Section 7 of the Appendix. In addition, checks on the gravitational-field routine are described at the end of Section 5 of the Appendix.

In order to display calculated results, two types of machine generated pictures are employed. The first type exhibits full configurations and density distributions at preset intervals during the course of a calculation. Two levels of shading are introduced thereby allowing the representation of gravitationally bound and unbound regions of fluid. Darker regions are gravitationally bound, lighter regions are volatile. The density distributions are indicated by means of contour lines connecting points of equal density; viz., $\varrho/\varrho_c = 1.0$, 0.5, 0.1, 0.01, and 0.001, ϱ_c being the central density of the undistorted stellar model. A final density contour is, in fact, formed by the outer boundaries where the shading ends and ϱ/ϱ_c equals the density cutoff, usually 10^{-6}.

The second type of display exhibits the fluid-velocity field. Arrows are generated at evenly-spaced points over only one quadrant of the cylindrically symmetric flow. Each arrow is a scaled-down velocity vector, being proportional to the fluid velocity at the point from which it stems and pointing in the direction of the flow. Here again density contours and two levels of shading are used.

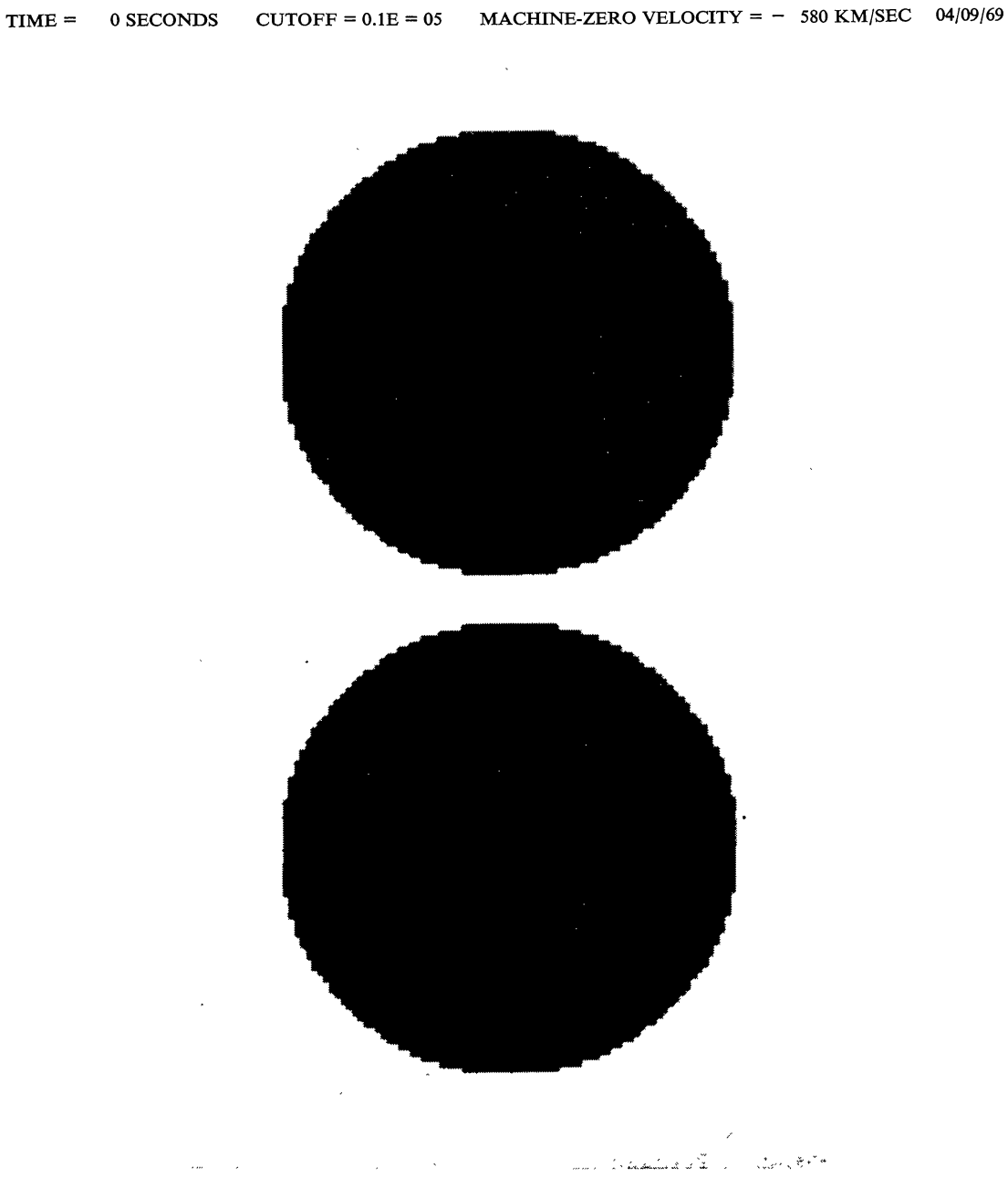

Fig. 1a. Machine-zero configuration showing contours of equal density. Here the contours for $\varrho/\varrho_c = 1.0$ are merely points at the centers of each object. Proceeding outwards $\varrho/\varrho_c = 0.5$, 0.1, 0.01, 0.001, and along the outer boundaries $\varrho/\varrho_c = 10^{-6}$. Note that this and the following configurations are rotationally symmetric around the vertical axis. ϱ_c denotes the initial central density.

3. The Collision Process Numerically Represented

Head-on collisions were investigated for three initial velocities of approach: (1) zero, (2) 1000 km s^{-1}, and (3) 2000 km s^{-1} as measured center-to-center at infinite separation. Incidentally, the kinetic energy of two colliding polytropes at infinite separation equals the sum of their gravitational binding energies if their relative initial velocity is 1512 km s^{-1}.

Figures 1a through 1f illustrate the collision process in the center-of-mass frame for an initial relative approach velocity of 1000 km s^{-1}. The collision axis is vertical. Figure 1a shows the machine-zero configuration, viz., two *undistorted* polytropes separated by 2.2 $R_\odot$ and approaching each other with velocities of 580.2 km s^{-1} relative to their common center of mass. Gravitational distortion at a separation of 2.2 $R_\odot$ or more has been neglected. The real time elapsed between Figure 1a and 1f is about 40 min. Near the point of maximum impact (the configuration of Figure

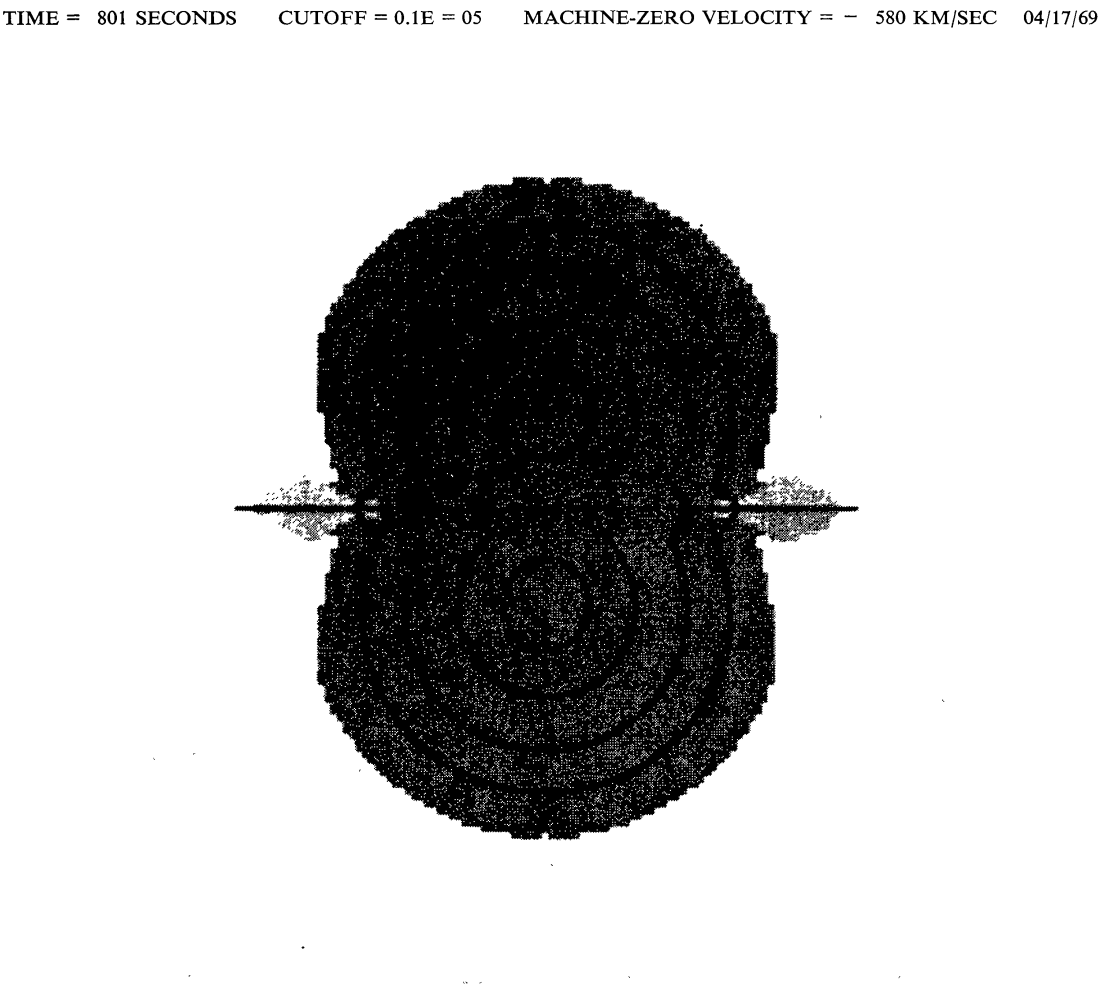

Fig. 1b. Early stage of a head-on collision involving an initial relative velocity of 1000 km s^{-1} at infinite separation. The lateral sheet of ejected fluid (shaded light) has begun to form. Regions shaded lightly are capable of gravitational escape.

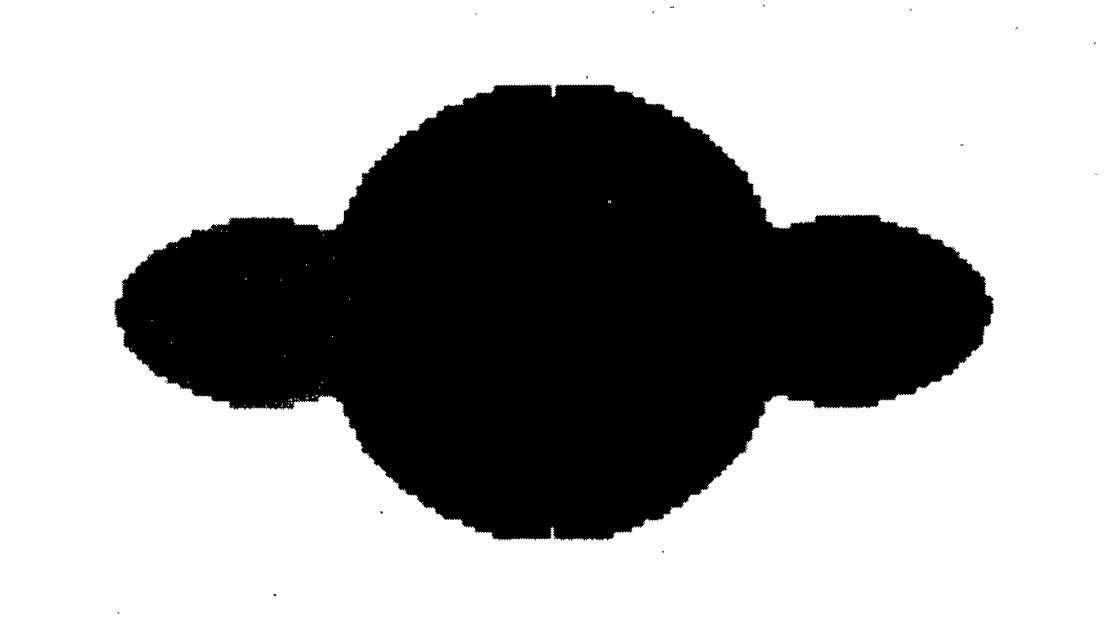

Fig. 1c. Maximum compression in the course of a head-on collision between solar-like polytropes initially approaching at 1000 km s^{-1}. The innermost density contour (viz., $\varrho/\varrho_c = 1.0$) encloses a spheroidal region where density and temperature exceed initial values at the centers of the stellar models.

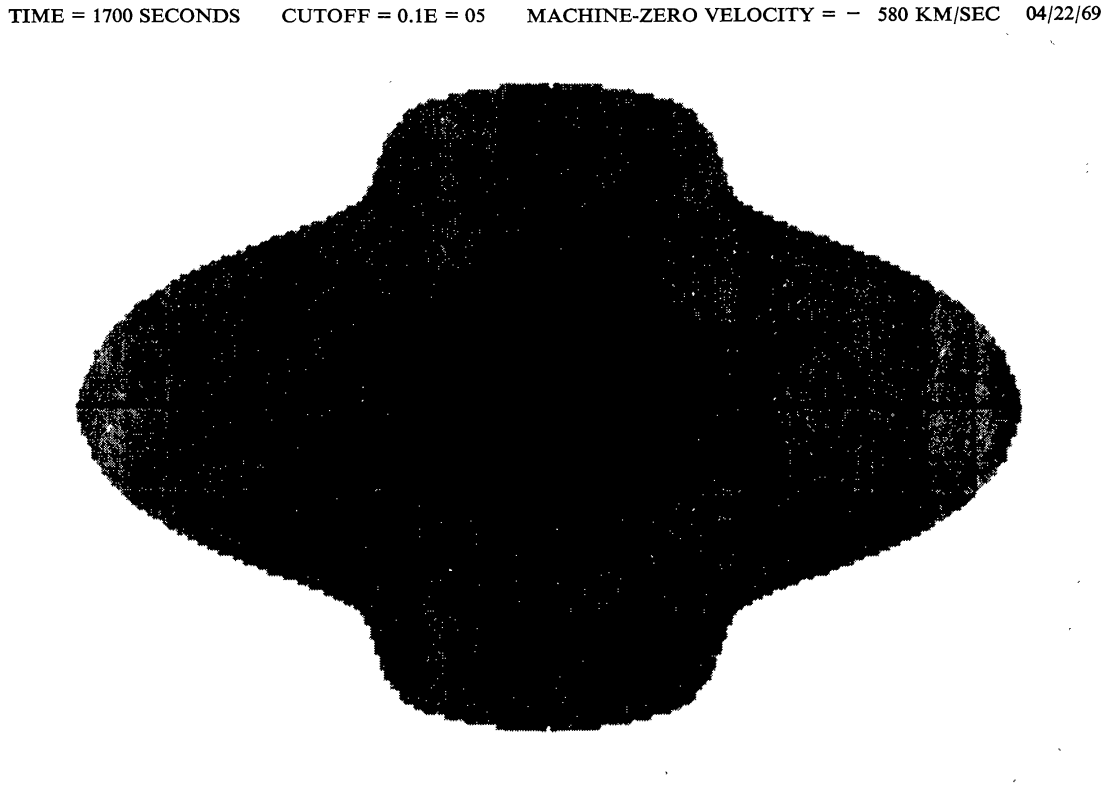

Fig. 1d. Unloading phase soon after the two recoil shocks have broken through the upper and lower surfaces (1000-km s^{-1} case). The density contours correspond to $\varrho/\varrho_c = 0.1$, 0.01, and 0.001, while, as in all these pictures, $\varrho/\varrho_c = 10^{-6}$ along the outer surface. Gravitationally escaping material is shaded lightly.

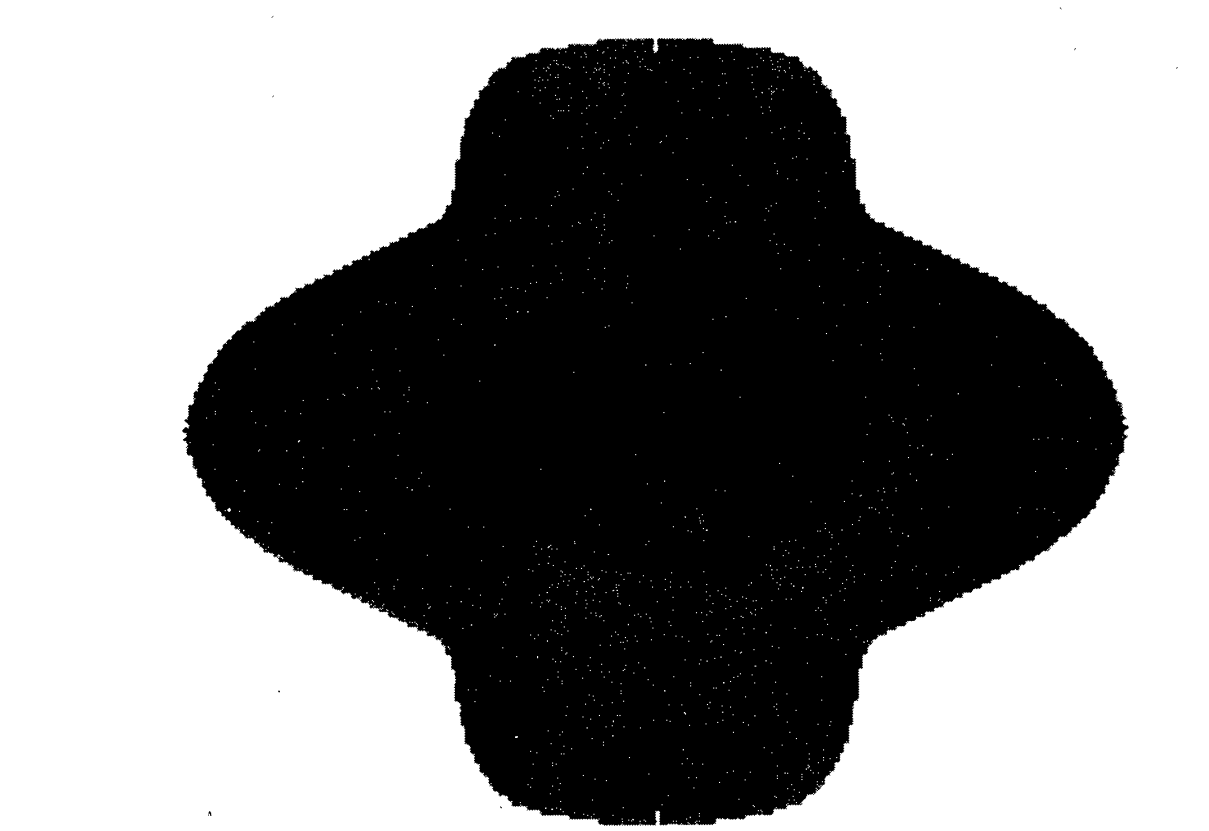

Fig. 1e. Appearance of characteristic shapes, viz., (1) upper and lower prominence due to effects of the two recoil shocks and (2) an extensive equatorial bulge caused by the lateral ejection of fluid (1000-km s^{-1} case).

1c) the fluid density exceeds the initial central stellar density ϱ_c throughout the oblate region bounded by the density contour $\varrho/\varrho_c = 1$; and, the temperature is appreciably higher here than the initial central stellar temperature (cf. Figure 4).

Figures 2 and 3 compare configuration changes due to different initial approach velocities. At machine zero, the separations were 2.2 $R_\odot$ and the velocities (1) 294.3 km s^{-1} and (2) 1042.4 km s^{-1} relative to the center of mass of the system; these velocities correspond respectively to *zero* and 2000 km s^{-1} center-to-center at infinite separation. The increase in lateral ejection of fluid with collision velocity is remarkable. This lateral fluid sheet is reminiscent of the behavior found when a liquid drop splashes against a rigid plane (Harlow and Shannon, 1967). The amount of compression at maximum impact likewise intensifies with approach velocity, as may be seen by examining the innermost density contours. Figure 3 contrasts configurations resulting from low and high-velocity collisions at times appreciably after maximum impact. The configuration of Figure 3a represents the state of the low-velocity collision 3668 s in real time after machine-zero; that of Figure 3b exhibits the high-velocity collision 1450 s following machine-zero, the shorter time interval demon-

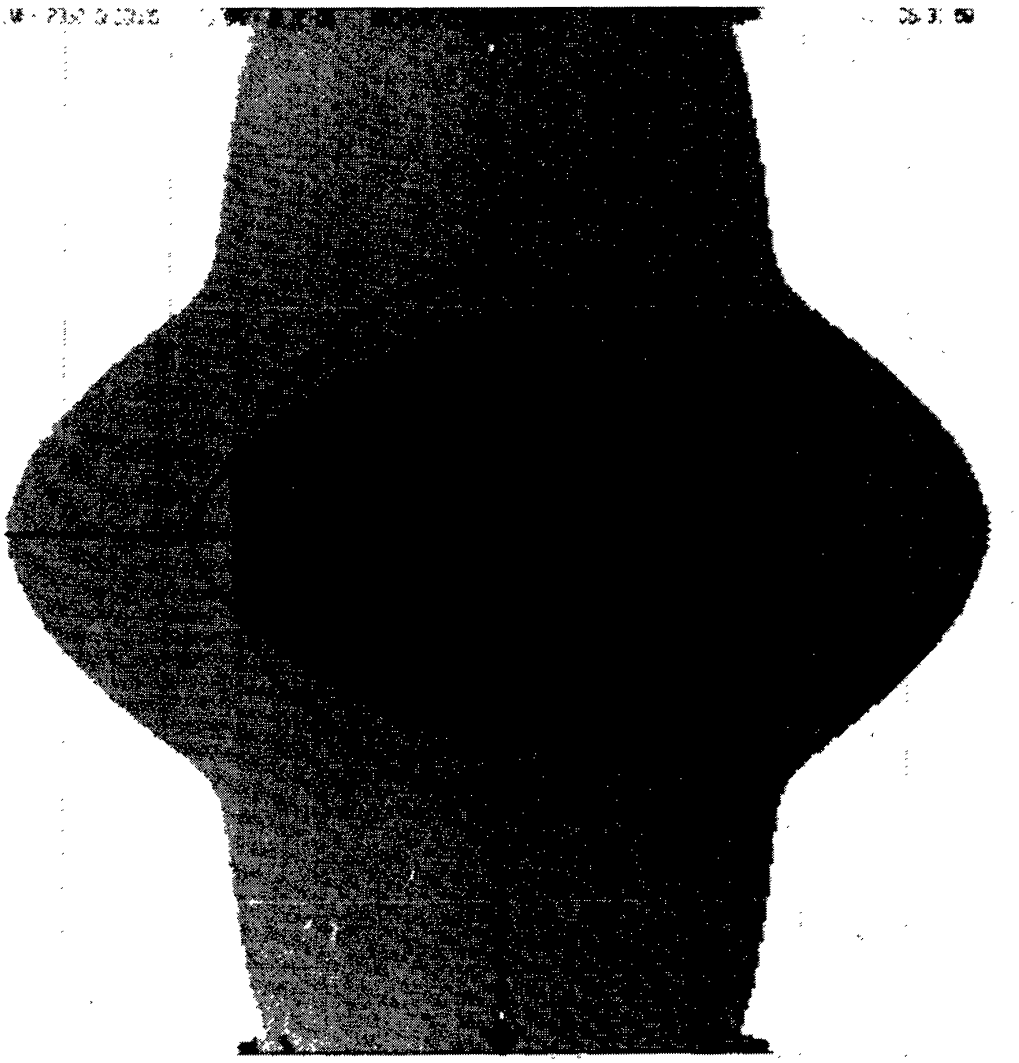

Fig. 1f. Growth of the prominences arising from the recoil shocks (1000-km s^{-1} case). The upper and lower extremities should trail off beyond the frame of the picture in a manner suggestive of plumes; however, the top and bottom edges indicate effects of the rigid boundary imposed on the domain of calculation. At this time some 18% of the total initial mass is calculated to be escaping from the gravitationally-bound central object.

strating a greater speed of interaction. Note that the density contours appearing in Figure 3b are for $\varrho/\varrho_c=0.01$ and 0.001 proceeding outwards from the center.

For the 1000 km s^{-1} collision process, the temperature and density at the center of impact are plotted in Figure 4 as a function of time over a period including maximum impact. The temperature was obtained from numerical values of P/ϱ by means of an equation of state [viz., $T=(P/\varrho)/(k/\mu H)$] corresponding to an early solar-type star whose core has undergone little hydrogen depletion. The numerical values came from a calculation using a mesh width of $h=R_\odot/40$. It should be noted that the temperature determination before the time 500 s is not physically significant as indicated by the absence from coarser-zoned runs of certain peaks shown here;

TIME = 1904 SECONDS CUTOFF = 0.1E = 05 MACHINE-ZERO VELOCITY = − 294 KM/SEC 01/03/69

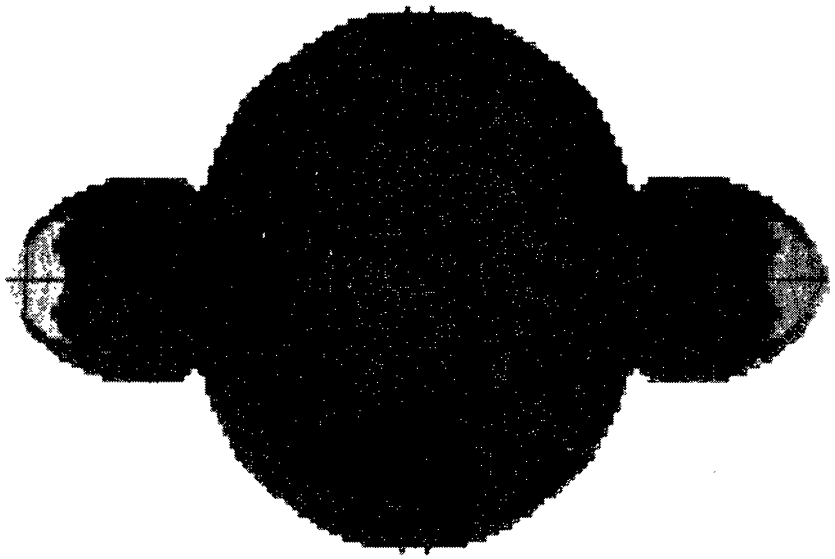

Fig. 2a. Configuration (rotationally symmetric) at maximum compression as calculated for a head-on collision between solar-like polytropes starting from *zero* relative velocity at infinite separation. Maximum velocities of lateral ejection are determined to be ~ 780 km s^{-1}.

TIME = 761 SECONDS CUTOFF = 0.1E = 05 MACHINE-ZERO VELOCITY = − 1042 KM/SEC 02/14/69

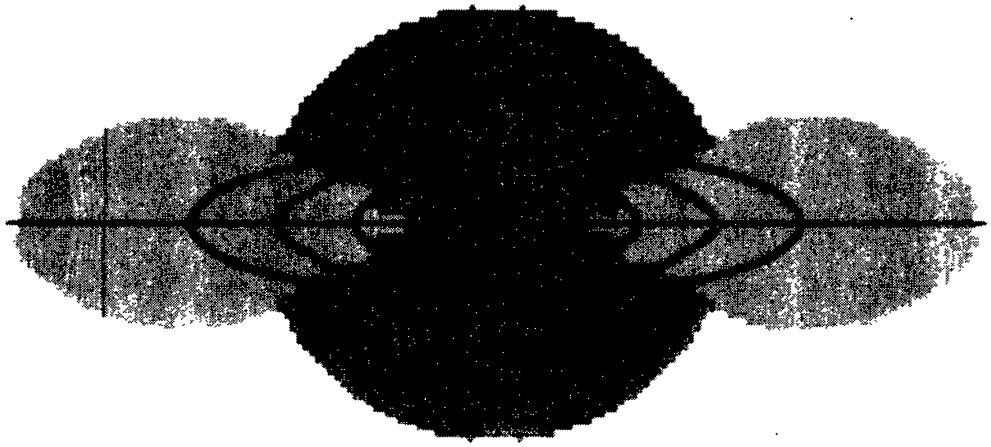

Fig. 2b. Configuration (rotationally symmetric) at maximum compression for a head-on collision involving two solar-type polytropes initially approaching one another at 2000 km s^{-1}. Here the maximum velocities of lateral ejection are calculated to be ~ 2500 km s^{-1}. Accompanying the higher lateral velocities, there is an extensive toroidal region where material is potentially capable of gravitational escape.

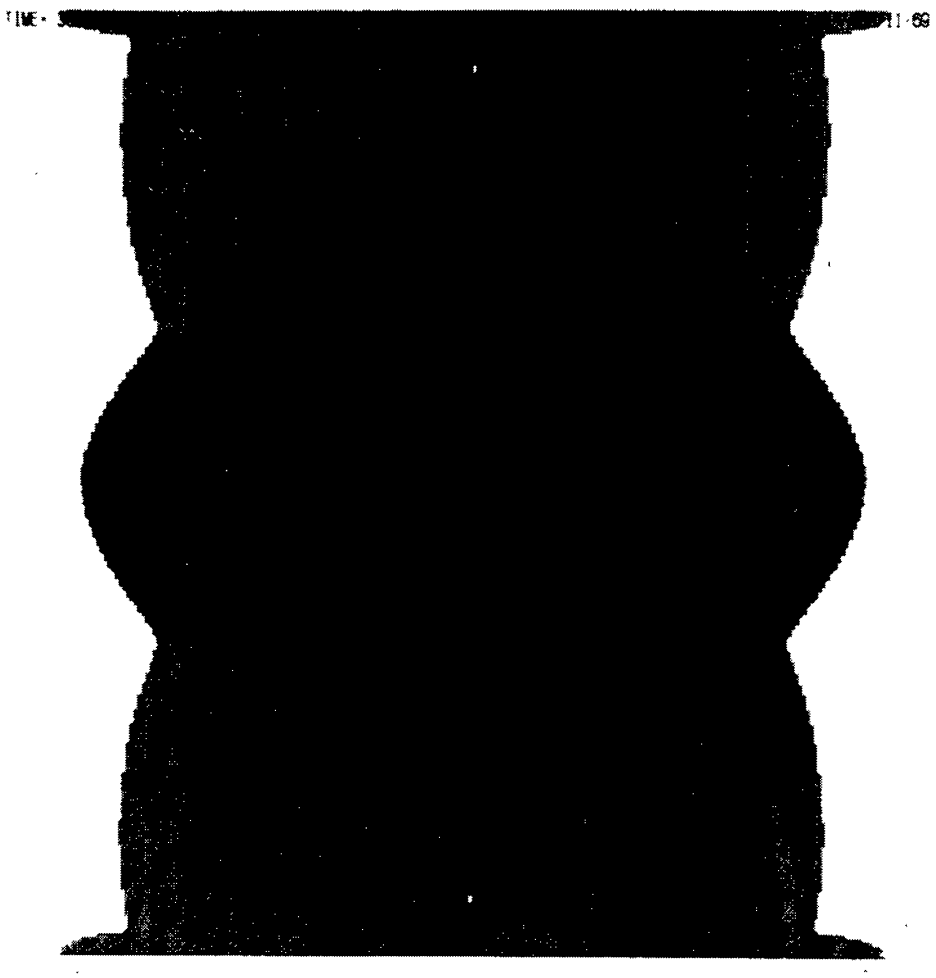

Fig. 3a. Last stage (rotationally symmetric) in the head-on collision of two solar-like polytropes nitially having *zero* relative velocity at infinite separation. Material escaping from the gravitationally-bound central object is shaded lightly, and is still streaming outwards through the upper and lower edges of the picture. Densities in this unbound region are of the order $\varrho_c \times 10^{-4}$ and velocities ~ 1000 km s^{-1}. The slight lateral spreading along the top and bottom edges is due to the artificial rigid boundary on the domain of calculation.

the latter are attributed to the action of artificial damping in regions of very low density. Extrapolation by the method described in Section 8 of the Appendix indicates that the temperature at center of impact reaches 52×10^6 K; but, the time interval during which temperature and density are appreciably elevated above central solar values is too short to sustain an increased release of nuclear energy comparable with the energy involved in the hydrodynamic interactions (cf. Mathis, 1967).

Changes in the fluid-velocity field and the shock fronts are displayed by the second type of machine-generated picture, Figures 5 through 8. Here the collision axis runs vertically along the lefthand edge of the picture, while the lateral plane of symmetry

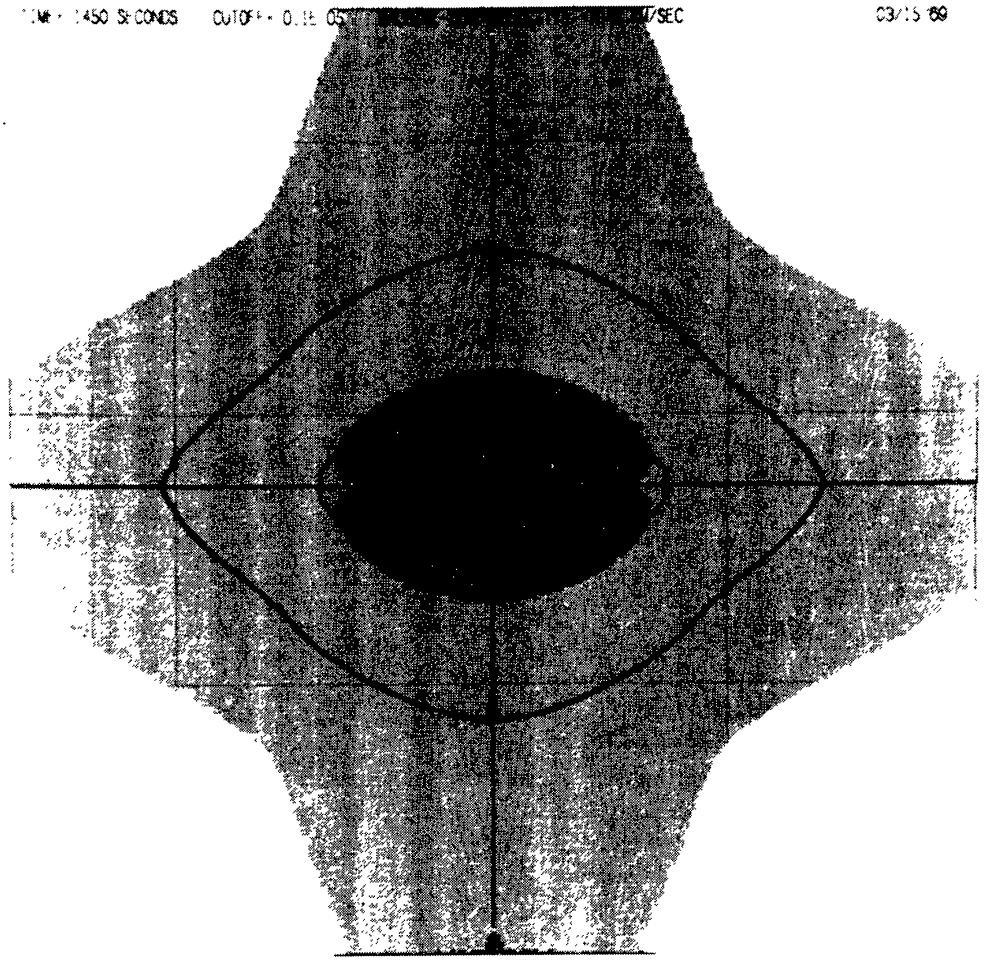

Fig. 3b. Late stage (rotationally symmetric) in the head-on collision between two solar-like polytropes initially closing at 2000 km s^{-1}. The lateral expulsion of fluid is much greater than for the case of zero initial collision velocity. Also, a much smaller gravitationally-bound remnant (shaded darker) is left behind.

forms the bottom edge. The fluid-velocity field is depicted by a field of small arrows drawn from every fourth netpoint; and, for velocity calibration a horizontal arrow of length denoting either 1000 km s^{-1}, 2000 km s^{-1}, or 5000 km s^{-1} is included in the upper righthand corner of each picture. All velocities are measured with respect to the center of mass of the system. The position and curvature of a shock front at any time is clearly discernible by means of a very narrow strip in which the velocity vectors abruptly change length and direction.

Summations of kinetic, internal, and total energy over all mass elements are plotted against time in Figures 9, 10, and 11 for the three initial approach velocities, the results being obtained from calculations using as mesh width $h = R_\odot/40$. The constancy of total energy is a necessary condition for the validity of a calculation, while

changes in total kinetic and internal energies are interesting aspects of the collision process. The peak in internal energy generally occurs just slightly before the minimum in kinetic energy, the lag of kinetic energy being attributed to the net deceleration of fluid still falling in after the highly compressed regions near the center of impact have begun to unload. Using the method of extrapolation described at the end of Section 8 in the Appendix, the peak internal energy for the 1000 km s^{-1} collision

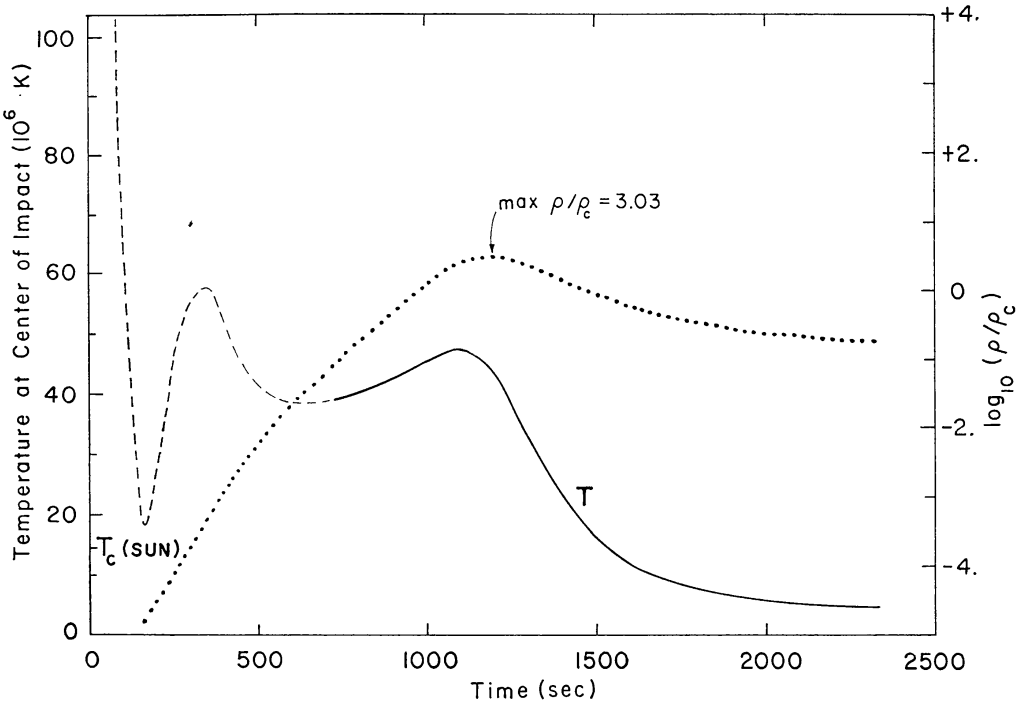

Fig. 4. Density and temperature *vs.* time at center of impact for a head-on collision between two solar-like polytropes initially closing at a relative velocity of 1000 km s^{-1}. ϱ_c denotes the initial central density. The dashed portion of the temperature plot is largely the result of intense artificial damping and is not physically significant.

(Figure 10) is estimated to reach $2.1^{+0.2}_{-0.0} \times 10^{+49}$ erg; this is $1.5 \times 10^{+49}$ erg more than the total initial internal energies of the two polytropes, and may be compared with twice the initial gravitational binding energy of a solar-type polytrope, viz., $1.14 \times 10^{+49}$ erg. Disruption does not occur, of course, because at maximum impact the gravitational binding energy has been sufficiently enhanced due to compression. Total energy, on the other hand, should remain constant with time although Figure 10 shows a slight fall-off for this run; at $t = 2275$ s or after 1840 machine steps, the total energy has dropped by an amount equal to 7% of the total initial internal energy. However, the discrepancy can be accounted for by the cumulative loss in kinetic energy accompanying the loss in mass caused by the density cutoff, which was introduced to handle the free-moving boundaries.

When two polytropes start to collide, sonic disturbances should propagate away from the regions which first make contact and travel back through the oncoming

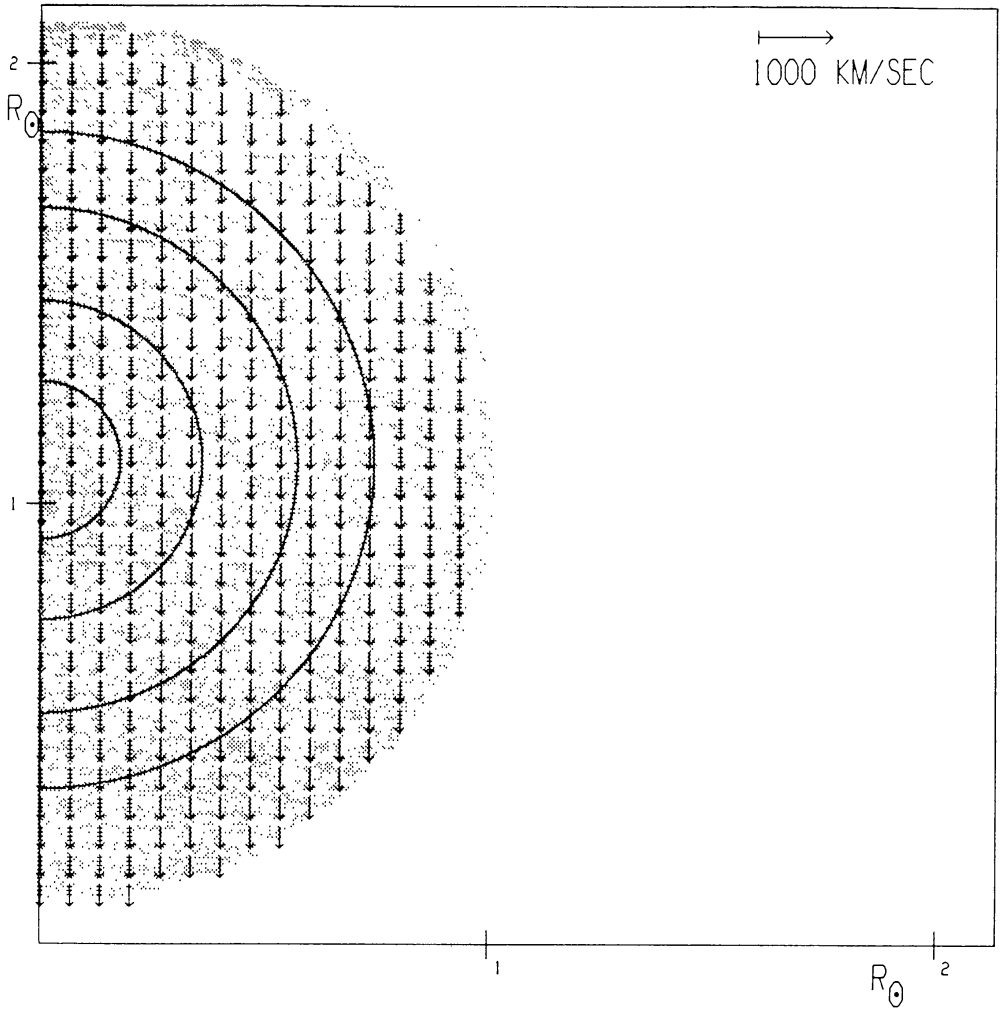

Fig. 5a. Head-on collision configuration at machine zero, viz., when two solar-like polytropes are 2.2 $R_\odot$ apart. The collision axis runs vertically, and only the upper righthand quadrant of the complete picture is shown. Fluid velocity is represented by a field of arrows, arrow length being calibrated by the horizontal arrow in the upper righthand corner.

fluid except that, in all cases considered here, the oncoming material is falling in supersonically with respect to the center of impact. More particularly, the local sound speed c decreases monotonically outwards along the radius of a solar-type polytrope of index 3.0 and $\gamma = \frac{5}{3}$ [cf. Equation (1)]; starting with a central maximum of $c = 521$ km s^{-1}, it drops to $c = 278$ km s^{-1} at a distance from the center of $R_\odot/2$, and to $c = 163$ km s^{-1} at 3 $R_\odot/4$, etc. In contrast, even for the lowest-velocity collision at the instant when the centers are 2.2 $R_\odot$ apart, the material velocity of each center is 294.3 km s^{-1} relative to the center of impact or center of mass of the system; and, shortly thereafter, higher velocities (e.g., $\gtrsim 400$ km s^{-1}) occur where the leading edges first touch and the sound speed is less than 163 km s^{-1}. Meanwhile, along the lateral plane of symmetry, which divides the system evenly at the center of impact, there is a sharp pressure build-up causing intense lateral acceleration of fluid in a

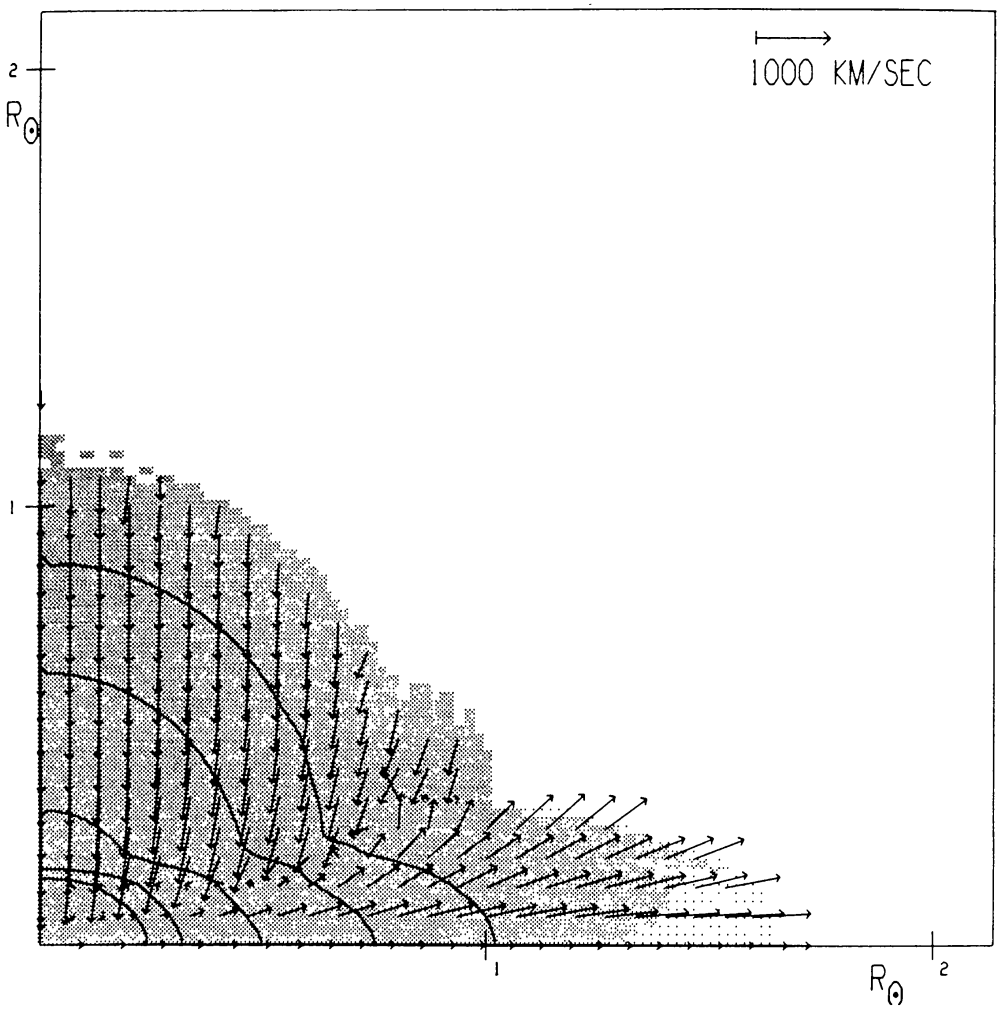

Fig. 5b. Configuration at the instant of maximum total *internal* energy for the case of a head-on collision starting from *zero* relative velocity at infinite separation. As calculated, this configuration occurs 31.9 min after that of Figure 5a. Heavy lines are density contours, viz., from the center out $\varrho/\varrho_c = 1.0$, 0.5, 0.1, 0.01, and 0.001. Sparsely dotted regions are where the local outgoing kinetic plus internal energies exceeds the gravitational energy.

way similar to the expansion of gas into a vacuum, no shocks being involved in this phenomenon (cf. Zel'dovich and Raizer, 1966; Sakurai, 1960; etc.). The lateral ejection of fluid assumes the form of a circular sheet of appreciable thickness; and, the outermost edges soon acquire outgoing velocities in excess of escape velocities (cf. Figures 1b and 1c).

While no sonic disturbances are able to travel upstream along the collision axis and no lateral shocks diverge from the center of impact in a direction normal to this axis, the pressure close to the lateral plane of symmetry very quickly reaches the point where it can produce two recoil shock fronts. These move away from the symmetry plane in opposite directions, one on either side, and propagate upstream against the fluid material still falling in on both directions along the collision axis.

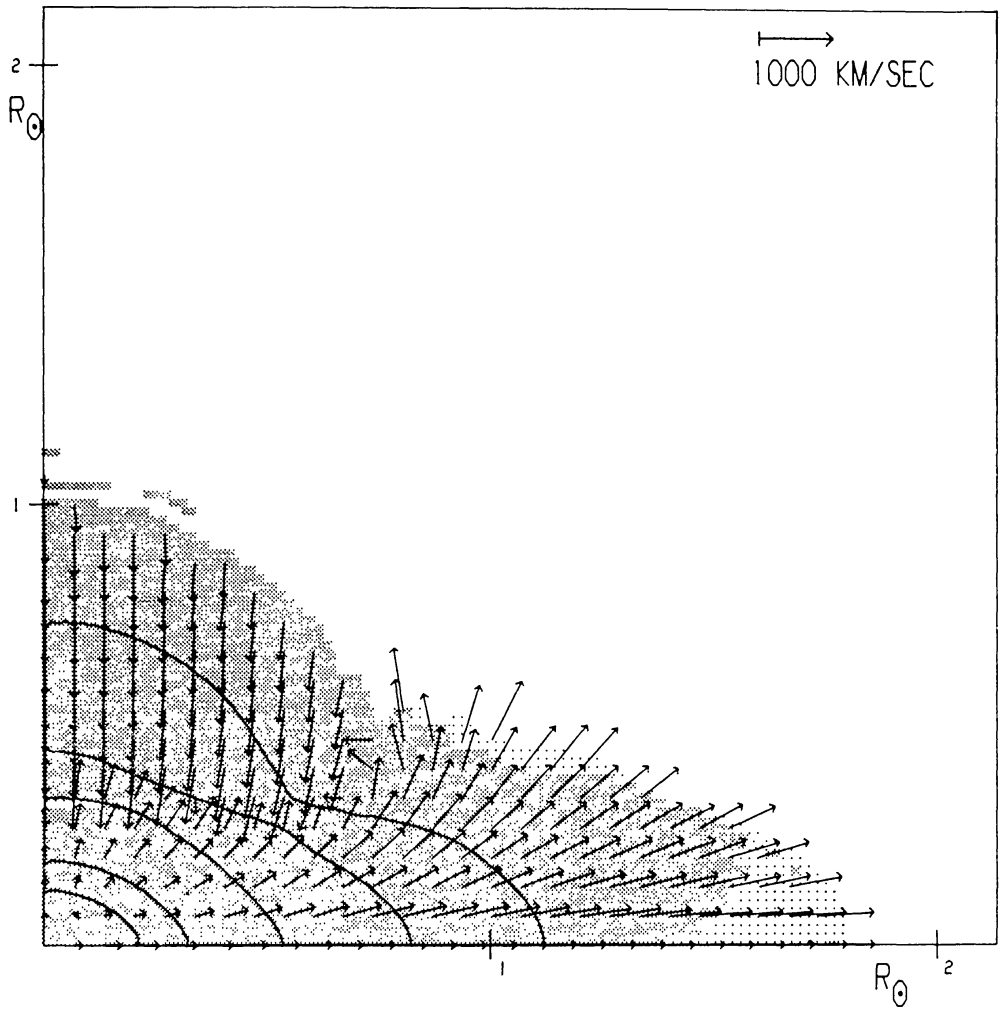

Fig. 5c. Configuration soon after maximum impact. The recoil shock front can be identified as the narrow region where the velocity arrows abruptly change direction. This and all other pictures in Figure 5 result from a calculation of the *zero* initial-velocity case using a mesh width of 60 steps per $R_\odot$.

The shock fronts tend to be formed parallel to the symmetry plane but immediately assume a concave shape when viewed from the unshocked regions. The concavity can be understood by realizing that shocks gain in strength as they propagate through material of decreasing density and vice versa (cf. p. 852ff., Zel'dovich and Raizer, 1967; Sakurai, 1960; etc.).

It can be seen from plots of fluid velocity *vs.* z for various r and at different times (such plots are not included here) that very soon after maximum compression all portions of the recoil shock fronts have traveled past the centers of the colliding polytropes which have merged at the center of impact. From this point on the fronts are free to propagate down negative density gradients, and consequently gain rapidly in strength. The jump in values across the shock fronts becomes most intense for material furthest from the center of impact; yet, all along unshocked material is not

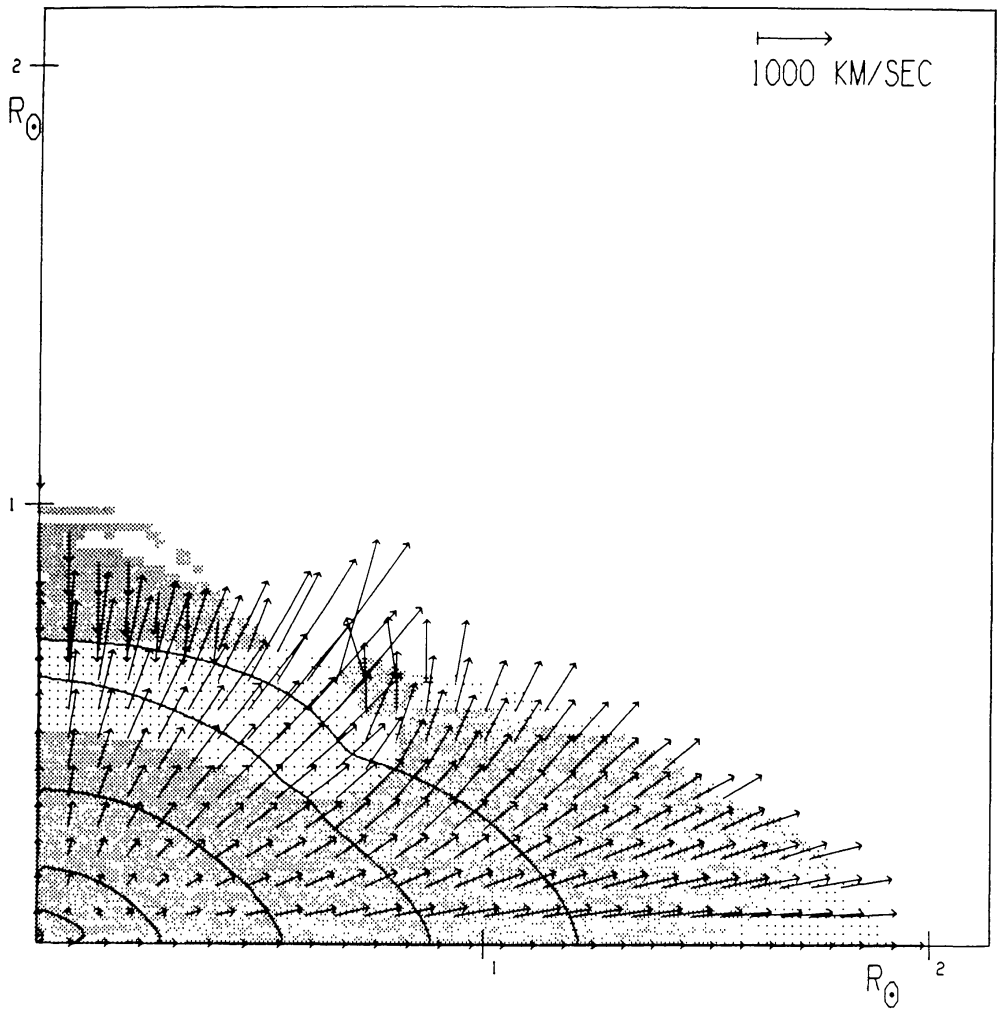

Fig. 5d. Here the recoil shock is shown to have progressed nearly to the rear of one of the colliding polytropes. Immediately behind the shock lies a lightly shaded region where the combination of outgoing fluid velocities and temperature are sufficient for gravitational escape. Since this picture represents only a quarter of a meridional cut through the colliding system, there is a similar recoil shock below.

merely slowed down as it encounters one of these shocks but strongly accelerated back in the direction from which it came (cf. Figure 5). The more intensely shocked material located outside the strongly-bound central region acquires a velocity sufficient for gravitational escape.

As the collision process proceeds towards later stages, fluid elements in outer regions continue to stream away from the center, while a readjustment and settling down take place within the more dense gravitationally bound central regions (cf. Figures 6d, 7f, and 8d). It is significant that, for all three initial collision velocities investigated, the total mass of gravitationally unbound material (viz., volatile mass) is found to approach a constant value, thus enabling us to make a sensible estimate of the mass-fraction which escapes coalescence.

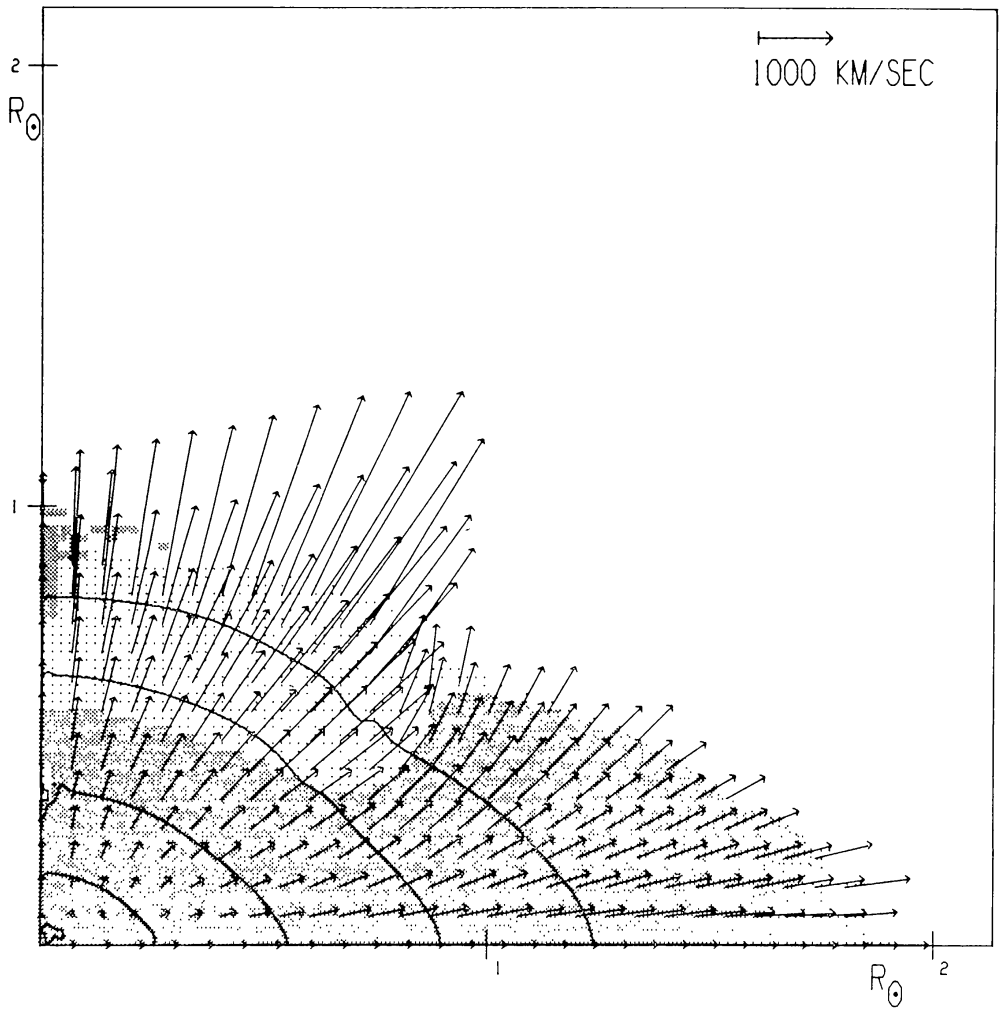

Fig. 5e. In this picture the recoil shock has broken through the rear surface leaving an extensive region of violently expanding hot fluid, which subsequently assumes the forms of Figures 3a and 6d. The real time elapsed since the configuration of Figure 5a amounts to 38.2 min. Moreover, according to Figures 3a and 6d, for lowest-velocity collision, the lightly shaded material shown at the lower righthand corner must cool during lateral expansion so as to again become gravitationally bound.

4. Mass-Escape *vs.* Collision Velocity

The numerical results of physical significance were obtained from the runs listed in Table I. All but one of these were initialized by supposing that at machine zero two undistorted solar-like polytropes separated by 2.2 $R_\odot$ were approaching each other head-on at a prescribed velocity. If a much larger machine-zero separation had been assumed the machine running time would have been greatly increased as well as the cumulative build-up of errors. The one calculation started from a machine-zero separation of 4.2 $R_\odot$ shows little if any indication of change in the calculated mass-escape fraction F. Generally speaking, runs made on the larger finite-difference network (128 by 128) are the most important.

TABLE I

Head-on colliding polytropes: physically significant runs

Initial relative velocity at infinite separation km s^{-1}	Density cutoff ϱ/ϱ_c	Finite difference steps per $R_\odot$	Size of network in terms of netpoints	Nature of artificial dissipation (cf. Appendix)		
				Flow-bias ε_0	κ_0	q_0
zero	10^{-6}	20	64 by 64	1.00	0.2	3.0
zero	10^{-7}	20	64 by 64	1.00	0.2	3.0
zero [b]	10^{-6}	20	64 by 64	0.20	0.2	2.0
zero [a]	10^{-6}	20	64 by 64	1.50	0.2	3.0
zero	10^{-6}	20	128 by 128	1.00	0.2	2.0
zero	10^{-7}	20	128 by 128	1.00	0.2	2.0
zero	10^{-6}	40	128 by 128	1.00	0.2	2.0
zero [c]	10^{-6}	60	128 by 128	1.00	0.2	2.0
1000 [b]	10^{-6}	20	64 by 64	0.60	0.2	2.0
1000	10^{-6}	20	128 by 128	1.20	0.2	3.0
1000	10^{-6}	40	128 by 128	1.20	0.2	2.0
2000	10^{-6}	20	128 by 128	2.00	0.1	3.0
2000	10^{-6}	40	128 by 128	2.00	0.15	2.0
2000 [b]	10^{-6}	20	64 by 64	1.00	0.2	2.0
2000 [d]	10^{-6}	20	64 by 64	2.00	0.15	2.0

[a] Machine-zero separation was 4.2 $R_\odot$; in all other cases this was 2.2 $R_\odot$.
[b] Δt limited only by $\Delta t \leqslant 0.5\, h/\hat{c}$; elsewhere, except for the last run, Δt was limited both by $\Delta t \leqslant 0.2h/\hat{c}$ and $\varrho_{i,j}{}^{n+1} \geqslant 0.6\ \varrho_{i,j}{}^{n}$.
[c] Only partially completed.
[d] $\Delta t \leqslant 0.2h/\hat{c}$ and $\varrho_{i,j}{}^{n+1} \geqslant 0.0\ \varrho_{i,j}{}^{n}$.

Uniform differencing was used throughout any run, the fineness of zoning being either 20, 40, or 60 netpoints per $R_\odot$. The coarser-zoned models (20 netpoints per $R_\odot$) had more room in the domain of calculation both for translation and the development of the collision process. On the other hand, those calculations employing finer-zoned models were better able to represent the collision mechanism. All the machine-generated pictures exhibited here (Figures 1 through 11) stem from fine-zoned calculations.

Curves of volatile mass *vs.* time resulting from the numerical calculations are shown in Figures 12, 13, and 14. The important property of any such curve from the standpoint of estimating F, the mass fraction which escapes gravitational binding, is the maximum value or what is, broadly speaking, the leveling-off value. Upon comparing the three figures, a marked increase in volatile mass with initial collision velocity is immediately evident. In addition, the following extraneous effects appear: (1) The leveling-off values of volatile mass depend upon mesh width, $\Delta r = \Delta z = h$. (2) Once the leveling-off condition is achieved, the volatile mass falls off slowly and continually with time. (3) There is a slight increase in the leveling-off value as the density cutoff is lowered.

The variation with mesh width is attributed to discretization errors (errors due to the replacement of a largely continuous system of differential equations by equa-

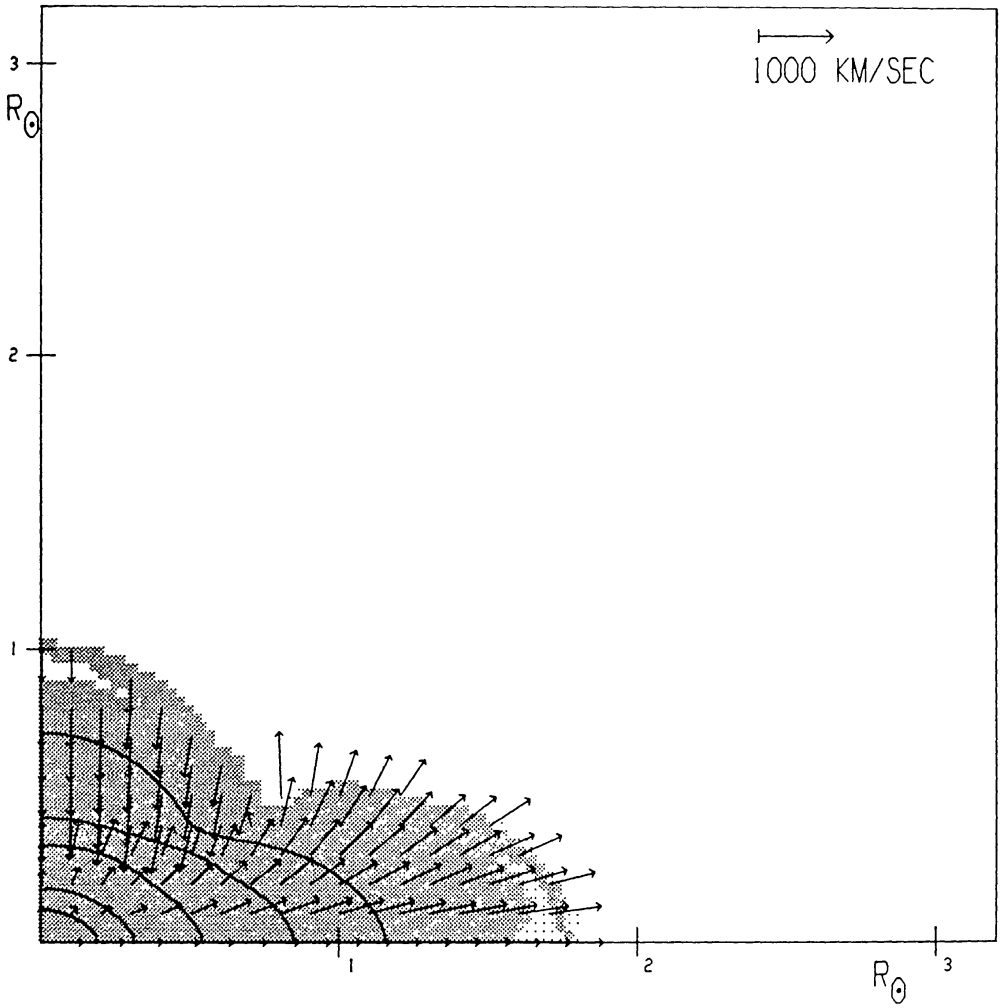

Fig. 6a. Shortly after maximum impact and 2118 s after machine-zero (viz., the configuration of Figure 5a) for the case of a head-on collision starting from *zero* initial velocity at infinite separation. This figure is due to a calculation employing a mesh width of 40 steps per $R_\odot$ and may be compared with the finer-zoned results of Figure 5c.

tions involving discrete differences; also called *truncation errors*; (cf. Richtmyer and Morton, 1967; Forsythe and Wasow, 1960; etc.). In our current program such errors are generally of second order with respect to the small quantities $\Delta r = \Delta z = h$ and Δt. Moreover, since empirical evidence shows that machine round-off and other random errors are negligible in our results, the total computational errors should consist almost entirely of discretization errors. The lowest-velocity collision (Figure 12) exhibits the most clear-cut dependence on h. Results of the 1000-km s^{-1} collision, on the other hand, seem largely insensitive to h (Figure 13); while, in the 2000-km s^{-1} collision (Figure 14), the sign of the variation of volatile mass with h is opposite that for the lowest-velocity collision, thereby implying dependence of the discretization error on collision velocity.

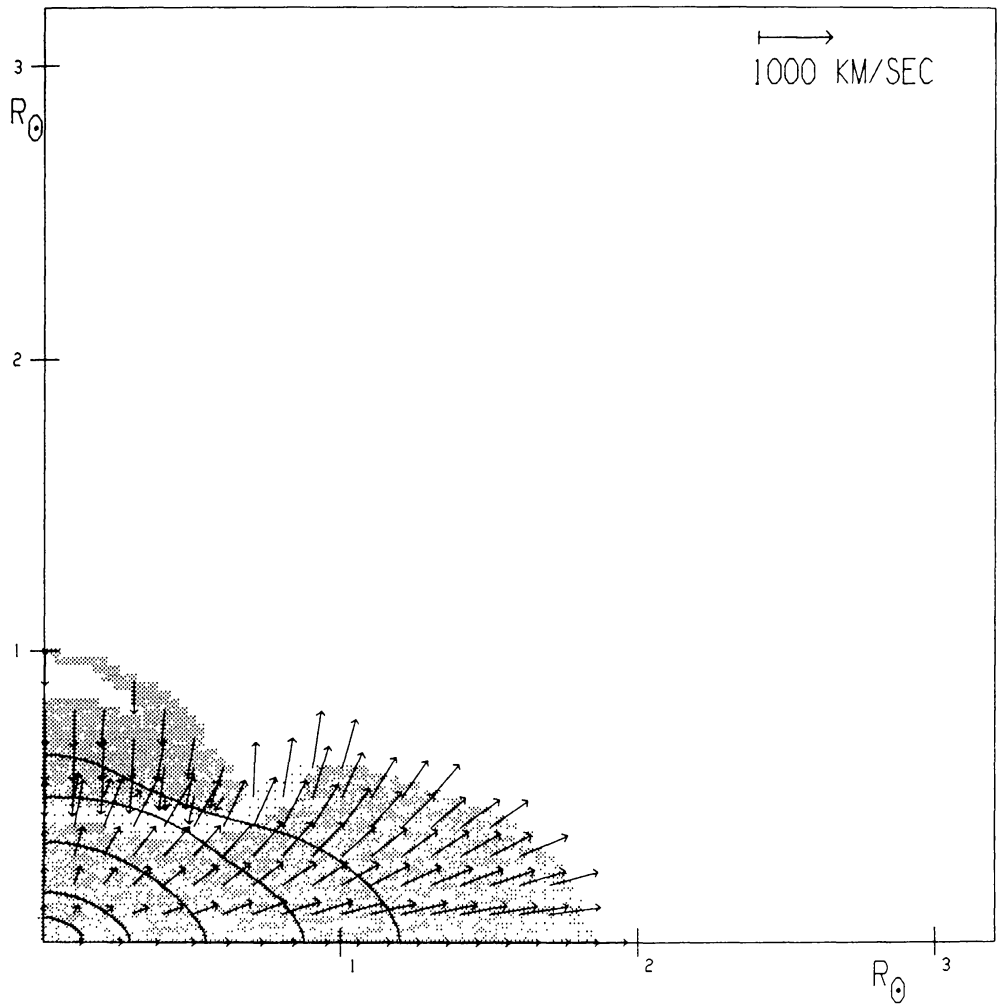

Fig. 6b. Shows the development of a volatile region immediately behind the recoil shock (case of *zero* initial collision velocity and 40 steps per $R_\odot$). The above configuration corresponds to 2196 s after machine-zero.

The slow fall-off in the leveling-off value of volatile mass and its dependence on the density cutoff both arise from the discard of finite-difference mass elements whenever their calculated density drops below a certain prescribed lower limit. A quantitative estimate of the slow decrease has been made as follows: It is noted that the outermost regions of fluid generally have a density close to cutoff $[\varrho(\text{cutoff})=\varepsilon]$, and late in a collision calculation they are diverging at some average speed $\bar{v}$. These regions are located at some mean distance $\bar{R}$ from the center of impact; and, as they continue to expand, the fluid density of the outermost regions drops below ε resulting in the discard of mass at a rate roughly equal to $4\pi\bar{R}^2\bar{v}\varepsilon$. This rate of mass loss is in agreement with the curves of Figure 12. The effect is most noticeable in the lowest-velocity collision since the volatile mass increases faster with collision velocity than does mass loss due to the cutoff; all of which suggests that the volatile mass depends

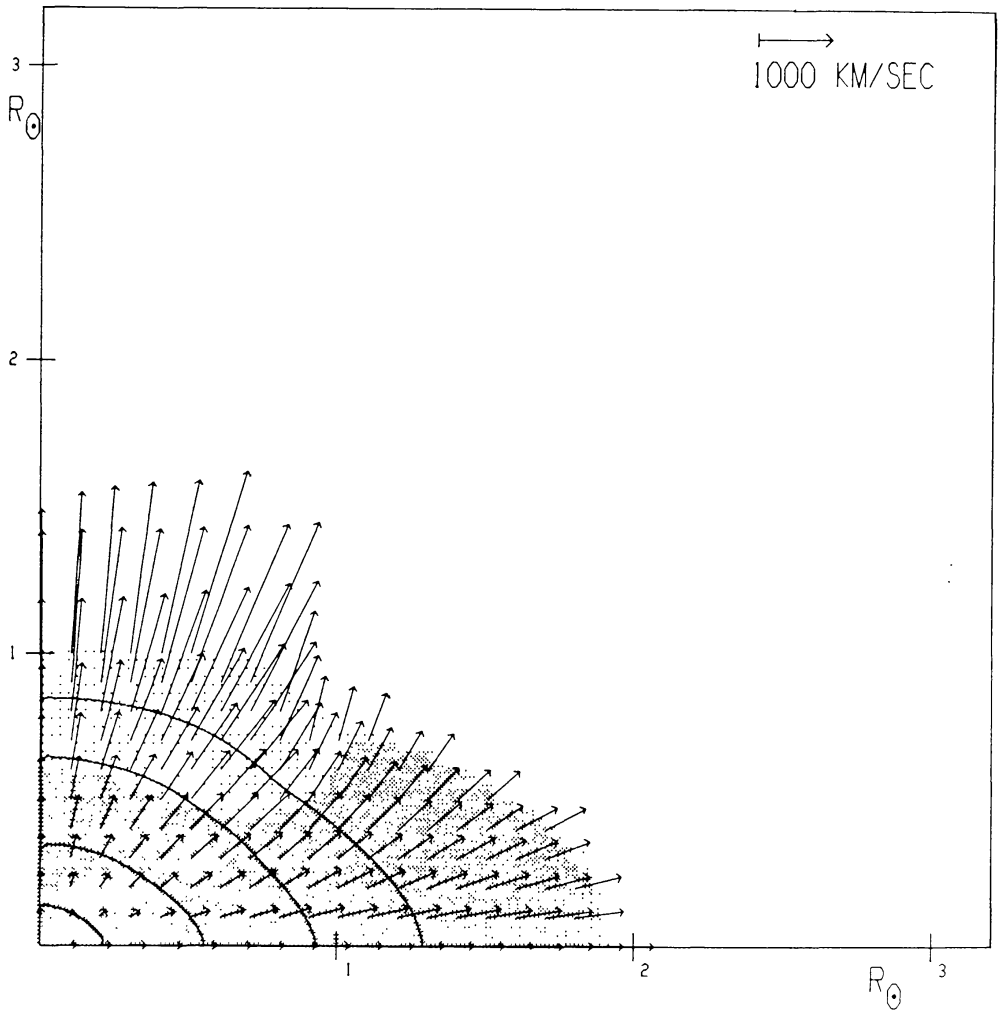

Fig. 6c. Soon after the recoil shock has broken through the rear surface, 2358 s after machine-zero (case of *zero* initial collision velocity and 40 steps per $R_\odot$).

more on the initial kinetic energy, while the cutoff mass loss is more nearly proportional to initial collision velocity.

An examination of the errors in our numerical calculations – especially for volatile mass – is given in Section 8 of the Appendix, which includes the following: (A) machine round-off errors; (B) errors due to the low-level density cutoff (as above); (C) effects of artificial dissipation; and (D) discretization errors. It is shown there that on the basis of empirical evidence round-off errors must be negligible. Moreover, use is made of numerical results to determine the errors arising from the low-level density cutoff in the three cases of initial collision velocity. The effects of artificial dissipation, particularly on calculated values of volatile mass, are inferred to be either negligible or of $O(h^2)$, like the discretization errors. Finally, a method for estimating the combined effect of discretization errors and artificial dissipation is described; it makes direct use of the observed dependence of the leveling-off value of volatile mass on

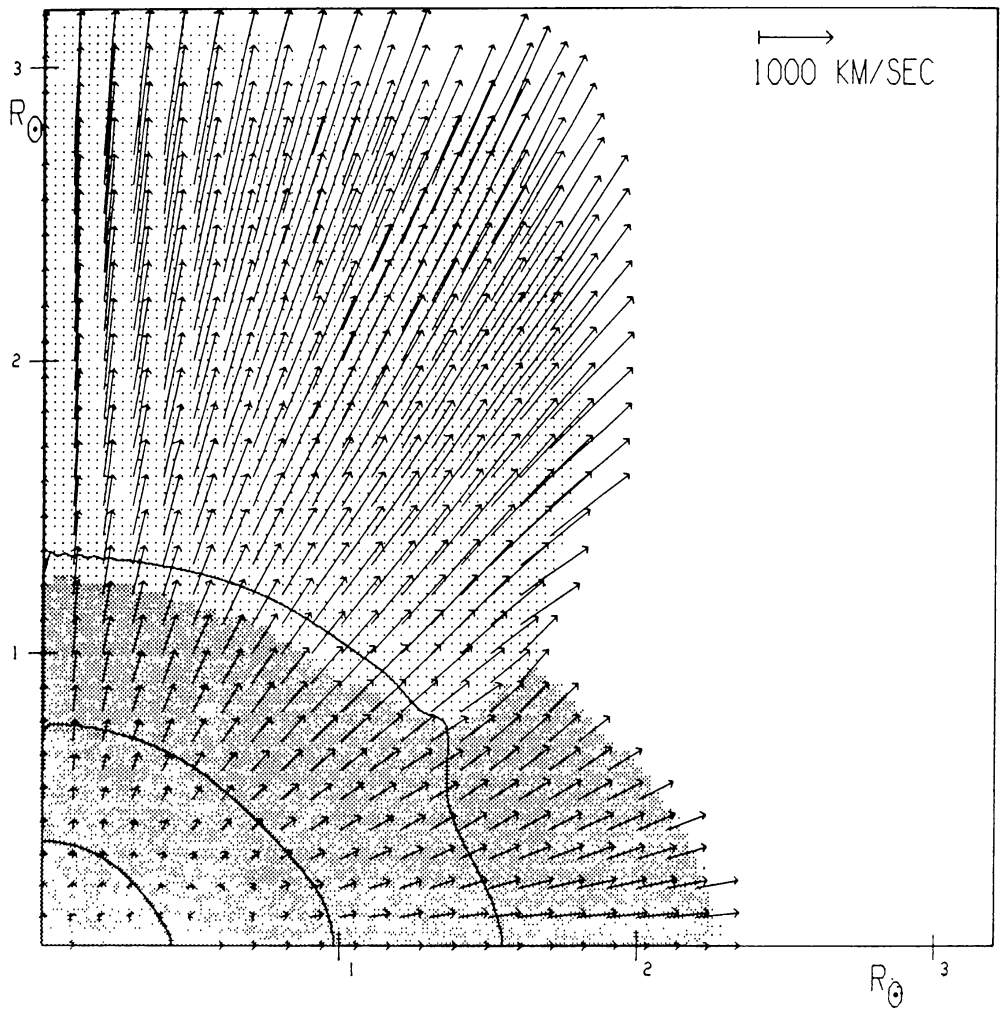

Fig. 6d. Shows the manner of mass escape in the case of *zero* initial collision velocity (40 steps per $R_\odot$). This is the condition 3010 s after machine-zero.

mesh width h (e.g., Figure 12). The particular considerations found necessary for each of the three initial collision velocities are summarized below.

In the case of *zero* initial collision velocity at infinite separation, the procedures given at the end of Section 8 of the Appendix have been applied both to obtain a best value for the volatile mass and to correct for mass loss caused by the density cutoff. In this case the variation of volatile mass with mesh width h is clear (Figure 12), and so Equation (A133) of the Appendix could be used to improve our results by carrying out a partial extrapolation to zero mesh width (Richardson's method; cf. Forsythe and Wasow, 1960, and elsewhere). The improved value of volatile mass was then multiplied by an empirically-determined number (viz., 1.070) to compensate for mass loss due to the density cutoff. The relative computation error in the final value of volatile mass was assumed to be approximately the same as relative computation errors worked out for the three quantities whose variations with h were investi-

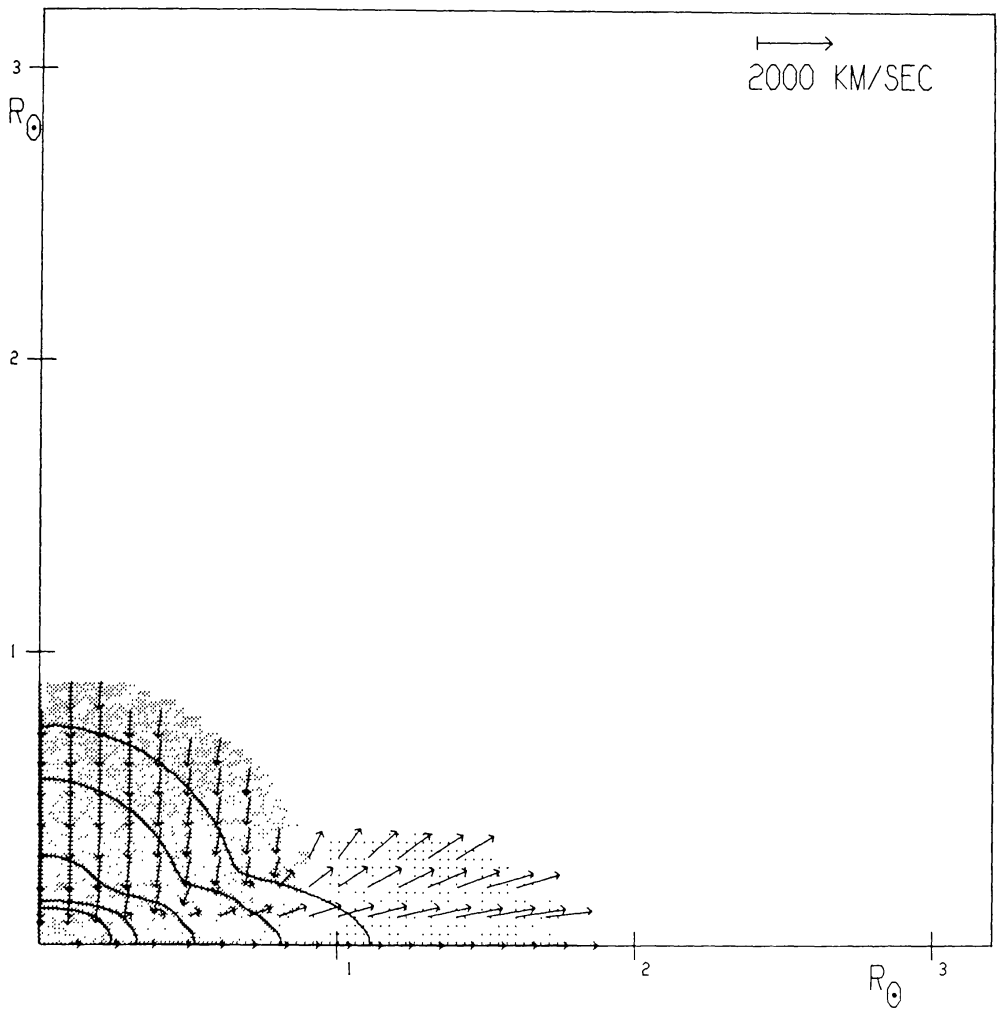

Fig. 7a. Display of the velocity field at the instant of maximum total internal energy in the case of a head-on collision starting from a relative approach velocity of 1000 km s^{-1}. This figure corresponds to Figure 1c, which is the instantaneous configuration 1218 s after machine-zero (machine-zero is shown in Figure 1a). All pictures in Figures 1 and 7 stem from the same calculation using a mesh width of 40 steps per $R_\odot$.

gated in Section 8 of the Appendix [cf. Equation (A135), particularly M_v(early)]. Thus, the volatile mass for *zero* initial collision velocity at infinite separation has been calculated to be

$$M_v = 0.0081^{+0.0020}_{-0.0000} \quad \text{machine units}$$

and the mass-escape fraction which follows according to Equation (8) is

$$F = 0.052^{+0.013}_{-0.000}.$$

In transferring this result to Table II, the error limits were expanded slightly to allow for small uncertainties in our corrections and interpretation.

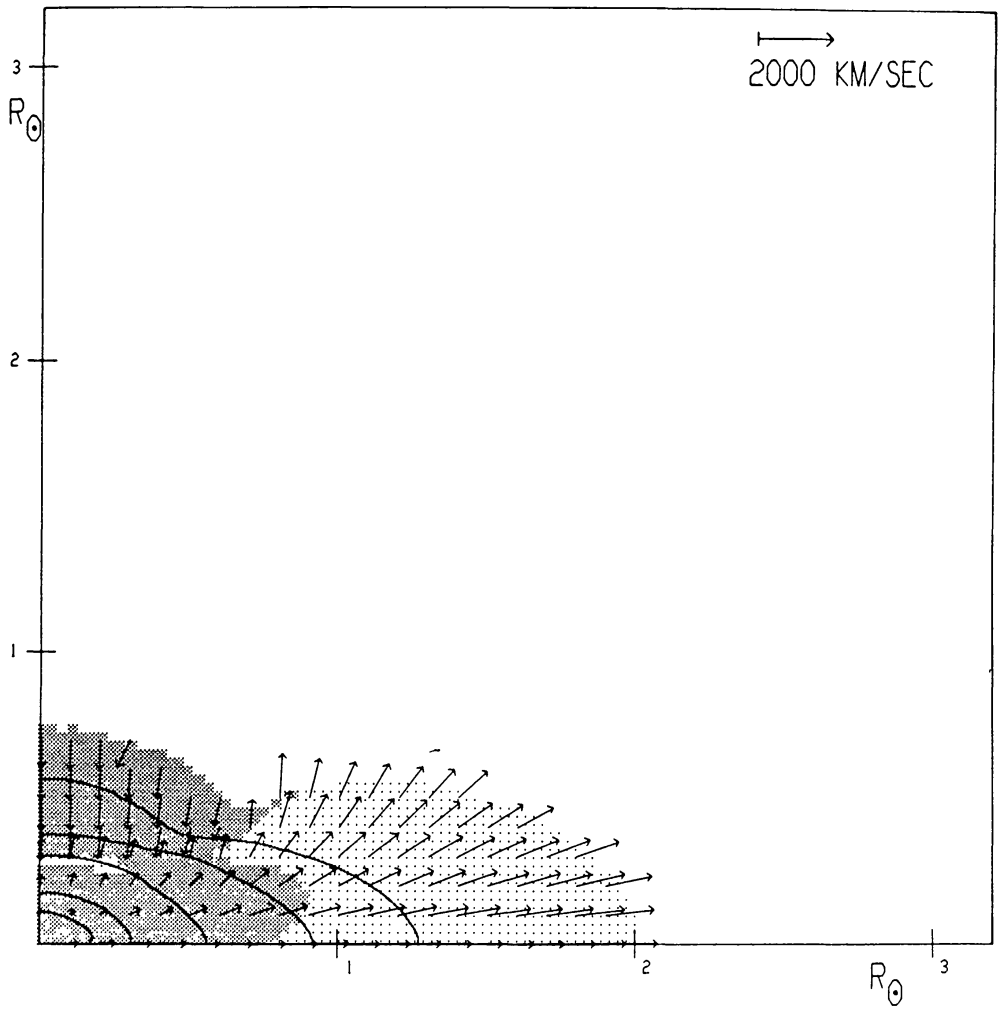

Fig. 7b. The 1000-km s^{-1} collision 1389 s after machine-zero (40 steps per $R_\odot$). The recoil shock has moved about halfway through the oncoming polytrope. Lateral ejection velocities reach 1370 km s^{-1} (cf. calibration arrow in upper righthand corner).

TABLE II

Coalescence resulting from the head-on collision of two polytropes of solar mass and radius

Initial collision velocity center to center at infinite separation	F, mass fraction which escapes coalescence
zero	$0.052^{+.0015}_{-0.005}$[a]
1000 km s^{-1}	0.180 ± 0.015[a]
2000 km s^{-1}	0.60 ± 0.05[a]

[a] Numerical errors

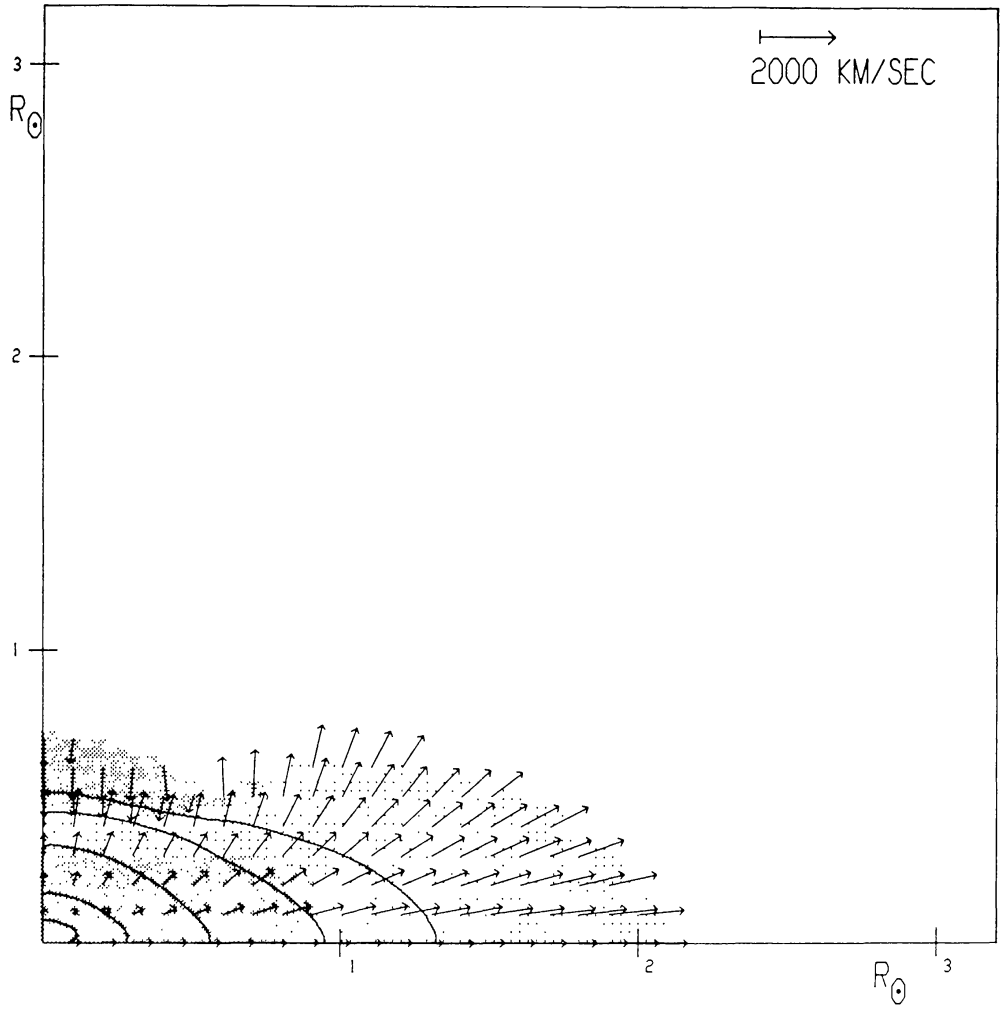

Fig. 7c. The 1000-km s^{-1} collision 1442 s after machine-zero (40 steps per $R_\odot$). A broadening volatile region appears immediately behind the shock.

The error limits are not so clearly defined for collision calculations involving 1000 km s^{-1} and 2000 km s^{-1} initial relative velocities. In these instances, the leveling-off values for finer-zoned runs were never quite achieved (Figures 13 and 14), as the calculations could not be completed before outward-moving fluid began to strike and rebound from the artificial boundaries imposed on the domain of calculation. The effect was greatest for the 2000-km s^{-1} collision. There was more room for expansion in the coarser-zoned runs where the initial stellar model took up a smaller fraction of the available computational space. The difficulty could have been overcome if there had been additional time for re-coding; i.e., an efflux of fluid through the boundaries would have been permissible if the amount was calculated and corrections introduced for any gravitational perturbations. However, despite certain weaknesses, the present results appear sufficient to meet our main objectives.

For the initial relative collision velocity of 1000 km s^{-1} at infinite separation, our

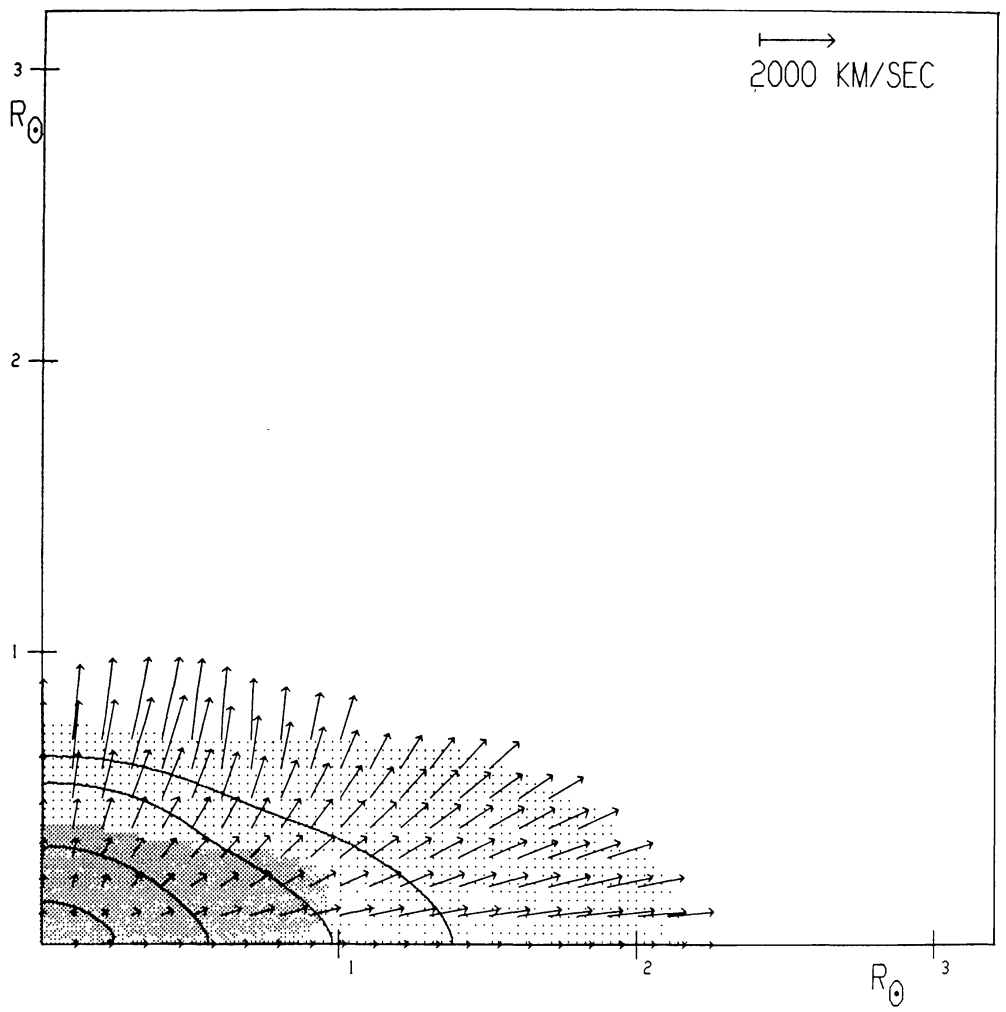

Fig. 7d. The 1000-km s^{-1} collision 1506 s after machine-zero (40 steps per $R_\odot$). The recoil shock front has just broken through the rear surface.

best value of volatile mass was largely determined by the leveling-off value of the run having a 128 by 128-point network with mesh width $h = R_\odot/20$ (cf. Figure 13). The principal correction used was that for mass loss due to the density cutoff. Error limits were estimated by considering the greatest possible positive and negative corrections. It was even allowed that there could be an error which was correlated with imperfect energy conservation, although a more plausible explanation for the small drop in total energy (e.g., Figure 10 shows an overall energy decrease equal to 4.4% of the total gravitational binding energy at infinite separation) is to associate the effect with kinetic-energy loss accompanying the mass loss caused by the density cutoff. The greatest possible positive correction included (1) an upwards adjustment to counteract the small fall-off in total energy, assuming that this is not due to the density cutoff and indicates a corresponding fall-off in volatile mass, and (2) the largest possible compensation for mass loss due directly to the density cutoff. On

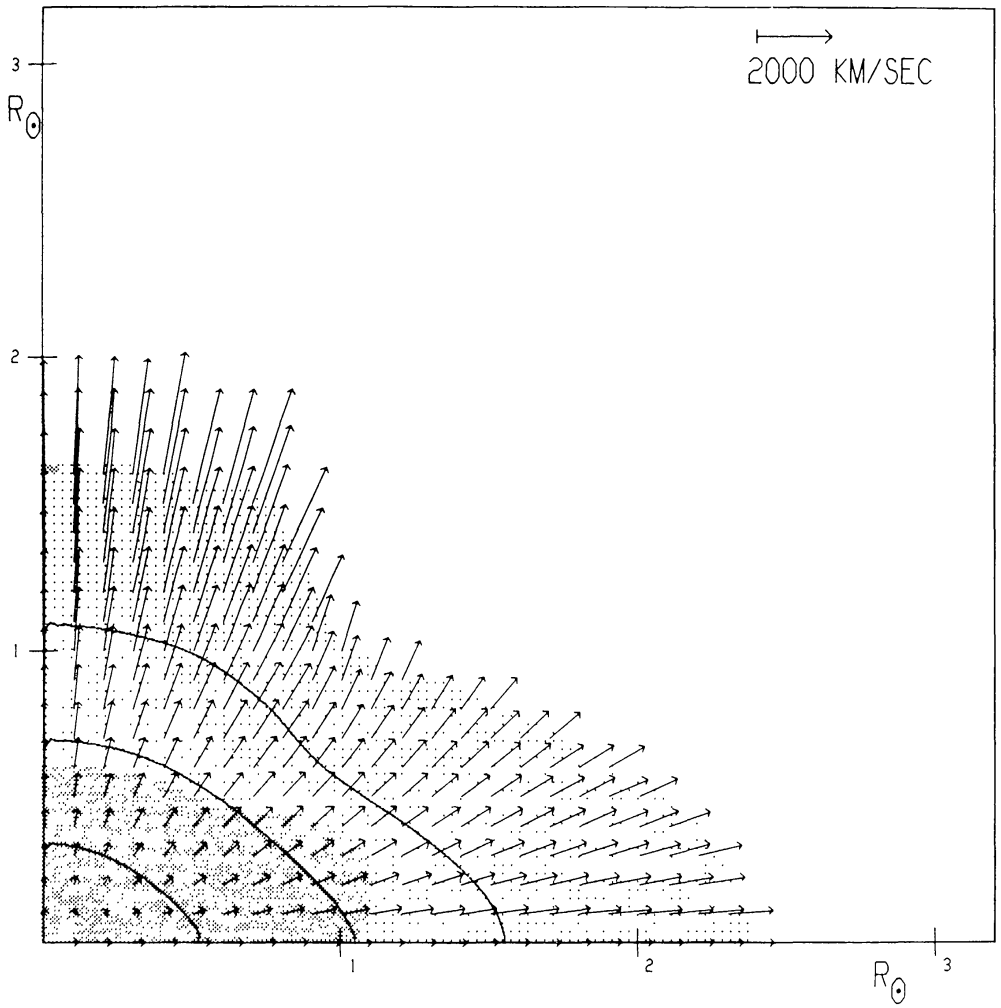

Fig. 7e. The 1000-km s^{-1} collision 1701 s after machine-zero (40 steps per $R_\odot$). This picture corresponds precisely to Figure 1d. The density contours shown are, from the center out, $\varrho/\varrho_c = 0.1$, 0.01, and 0.001.

the other hand, the lower limit was obtained by using the least possible correction for density-cutoff mass loss and by assuming that a dependence upon h existed, and that this dependence was the only factor causing the slight decrease observed in calculated values of volatile mass as the mesh width h was dropped from $h = R_\odot/20$ to $h = R_\odot/40$ (Figure 13). The consequent partial extrapolation to zero mesh width was carried out by means of Equation (A133) of the Appendix. The results of these considerations are set out in Table II. Incidentally, the procedure for making adjustments because of small deviations in energy conservation is discussed briefly below.

Suppose the volatile mass were correlated with the total energy ε; then the effect might be expressed approximately by writing

$$M_v(\varepsilon_0) \simeq M_v(\varepsilon_0 + \Delta\varepsilon) - (\mathrm{d}M_v/\mathrm{d}\varepsilon)\ \Delta\varepsilon \tag{9}$$

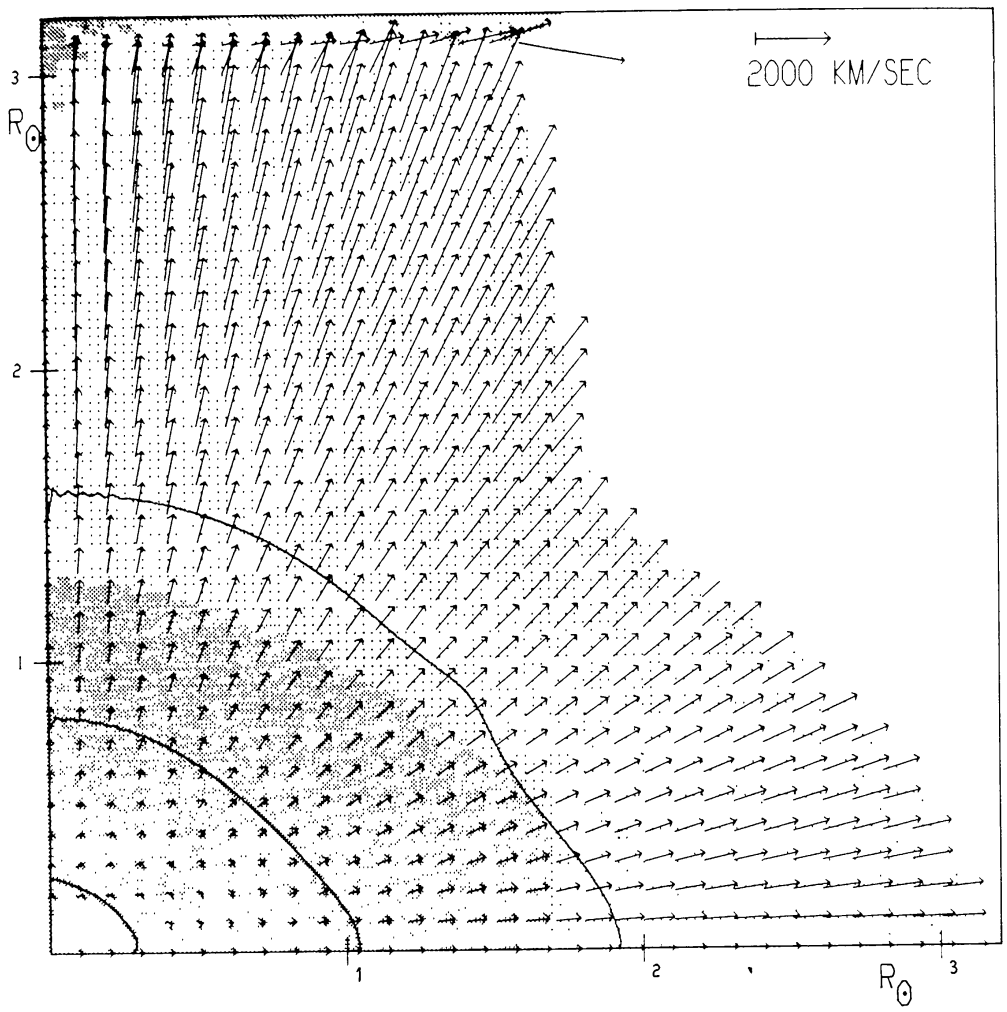

Fig. 7f. The 1000-km s^{-1} collision 2360 s after machine zero (40 steps per $R_\odot$). Velocities in the gravitationally-bound central region (shaded darker) are approaching quiescence. Velocity changes and darkening at the very top of the picture arise from impact against the artificial rigid boundary of the domain of calculation.

where $M_v\varepsilon_0$ denotes the value of volatile mass corresponding to ε_0, the initial total energy of the system. From six runs on the 1000-km s^{-1} collision (not all of which are listed in Table I) pairs of values were obtained for $M_v(\varepsilon)$ *vs.* ε at the time of the final point on the $R_\odot/40$ curve in Figure 13. When these values were plotted, the points fell reasonably close to a straight line; hence, an approximate value for $d\,M_v d\varepsilon$ could be determined empirically. This quantity was then available for correcting the leveling-off value of volatile mass according to Equation (9).

Our estimate of volatile mass in the case of 2000-km s^{-1} relative velocity at infinite initial separation is again based largely on the leveling-off value of the calculation employing a 128 by 128-point grid with mesh width $h=R_\odot/20$. Two corrections were

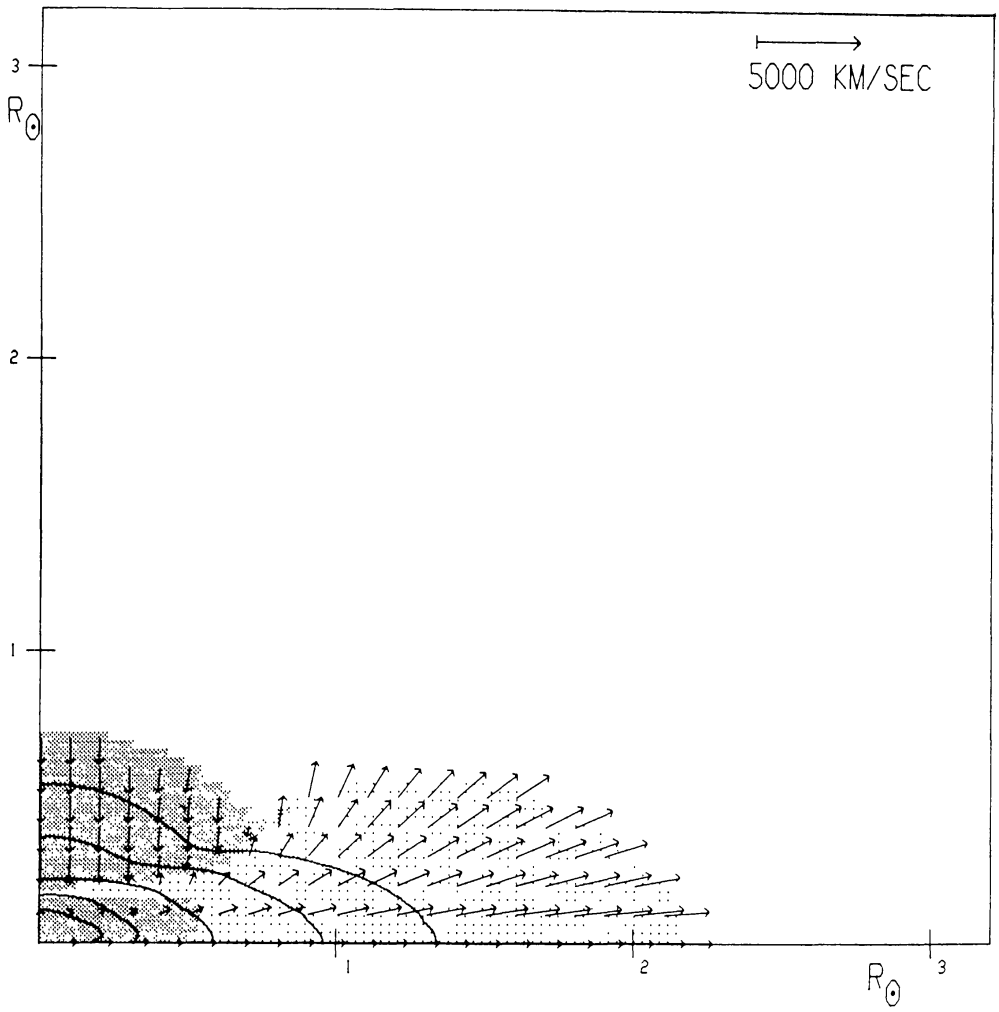

Fig. 8a. Velocity field 81 s after the point of maximum internal energy or 842 s after machine-zero for a head-on collision where the initial collision velocity was 2000 km s^{-1} at infinite separation. The machine-zero configuration was like that shown in Figure 1a. Lateral ejection velocities at this time are as high as 2460 km s^{-1} (cf. calibration arrow in upper righthand corner). Calculation employed a mesh width of 40 steps per $R_\odot$.

introduced: (1) an adjustment for mass loss due to the density cutoff and (2) an attempt, in view of the apparently unambiguous dependence on h (cf. Figure 14), to partially extrapolate the results to zero mesh width h. An upper limit for the first correction is immediately available from the small overall losses incurred by the total mass of the system; but, the second correction is not well-determined, since the run with $h=R_\odot/40$ did not extend far enough to reach the leveling-off region. Any effects associated with imperfect energy conservation must be negligible in the 2000-km s^{-1} case for two reasons: On comparing calculations using $h=R_\odot/20$ with one where $h=R_\odot/40$, the discrepancies found for total or kinetic energy of the system versus h do not correlate with the observed dependence of volatile mass on h. In contrast, such a correlation (spurious or otherwise) does appear in results calculated for the

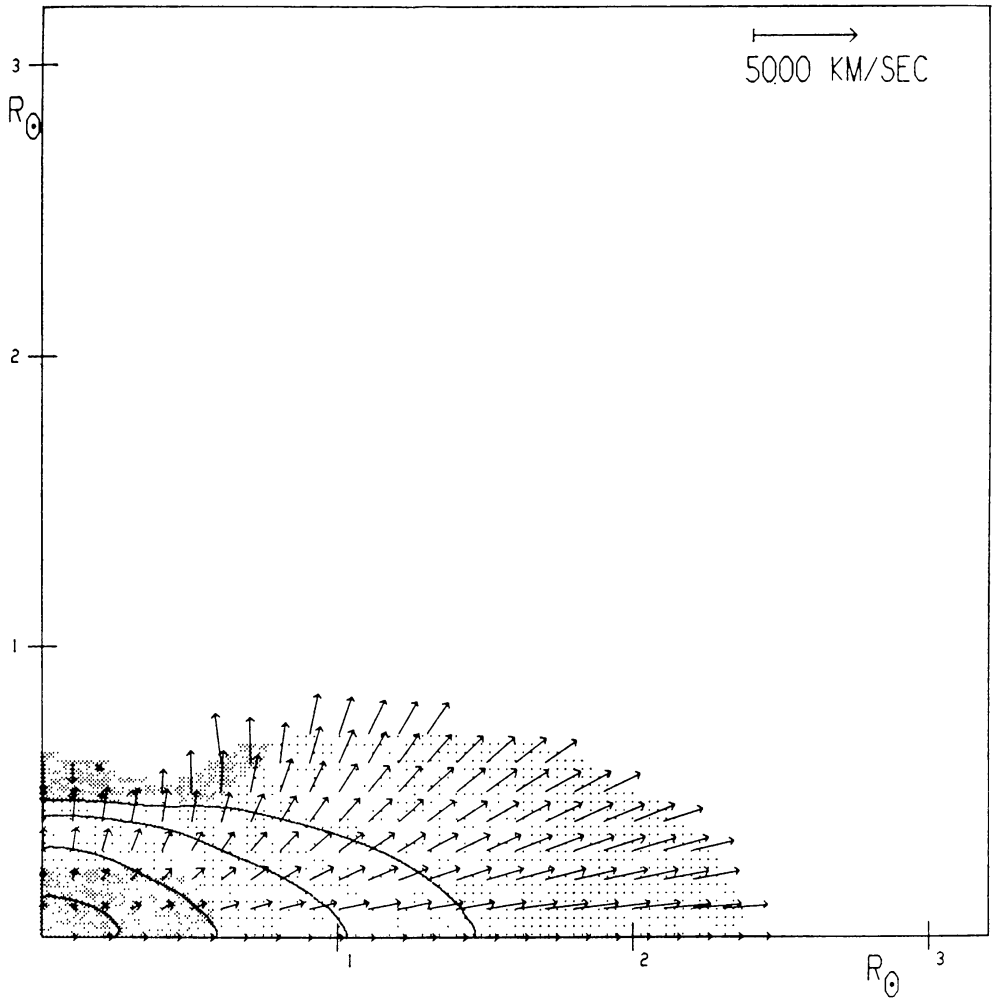

Fig. 8b. The 2000-km s^{-1} collision 923 s after machine-zero (40 steps per $R_\odot$). Fluid in lightly shaded region has sufficient energy to escape gravitational binding.

1000-km s^{-1} collision. Secondly, although some small decrease in total energy generally occurred during a 2000-km s^{-1} run, this can be readily attributed to the kinetic-energy loss associated with the mass loss due to the density cutoff. Thus, only discretization errors remain as a source of the observed changes with mesh width h; and, certain components of these errors must depend upon collision velocity in order to explain the shift from a decrease in volatile mass as h decreases to the reverse behavior, which has been found when the initial collision velocity was zero (cf. Figures 12 and 14).

By invoking first one then the other of two extreme correction procedures, bounds are placed on the value of volatile mass following a 2000-km s^{-1} collision. To estimate a probable upper bound, no reduction is made in the value of volatile mass to correct for the h dependence, and the maximum possible compensation is allowed for volatile-mass loss due to the density cutoff. In estimating a probable lower bound,

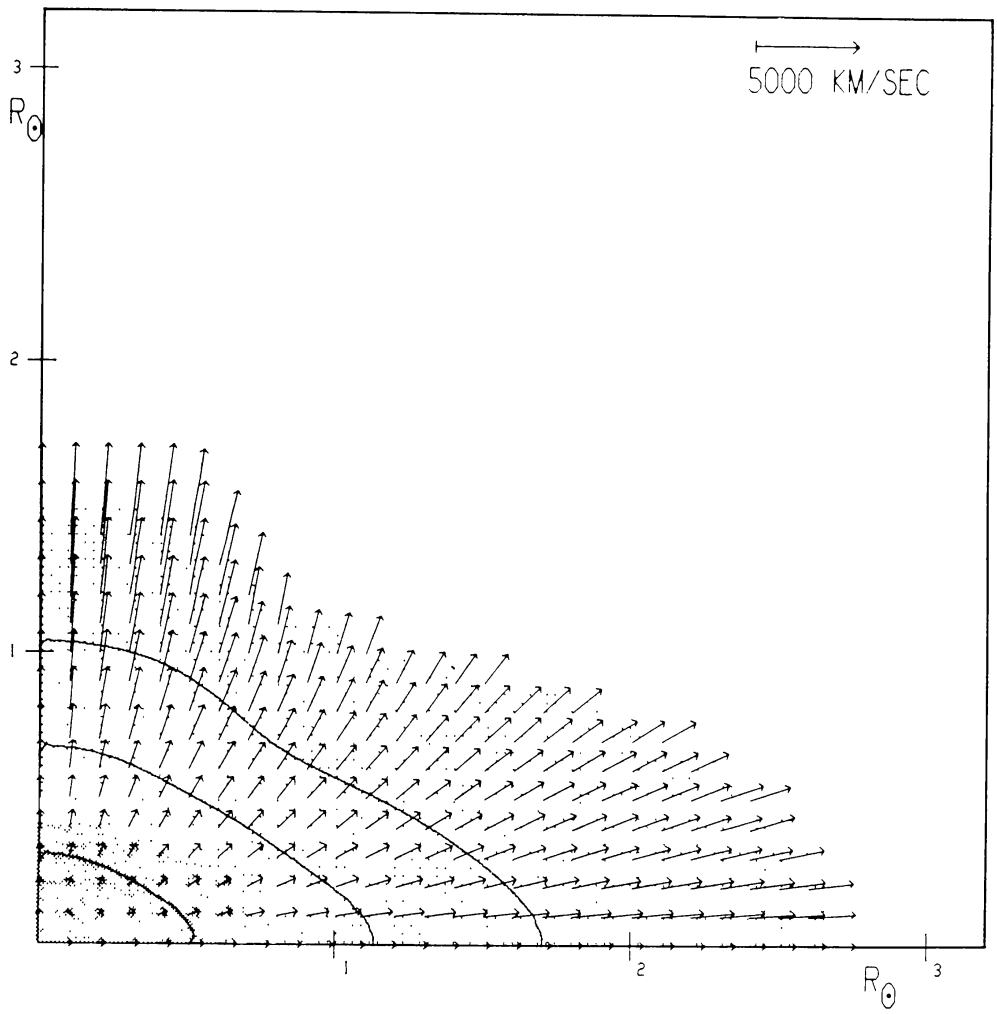

Fig. 8c. The 2000-km s^{-1} collision 1075 s after machine-zero (40 steps per $R_\odot$). Proceeding from the center out, the density contours are $\varrho/\varrho_c = 0.1$, 0.01, and 0.001. Outward streaming velocities near the collision axis are as high as 4600 km s^{-1}.

the least possible correction was introduced for the density-cutoff mass loss; while, on the basis of the numerical results available, the h dependence of volatile mass was extrapolated to the leveling-off region where Equation (A133) of the Appendix was used to provide an estimate of the value of volatile mass at zero mesh width. Thus, the mass-escape fraction for the case of 2000 km s^{-1} initial relative collision velocity was found to lie between $F=0.66$ and $F=0.55$; it was therefore sensible to quote $F=0.60\pm0.05$ as being representative of our numerical results.

5. Conclusions

For a relative initial collision velocity at infinity of 1512 km s^{-1} the initial kinetic and gravitational-binding energies are equal, and the system is energetically capable

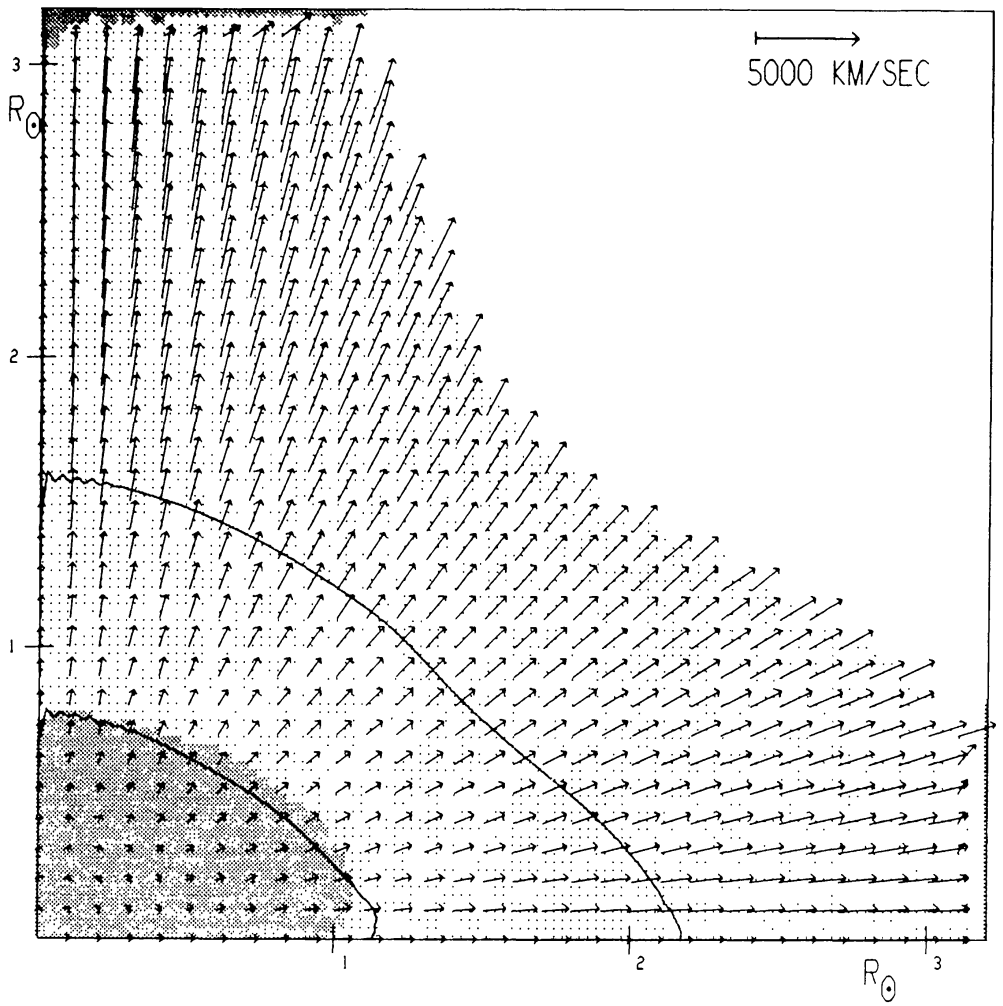

Fig. 8d. The 2000-km s^{-1} collision 1451 s after machine-zero (40 steps per $R_\odot$). Proceeding outwards from the center, the density contours are $\varrho/\varrho_c = 0.01$ and 0.001. Compared to Figures 6d and 7f, the residual gravitationally-bound object (shaded darker) is much smaller. At the extreme top and right, influences can be seen of the rigid boundaries of the domain of calculation.

of complete disruption. By interpolation (linear or quadratic) of the results shown in Table II for head-on collisions, we estimate that 35 or 40% of the total mass would be ejected at this collision velocity; thus, the collision process exhibits a strongly inelastic behavior. If the three values of F from Table II are plotted against the square of the initial collision velocity, the points lie on a straight line well within the error limits quoted. On this basis, the point where the central remnant has half of the total mass occurs for a collision velocity in the vicinity of 1800 km s^{-1}. We therefore conclude that stellar collisions where the relative collision velocity is less than this value (such as in galactic cores) will be amalgamative and lead to the formation of more massive stars by coalescence, at least for the case of head-on collisions.

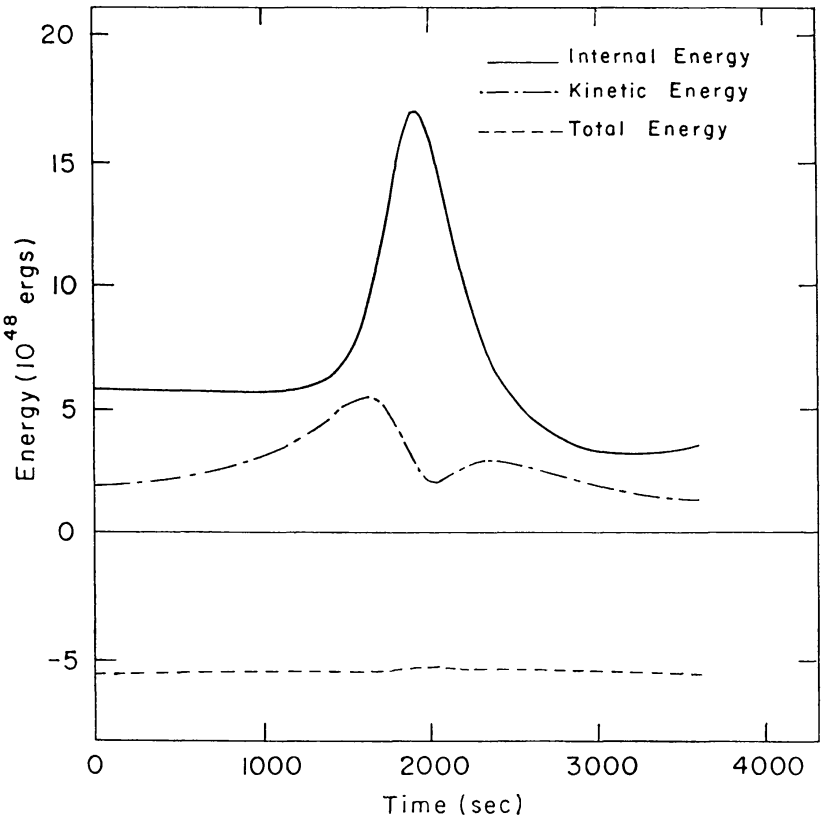

Fig. 9. Variations with time of internal, kinetic, and total energies for a system involving a head-on collision between two solar-like polytropes starting from *zero* relative velocity at infinite separation.

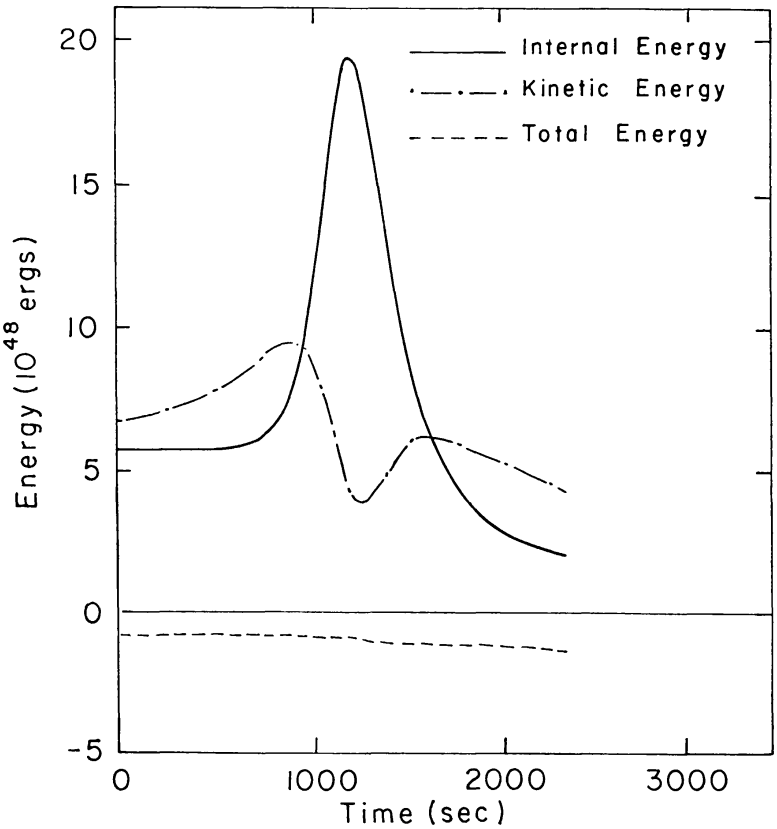

Fig. 10. Internal, kinetic, and total energies *vs.* time for a system which represents the head-on collision of two solar-like polytropes initially closing at a relative velocity of 1000 km s^{-1}.

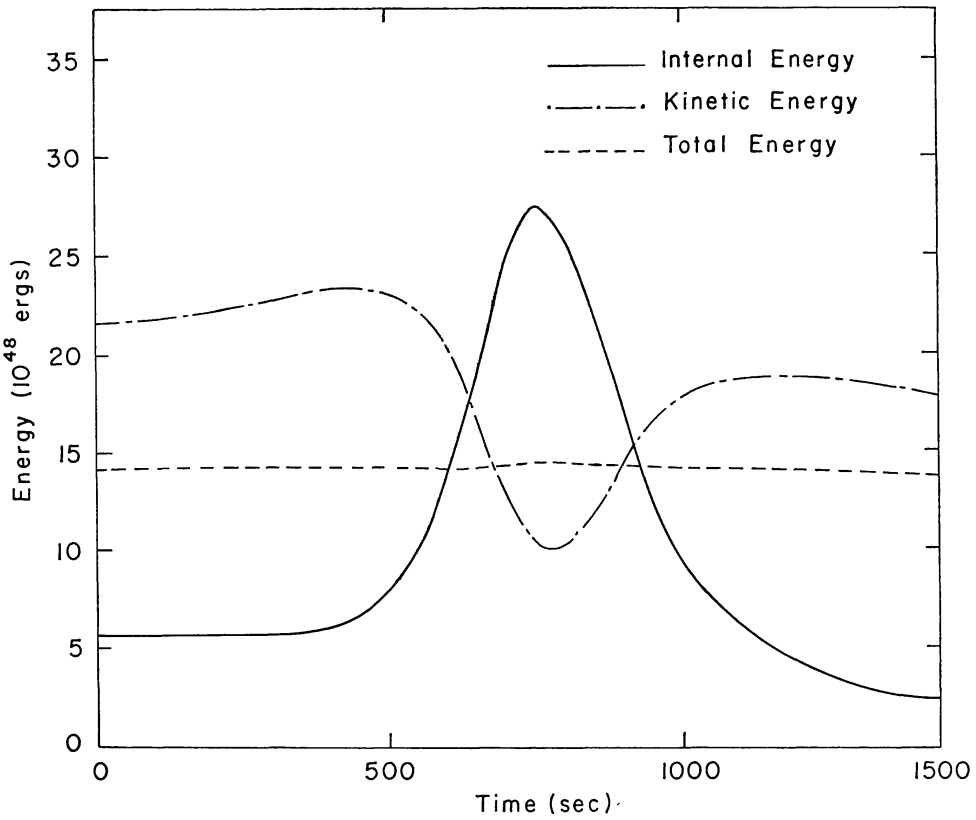

Fig. 11. Internal, kinetic, and total energies *vs.* time for a system in which two solar-like polytropes collide head-on starting from an initial relative velocity of 2000 km s^{-1} at infinite separation.

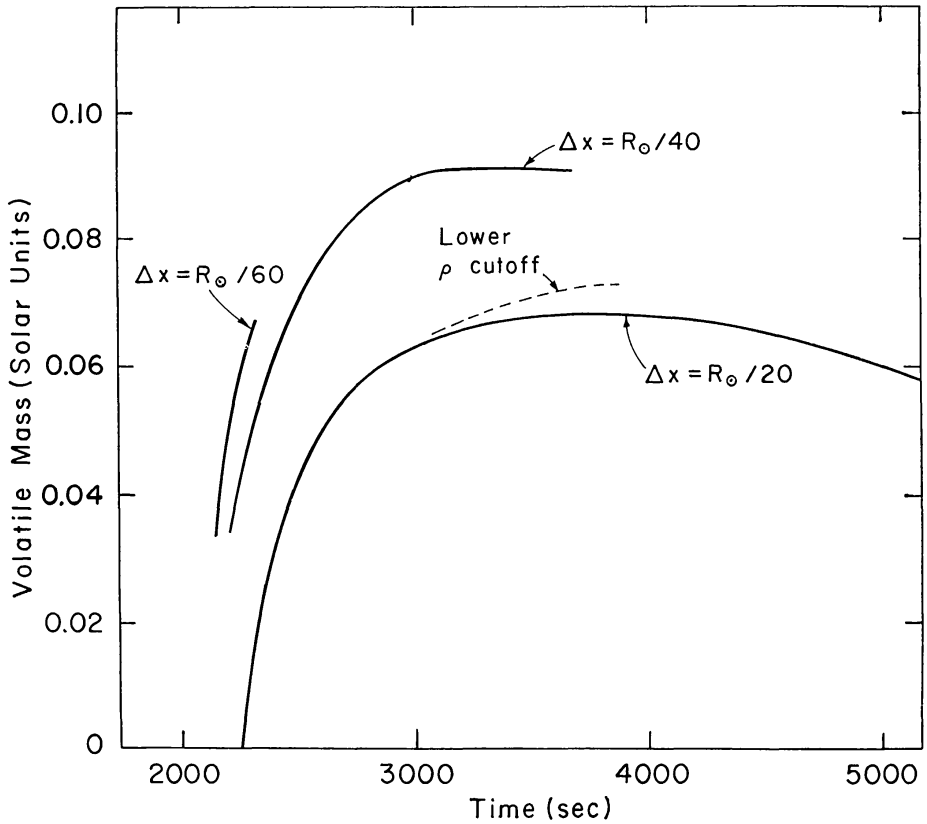

Fig. 12. Volatile mass *vs.* time following a head-on collision involving two solar-like polytropes starting from *zero* relative velocity at infinite separation, where the volatile mass at any time is the total mass energetically capable of gravitational escape. The appreciable dependence on mesh width Δx is attributed to discretization errors.

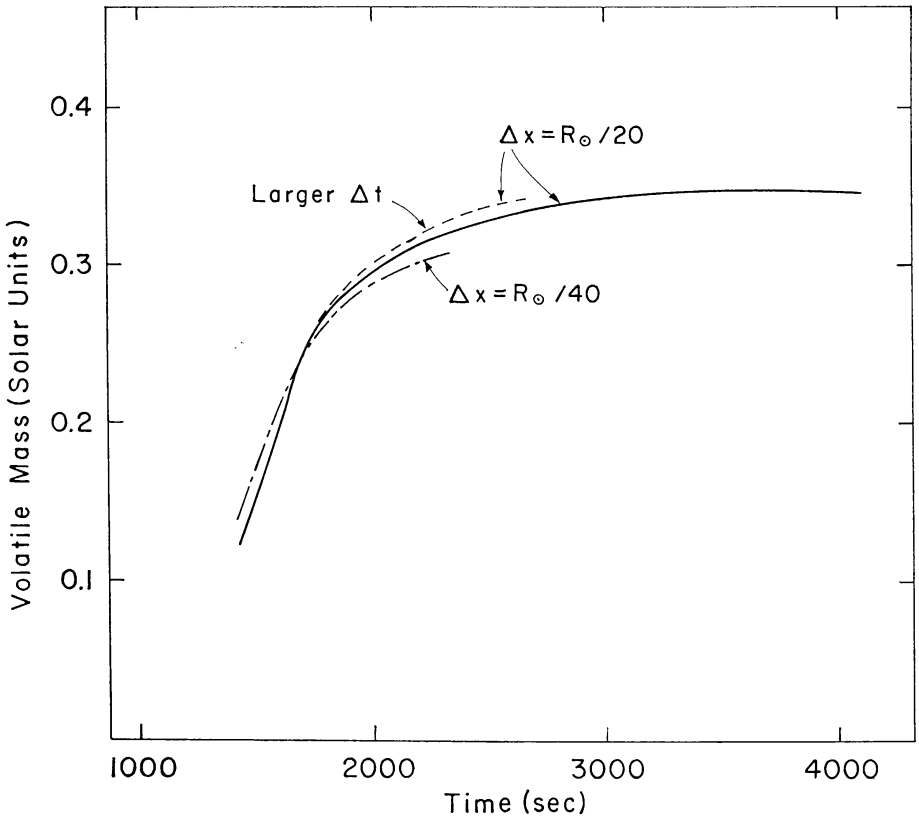

Fig. 13. Volatile mass *vs.* time following a head-on collision between solar-like polytropes initially having a relative velocity of 1000 km s^{-1} at infinite separation. Here the variation with mesh width Δx is relatively small.

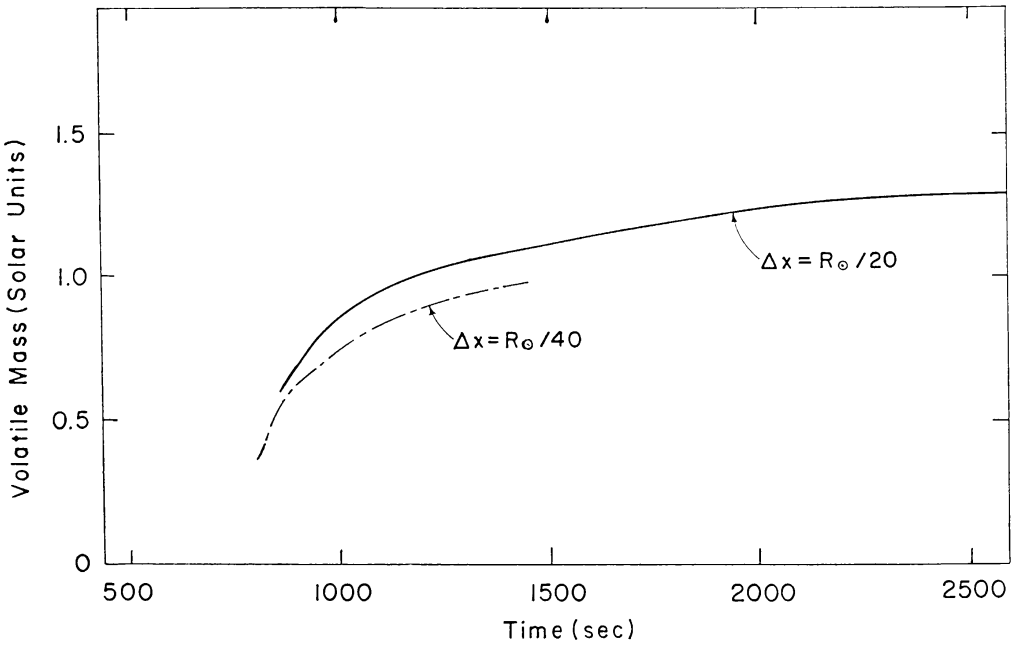

Fig. 14. Volatile mass *vs.* time during late stages of a head-on collision between two solar-like polytropes initially closing with a relative velocity of 2000 km s^{-1} at infinite separation. In contrast to the case of Figure 12, the calculated volatile mass appears to decrease as mesh width Δx is reduced.

The $5^{+1.5}_{-0.5}\%$ mass loss, found for the collision between polytropes with *zero* initial relative velocity at infinity, compares reasonably well with the seven percent mass loss found in the calculation by Mathis (1967).

Acknowledgments

This research has been supported in part by grants from the National Aeronautics and Space Administration and the National Science Foundation.

References

Allen, C. W.: 1963, *Astrophysical Quantities*, The Athlone Press, London.
Chandrasekhar, S.: 1939, *Stellar Structure*, Dover Publications, New York.
Colgate, S. A.: 1967, *Astrophys. J.* **150**, 163.
De Young, D. S.: 1968, *Astrophys. J.* **153**, 633.
De Young, D. S. and Axford, W. I.: 1967, *Nuovo Cim.* **50**, 199.
Forsythe, G. E. and Wasow, W. R.: 1960, *Finite-Difference Methods for Partial Differential Equations*, John Wiley and Sons, New York and London.
Gold, T., Axford, W. I., and Ray, E. C.: 1965, in *Quasi-Stellar Sources and Gravitational Collapse* (ed. by I. Robinson, A. Schild, and E. L. Schucking), University of Chicago Press, Chicago.
Harlow, F. H. and Shannon, J. P.: 1967, *J. Appl. Phys.* **38**, 3855.
Lax, P. D. and Wendroff, B.: 1960, *Comm. Pure Appl. Math.* **13**, 217.
Mathis, J. S.: 1967, *Astrophys. J.* **147**, 1050.
Neumann, J. von and Richtmyer, R. D.: 1950, *J. Appl. Phys.* **21**, 232.
Richtmyer, R. D. and Morton, K. W.: 1967, *Difference Methods for Initial-Value Problems*, Interscience Pub., New York.
Sakurai, A.: 1960, *Comm. Pure Appl. Math.* **13**, 353.
Sanders, R. H.: 1970, *Astrophys. J.* **162**, 791.
Spitzer, L. and Saslaw, W. C.: 1966, *Astrophys. J.* **143**, 400.
Woltjer, L.: 1964, *Nature* **201**, 803.
Zel'dovich, Y. B. and Raizer, Y. P.: 1966, Vol. I, and 1967, Vol. II, *Physics of Shock Waves and High-Temperature Hydrodynamic Phenomena* (ed. by W. D. Hayes and R. F. Probstein), Academic Press, New York and London.

APPENDIX

Numerical program (cylindrical symmetric) for handling compressible self-gravitating fluids with free boudaris

F. G. P. SEIDL

1. Introduction

The present numerical program is designed to handle problems of compressible self-gravitating fluids, which can have free-moving boundaries and may involve hydrodynamic shocks. The gravitational field calculations make use of the integral formulation for the solution of Poisson's equation, an approach which results in straightforward answers in the neighborhoods of free-moving boundaries. The hydro-

dynamics of such boundaries are treated approximately by allowing the set of difference equations complete control unless the density ϱ drops below some small prescribed value $|\varepsilon|$; i.e., whenever $\varrho < |\varepsilon|$ at some point, ϱ and all the other dependent variables are set to *zero* at that point. This procedure is likely to be acceptable for certain stellar calculations where the densities near moving boundaries are less than those in stellar interiors by many orders of magnitude. All current calculations are limited to cylindrically symmetric cases, the independent variables being the spatial variables r, z and the time t.

An Eulerian representation is used since otherwise it is difficult to allow for sufficient freedom of fluid motion and change of shape; i.e., the fluid is assumed to move with respect to the cylindrical coordinate system. Moreover, there must be room in the finite-difference network for some translation of the stellar models. As a consequence, only a limited number of netpoints are available for defining the density distribution of a star. In order to reduce the necessary netpoints per stellar radius and yet handle a large range of density (e.g., at least a range of 10^6), a second-order difference scheme is employed, viz., accurate to second-order in the small quantities Δr, Δz, Δt.

The difference scheme resembles Richtmyer's (1962) and Richtmyer and Morton's (1967) two-step modification of the Lax-Wendroff method (1960, 1964). One step involves calculating variables at intermediate netpoints which then are used in a second step where the variables at primary netpoints are evaluated to full precision. A significant part of the procedure, as Lax (1957) and Richtmyer and Morton (1967, p. 305) have pointed out, is that the space differencing be carried out directly on equations written in so-called conservation form (Lax 1954, 1957), a feature which makes the difference equations themselves obey the conservation laws exactly. But perhaps even more important, the Lax-Wendroff method afford a rather elegant means of choosing dependent variables which are consistent with the shock-jump conditions determined by physical principles. The introduction of the gravitational field forces some departure from strict conservation form. However, if the gravitational potential Φ is differentiable with respect to the space variables (the assumed physical model meets this requirements), weak solutions can be shown to exist which properly involve the dependent variables in the physically correct jump conditions.

In the case of nonlinear equations such as are involved here, the jump conditions have to be supplemented if a unique solution is to be obtained for a particular problem, e.g., by the so-called 'entropy' condition (Lax, 1957). It is conjectured that in the present work the necessary supplementary condition comes about through the artificial viscosity (von Neumann and Richtmyer, 1950; Lax and Wendroff, 1960), a device also needed for damping certain oscillations in the difference solutions which are not representative of actual fluid behavior. By way of justification, it may be noted that, for a locally one-dimensional system, the correct solution is the one where the entropy of a fluid particle increases as it crosses a shock front (Lax, 1957); and, the artificial viscosity, when applied in the right way, induces very nearly the correct entropy jump across a simulated shock (von Neumann and Richtmyer, 1950).

Although considerable success has been achieved in establishing the validity of the numerical solutions of linear differential equations (cf. Lax's equivalence theorem as discussed by Richtmyer and Morton (1967); see also Kreiss (1964, 1966, 1968, etc.), uncertainties remain in the case of quasilinear equations, such as employed here. The problem concerns the convergence of the numerical solutions to those of the differential equations. A simple experimental test has been made (cf. Section 7), but this remains insufficient. The nearest thing we know to mathematical justification is a theorem due to Strang (1964) on difference approximations for quasilinear hyperbolic initial-value problems. He has demonstrated convergence for explicit difference schemes under the following conditions: (1) The equations and the *exact* solution possess a sufficient degree of smoothness to make Taylor expansion meaningful. (2) There are limits on the domain of dependence which are assured by stipulating hyperbolicity. (3) The first variation of the difference scheme is stable. And, (4) the difference scheme is consistent with the basic differential equations. Consistency is, of course, a formal way of requiring that the difference operator approach the differential operator as Δx, $\Delta t \to 0$. Strang's treatment shows the immense importance of consistency and stability for convergence – two conditions which we endeavor to satisfy. However, our program must allow shocks, and thus the solutions belong to a class (weak solutions) more properly determined by the integral version of the conservation laws and which in the large does not possess the smoothness necessary for Strang's proof.

2. Basic Equations

The equations set out below are the divergence formulation of the conservation of mass, Newton's second law, and the conservation of energy expressed in terms of the cylindrical coordinates r, θ, z, where all derivatives with respect to θ vanish due to symmetry. The tangential velocity v and associated inertial forces are included here for completeness. However, these quantities are zero in the current colliding-star calculations; and, hence, will be omitted from the subsequent difference equations.

The formula derived from the conservation of mass is

$$\varrho_t = -\frac{1}{r}(r\varrho u)_r - (\varrho w)_z = -\nabla\cdot\varrho\mathbf{U} \tag{A1}$$

where ϱ denotes fluid density and $\mathbf{U}$ the fluid velocity vector

$$\mathbf{U} = u\cdot\mathbf{e}_r + v\cdot\mathbf{e}_\theta + w\cdot\mathbf{e}_z \tag{A2}$$

$\mathbf{e}_r$, $\mathbf{e}_\theta$, $\mathbf{e}_z$ being unit orthogonal vectors attached to the local cylindrical coordinate frame; u is the radial, v the tangential, and w the axial velocity component.

Conservation of momentum yields the following equations:

$$(\varrho u)_t = -\frac{1}{r}(r\varrho u^2 + rP)_r - (\varrho uw)_z + \varrho\frac{v^2}{r} + \frac{1}{r}P + \varrho\Phi_r \tag{A3}$$

$$(\varrho v)_t = -\frac{1}{r}(r\varrho vu)_r - (\varrho vw)_z - \varrho\frac{uv}{r}, \tag{A4}$$

$$(\varrho w)_t = -\frac{1}{r}(r\varrho wu)_r - (\varrho w^2 + P)_z + \varrho\Phi_z, \tag{A5}$$

where P denotes fluid pressure and Φ gravitational potential. Since Φ is always differentiable with respect to r and z [cf. Equation (A6)], the use of (ϱu), (ϱv), (ϱw) as dependent variables rather than u, v, w leads directly, according to the theory of weak solutions (cf. Lax, 1957; Courant and Hilbert, 1962), to a momentum jump across a shock front that satisfies Newton's second law. Otherwise, Equations (A1) through (A5) and (A7) are equivalent to the standard Eulerian fluid-dynamic equations (e.g., Landau and Lifshitz, 1959).

The gravitational potential $\Phi(r, z, t)$ is obtained from the integral

$$\Phi(r, z, t) = G\int^{V(t)} \frac{\varrho(r', z', t)}{|\mathbf{r}' - \mathbf{r}|}\,\mathrm{d}V(r', z') \tag{A6}$$

$V(t)$ denoting the volume within which $\varrho(r, z, t)$ is non-vanishing. Equation (A6) is, of course, the well-known integral expression for the solution of Poisson's equation.

Application of the conservation of energy leads to the equation

$$(\varrho E)_t = -\frac{1}{r}(r\varrho Eu)_r - (\varrho Ew)_z - P\left(\frac{1}{r}(ru)_r + w_z\right), \tag{A7}$$

where E denotes the thermodynamic internal energy per unit mass of fluid. While the above equation has advantages of simplicity, the conservation of energy is perhaps more properly expressed in terms of the total energy per unit volume excluding gravitational, viz., $\varepsilon = [(\varrho u)^2 + (\varrho w)^2]/2\varrho + \varrho E$; then, since Φ is differentiable, the theory of weak solutions readily yields the physically correct jump conditions across an arbitrary shock front. Such considerations are important because different jump conditions are obtained across a shock discontinuity depending upon the form of the governing differential equations (e.g., Kasahara and Houghton, 1969), and a form must be chosen that results in the proper jump conditions corresponding to physical principles. However, the use of Equation (A7) is to some extent justified as follows: An integral version of the physical relationship expressed by Equation (A7) states that the time rate of change in internal energy of a small fluid element [viz., $\int_\varepsilon (\varrho E)_t\,\mathrm{d}V + \oint_{\partial\varepsilon} \varrho E\mathbf{v}\cdot\mathrm{d}\mathbf{S}$] is approximately equal to the negative of an average pressure multiplied by the rate of change of the element's volume $[-\bar{P}\oint_{\partial\varepsilon}\mathbf{v}\cdot\mathrm{d}\mathbf{S}]$. Let us apply this interpretation to a very thin flat element of fluid containing a portion of a shock front. The flat dimensions of the element are parallel to the front, and the element as a whole moves with the fluid in the Lagrangian sense. The time rate of change in internal energy of the fluid within the element is then

$$s(\varrho_2 E_2 - \varrho_1 E_1) - \varrho_2 E_2 w_2 + \varrho_1 E_1 w_1$$

per unit area of the front, where s denotes the shock speed, w the fluid velocity normal to the shock front, and the subscripts 1 refer to conditions ahead of the shock, subscripts 2 refer to conditions immediately behind. On the other hand, the rate of change in the volume of the fluid element is $w_1 - w_2$ per unit area of the front, thus

$$s(\varrho_2 E_2 - \varrho_1 E_1) = \varrho_2 E_2 w_2 - \varrho_1 E_1 w_1 + \bar{P}(w_2 - w_1). \tag{a}$$

By comparison, the physically correct jump condition for internal energy ϱE is

$$s(\varrho_2 E_2 - \varrho_1 E_1) = \varrho_2 E_2 w_2 - \varrho_1 E_1 w_1 + [(P_2 + P_1)/2](w_2 - w_1). \tag{b}$$

The similarity of Equations (a) and (b) supports the view that Equation (A7) is valid about shock fronts; while, elsewhere the validity of Equation (A7) is not in question.

To complete the definition of the system, an equation of state is necessary; currently that for an ideal gas is used, viz.,

$$\varrho E = P/(\gamma - 1) \tag{A8}$$

γ being a characteristic constant of the fluid. If this value for E is substituted into Equation (A7), an equation for P results

$$P_t = -\frac{1}{r}(rPu)_r - (Pw)_z - (\gamma - 1)P\left(\frac{1}{r}(ru)_r + w_z\right). \tag{A9}*$$

Besides the above relations, it may be desirable to imagine an artificial viscosity included in the basic system of differential equations. This can be done by adding the following term to the pressure P in places where the latter is engaged in doing work (von Neumann and Richtmyer, 1950; Richtmyer and Morton, 1967)

$$q = \begin{cases} q_0 h^2 \varrho (\nabla \cdot \mathbf{U})^2 & \text{if} \quad \nabla \cdot \mathbf{U} < 0 \\ 0, & \text{if} \quad \nabla \cdot \mathbf{U} \geqslant 0, \end{cases} \tag{A10}$$

where h is a characteristic length (e.g., $h = \Delta r = \Delta z$) and q_0 a constant of order unity. The introduction of q means adding $-q_r$ and $-q_z$ to the righthand sides of the momentum equations (A3) and (A5) respectively; while, Equation (A9) becomes

$$P_t = -\frac{1}{r}(rPu)_r - (Pw)_z - (\gamma - 1)(P + q)\left(\frac{1}{r}(ru)_r + w_z\right). \tag{A11}$$

An alternate form of artificial viscosity (Lapidus, 1967) is discussed later under controls needed for stability (cf. Section 6).

3. The Finite-Difference Network and Its Boundary Conditions

A rectangular network is employed with basic spacings $\Delta r = \Delta z = h$, where r and z are cylindrical coordinates. There is a primary lattice of netpoints and two secondary lattices staggered with respect to the first both in space and time. One secondary

* This equation may be written in conservation form: $(P^{1/\gamma})_t + 1/r(ruP^{1/\gamma})_r + (wP^{1/\gamma})_z = 0$. However, then the resulting jump conditions would not be physically correct.

lattice is shifted by $h/2$ to the right of the primary lattice; the other is shifted upwards by $h/2$; and, these determine a system of secondary mesh points. Variables evaluated at the secondary points are used in the determination of values at the primary points where the full second-order accuracy is obtained. The current calculations employ a network of 128 by 128 primary points.

Variables determined at the primary points are written $X^n_{i,j}$; the radial cylindrical index being $i=1, 2, \ldots I$; the z-axis index is $j=1, 2, \ldots J$; and the time index n. Consequently, the r-coordinate of the point i, j is

$$r_i = (i-1)h \tag{A12}$$

while the z-coordinate is

$$z_j = (j-1)h\,. \tag{A13}$$

Variables at secondary netpoints are written $X^{n+1/2}_{i+1/2,\,j}$ and $X^{n+1/2}_{i,\,j+1/2}$ (cf. Figure A1), thereby implying that they are evaluated at intermediate times such as $t^{n+1/2} = \frac{1}{2}(t^{n+1}+t^n)$, where $t^{n=1}=0$.

The fixed boundary conditions arise chiefly from (1) cylindrical symmetry about the z-axis, and (2) mirror-like symmetry across the plane perpendicular to this axis at $z=0$. Because of this symmetry only one quadrant of a three-dimensional physical space has to be included in the domain of calculation (cf. Figure A2). Since the

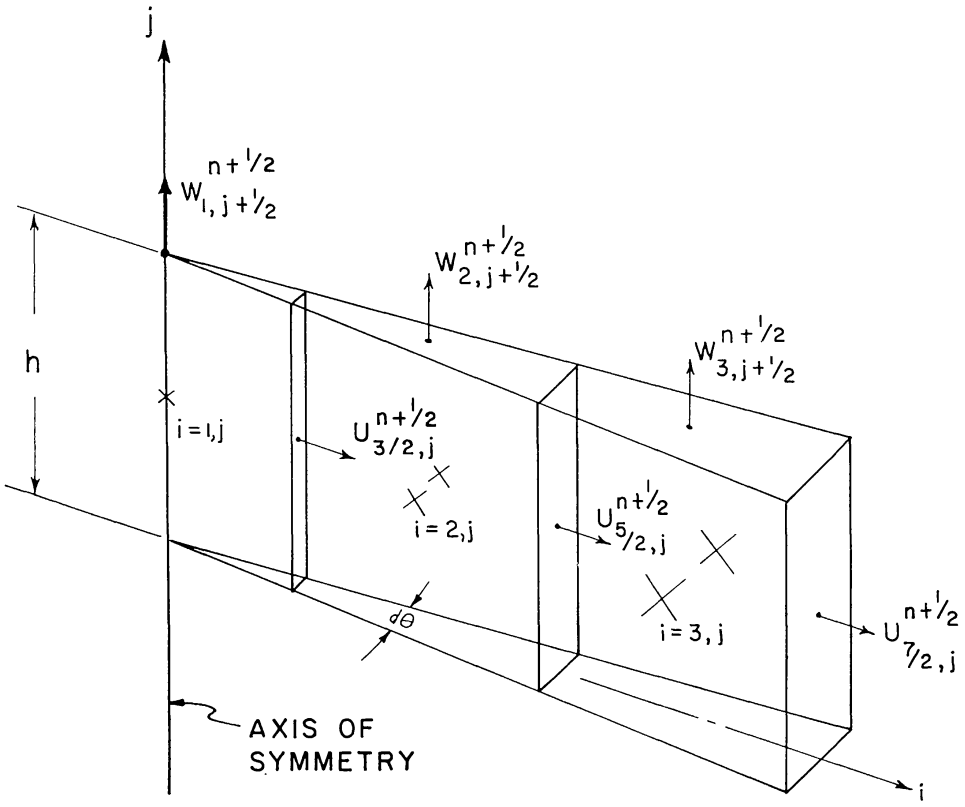

Fig. A1. Basic finite-difference cells.

boundary conditions are strongly defined along the z-axis and the plane of symmetry, primary netpoints are located at these places.

The domain of calculation is assumed to be bounded by rigid walls on the right where $r=(I-1)h$ and on the top where $z=(J-1)h$. During development of the program, it seemed easier to satisfy the conservation laws if such artificial rigid outer

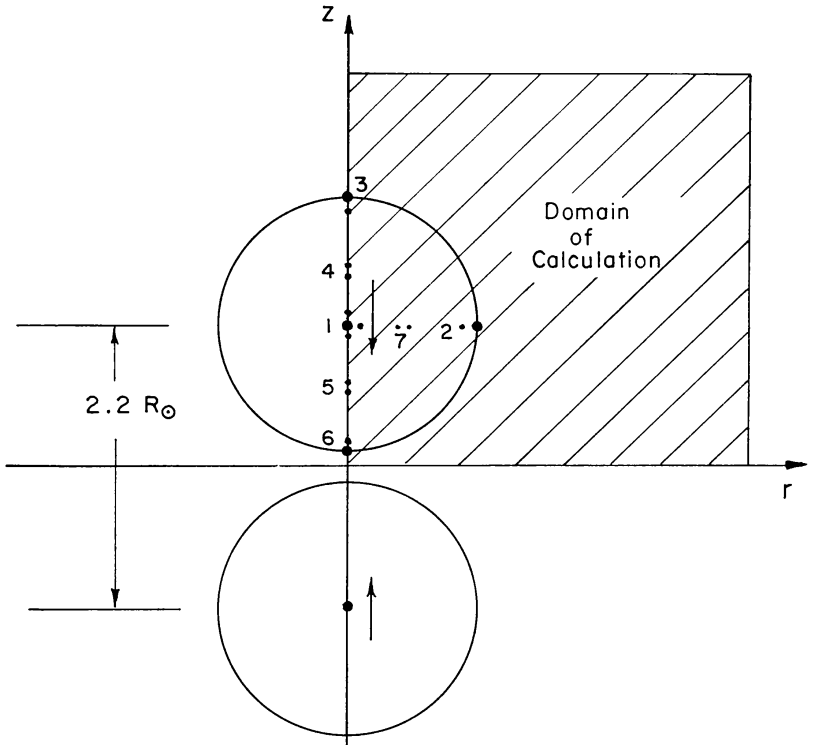

GRAVITATIONAL GRADIENTS

Location	Meaning of $\Delta\Phi$	[1] $\Delta\Phi$ (exact)	[2] $\Delta\Phi$ (numerical)
1	$\Phi_{1,23} - \Phi_{1,22}$	0.065 5149	0.064 748
1	$\Phi_{1,23} - \Phi_{1,24}$	0.089 7119	0.089 026
2	$\Phi_{20,23} - \Phi_{21,23}$	0.065 7015	0.065 922
3	$\Phi_{1,42} - \Phi_{1,43}$	0.067 4130	0.067 638
4	$\Phi_{1,32} - \Phi_{1,33}$	0.234 3510	0.234 830
5	$\Phi_{1,14} - \Phi_{1,13}$	0.206 4985	0.206 884
6	$\Phi_{1,4} - \Phi_{1,3}$	0.022 5892	0.022 664
1	$\Phi_{1,23} - \Phi_{2,23}$	0.078 0257	0.076 846
7	$\Phi_{10,23} - \Phi_{11,23}$	0.228 559	0.229 079

1. POLYTROPE OF INDEX 3. 2. $R_\odot$ INCLUDES 20 MESH POINTS

Fig. A2. A comparison of numerical and exact calculations of the gravitational gradient for a coarsely-zoned case of 20 zones per $R_\odot$.

boundaries were imposed. At a later time, it might be advantageous to change this assumption allowing an outflux of mass and energy.

Along the axis of symmetry where $r=0$ and $i=1$ the radial component of fluid velocity is assumed to vanish as well as the radial derivative of certain variables; i.e.,

$$\begin{aligned} u^n_{i,j} &= 0, \\ u^{n+1/2}_{i,j+1/2} &= 0, \end{aligned} \tag{A14}$$

and at $r=0$

$$(X \cdot w)_r = 0, \tag{A15}$$

where w denotes the axial component of fluid velocity and X represents any of the variables ϱ, ϱu, ϱv, ϱw, or pressure P. Moreover, in order to gain greater smoothness near $r=0$, the second derivative of w with respect to r may be allowed to vanish (viz., $w^n_{2,j}=w^n_{i,j}$ and $w^{n+1/2}_{2,j+1/2}=w^{n+1/2}_{i,j+1/2}$). A final useful assumption along the axis of symmetry is that, at $r=0$,

$$P_r = 0. \tag{A16}$$

On the plane of symmetry where $z=0$ and $j=1$, the z-component of fluid velocity vanishes; i.e.,

$$\begin{aligned} w^n_{i,1} &= 0, \\ w^{n+1/2}_{i+1/2,1} &= 0. \end{aligned} \tag{A17}$$

Also, because of the mirror-like symmetry across this plane, the z-component of velocity must obey the relation

$$w(r, z) = -w(r, -z), \tag{A18}$$

while for all other variables

$$X(r, z) = X(r, -z). \tag{A19}$$

Similar boundary conditions apply across the upper rigid boundary at $z=z(\max)=(J-1)h$ or $j=J$; i.e.,

$$\begin{aligned} w^n_{i,J} &= 0, \\ w^{n+1/2}_{i+1/2,J} &= 0. \end{aligned} \tag{A20}$$

Moreover, across the boundary at $j=J$

$$w(r, z) = -w(r, z'), \tag{A21}$$

where $z'=2 \cdot z(\max)-z$; and, for all other variables

$$X(r, z) = X(r, z'). \tag{A22}$$

Of course, excursions beyond the boundaries of the domain of calculation only occur in setting up boundary relations for the difference scheme and never extend by more than a few steps.

On the rigid cylindrical boundary at $r=r(\max)=(I-1)h$ and $i=I$

$$\begin{aligned} u^n_{I,j} &= 0\,, \\ u^{n+1/2}_{I,j+1/2} &= 0\,. \end{aligned} \tag{A23}$$

In addition, for arbitrary z it is imagined that the radial component of flow at a small distance inside this boundary is equal and opposite to a virtual radial flow at an equal distance outside the boundary, viz.,

$$r_{I+1/2}u^{n+1/2}_{I+1/2,j}X^{n+1/2}_{I+1/2,j} = -\,r_{I-1/2}u^{n+1/2}_{I-1/2,j}X^{n+1/2}_{I-1/2,j}\,, \tag{A24}$$

where $r_{I+1/2}=(I-\frac{1}{2})\cdot h$ and $r_{I-1/2}=(I-\frac{3}{2})\cdot h$. Except for the radius factor, Equation (A24) is analogous to the conditions across the lateral planes $z=0$ and $z=z(\max)$, where the surfaces may be imagined to behave like rigid walls undergoing elastic collisions with the fluid.

4. Difference Equations

Imagine that each primary netpoint is enclosed in a small tapered cell with rectangular sides (Figure A1). A difference analogue for the divergence of a vector quantity $X\mathbf{U}$ at an arbitrary point i,j is obtained by calculating the outflow rate across the walls of the surrounding cell and dividing the result by the cell volume: i.e.,

$$\left[\frac{1}{r}(rXu)_r\right]^{n+1/2}_{i,j} = \frac{\Delta\theta}{\Delta V_{i,j}\Delta t^{n+1/2}} \int_{t^n}^{t^{n+1}} \mathrm{d}t \int_{z_{j-1/2}}^{z_{j+1/2}} [r_{i+1/2}X(z,t)_{i+1/2}\,u(z,t)_{i+1/2} - r_{i-1/2}X(z,t)_{i-1/2}\,u(z,t)_{i-1/2}]\,\mathrm{d}z \tag{A25}$$

and

$$[(Xw)_z]^{n+1/2}_{i,j} = \frac{\Delta\theta}{\Delta V_{i,j}\Delta t^{n+1/2}} \int_{t^n}^{t^{n+1}} \mathrm{d}t \int_{r_{i-1/2}}^{r_{i+1/2}} [X(r,t)_{j+1/2}\,w(r,t)_{j+1/2} - X(r,t)_{j-1/2}\,w(r,t)_{j-1/2}]\,r\,\mathrm{d}r \tag{A26}$$

where $\Delta V_{i,j}/\Delta\theta$, the cell volume per unit angle, is

$$\Delta V_{i,j}/\Delta\theta = \begin{cases} h^3/8 & \text{when} \quad i=1 \\ (i-1)\,h^3 & \text{for} \quad i>1\,. \end{cases} \tag{A27}$$

In practice it is convenient to construct the divergence from intermediate terms $A^{n+1/2}_{i+1/2,j}$ and $B^{n+1/2}_{i,j+1/2}$, which can be worked out from Equations (A25) and (A26) in accord with the boundary conditions of Section 3. Thus,

$$\left[\frac{1}{r}(rXu)_r\right]^{n+1/2}_{i,j} = \begin{cases} \dfrac{1}{(i-1)h^3}(A^{n+1/2}_{i+1/2,j} - A^{n+1/2}_{i-1/2,j}), & \text{if} \quad 1<i<I \\ +\dfrac{8}{h^3}A^{n+1/2}_{3/2,j}\,, & \text{if} \quad i=1 \\ \dfrac{-2}{(I-1)h^3}A^{n+1/2}_{I-1/2,j}\,, & \text{for} \quad i=I \end{cases} \tag{A28}$$

it being understood that Equation (A24) is used when $i=I$; and,

$$[(Xw)_z]^{n+1/2}_{i,j} = \frac{1}{(i-1)h^3}\begin{cases}(B^{n+1/2}_{i,j+1/2} - B^{n+1/2}_{i,j-1/2}), & \text{if} \quad 1<j<J \quad \text{and} \quad i>1\\ +2\,B^{n+1/2}_{i,3/2}, & \text{if} \quad j=1 \quad \text{and} \quad i>1\\ -2\,B^{n+1/2}_{i,J-1/2}, & \text{if} \quad j=J \quad \text{and} \quad i>1\end{cases} \tag{A29}$$

$$[(Xw)_z]^{n+1/2}_{1,j} = \frac{8}{h^3}\begin{cases}(B^{n+1/2}_{1,j+1/2} - B^{n+1/2}_{1,j-1/2}), & \text{if} \quad 1<j<J \quad \text{and} \quad i=1\\ +2\,B^{n+1/2}_{1,3/2}, & \text{if} \quad j=1 \quad \text{and} \quad i=1\\ -2\,B^{n+1/2}_{1,J-1/2}, & \text{if} \quad j=J \quad \text{and} \quad i=1\end{cases} \tag{A30}$$

where

$$A^{n+1/2}_{i+1/2,j} = \frac{1}{\Delta t^{n+1/2}}\int_{t^n}^{t^{n+1}} \mathrm{d}t \int_{z_{j-1/2}}^{z_{j+1/2}} r_{i+1/2} X(z,t)_{i+1/2}\, u(z,t)_{i+1/2}\, \mathrm{d}z \tag{A31}$$

and

$$B^{n+1/2}_{i,j+1/2} = \frac{1}{\Delta t^{n+1/2}}\int_{t^n}^{t^{n+1}} \mathrm{d}t \int_{r_{i-1/2}}^{r_{i+1/2}} X(r,t)_{j+1/2}\, w(r,t)_{j+1/2}\, r\, \mathrm{d}r \tag{A32}$$

In Equation (A31) it should be understood that for $j=1$, $z_{j+1/2}=+h/2$, $z_{j-1/2}=-h/2$; also, the relations expressed by Equations (A18) and (A19) apply; similarly at $j=J$. Since $A^{n+1/2}_{i+1/2,j}$ and $B^{n+1/2}_{i,j+1/2}$ are evaluated at secondary mesh points which are nested between primary points, the range of i for $A^{n+1/2}_{i+1/2,j}$ is $i=1, I-1$; while for $B^{n+1/2}_{i,j+1/2}$ $j=1$ to $J-1$. When $i=1$, $r_{i-1/2}$ in Equation (A32) is taken to be *zero*.

Except for possible small damping terms (cf. Section 6), $A^{n+1/2}_{i+1/2,j}$ and $B^{n+1/2}_{i,j+1/2}$ are calculated by the following approximate formulas:

$$\begin{aligned}A^{n+1/2}_{i+1/2,j} \simeq\ & hr_{i+1/2}[(Xu)^{n+1/2}_{i+1/2,j}(1-\varepsilon^n_{x,j}) + \varepsilon^n_{x,j}(Xu)^n_{x,j}] + \\ & + hr_{i+1/2}\begin{cases}\frac{1}{24}[(Xu)^{n+1/2}_{i+1/2,j+1} - 2(Xu)^{n+1/2}_{i+1/2,j} + (Xu)^{n+1/2}_{i+1/2,j-1}], & \text{if} \quad 1<j<J\\ \frac{1}{12}[(Xu)^{n+1/2}_{i+1/2,2} - (Xu)^{n+1/2}_{i+1/2,1}], & \text{if} \quad j=1.\\ \frac{1}{12}[(Xu)^{n+1/2}_{i+1/2,J-1} - (Xu)^{n+1/2}_{i+1/2,J}], & \text{if} \quad j=J\end{cases}\end{aligned} \tag{A33}$$

The dominant term here is $(Xu)^{n+1/2}_{i+1/2,j} = X^{n+1/2}_{i+1/2,j} u^{n+1/2}_{i+1/2,j}$. The special subscript x equals either i or $i+1$ depending upon the direction of flow; viz.,

$$x = \begin{cases} i, & \text{if} \quad r_{i+1}u^n_{i+1,j} + r_i u^n_{i,j} \geqslant 0\\ i+1, & \text{if} \quad r_{i+1}u^n_{i+1,j} + r_i u^n_{i,j} < 0\end{cases} \tag{A34}$$

and

$$\varepsilon^n_{x,j} = \varepsilon_0 \frac{r_x}{r_{i+1/2}} \frac{|u^n_{x,j}|\,\Delta t^{n+1/2}}{h} \tag{A35}$$

ε_0 is termed the 'flow-bias' factor, its value being $0<\varepsilon_0<2$. The optimum value of ε_0 (viz., from the standpoint of preserving overall energy conservation) is found by trial and error; it appears to depend upon the average values of Δt and $(u^2+w^2)^{1/2}/c$, c denoting the speed of sound. Flow-bias originates from a view that the flow across

an arbitrary surface element during the interval $\Delta t^{n+1/2}=t^{n+1}-t^n$ is affected by the values of variables at the slightly earlier time t^n on the upstream side (cf. suggestion attributed to Lelevier, p. 292, Richtmyer and Morton, 1967). On the other hand, additional terms like (1/24) $[(X\,u)^{n+1/2}_{i+1/2,\,j+1}-2(X\,u)^{n+1/2}_{i+1/2,\,j}+(X\,u)^{n+1/2}_{i+1/2,\,j-1}]$ correct for variations along the z-direction, the direction perpendicular to the component of flow represented by $A^{n+1/2}_{i+1/2,\,j}$. The quantities like $(X\,u)^{n+1/2}_{i+1/2,\,j}\equiv X^{n+1/2}_{i+1/2,\,j}\,u^{n+1/2}_{i+1/2,\,j}$, later $(Xw)^{n+1/2}_{i,\,j+1/2}\equiv X^{n+1/2}_{i,\,j+1/2}\,w^{n+1/2}_{i,\,j+1/2}$, involve the variables determined at secondary netpoints.

In setting up expressions for $B^{n+1/2}_{i,\,j+1/2}$ it is assumed that at $r=0$ (viz., $i=1$) certain first derivatives with respect to r vanish [cf. Equation (A15)]. Hence, for $i=1$

$$B^{n+1/2}_{1,\,j+1/2}\simeq\frac{h^2}{8}\left[(Xw)^{n+1/2}_{1,\,j+1/2}\,(1-\varepsilon^n_{1,\,y})+\varepsilon^n_{1,\,y}\,(Xw)^n_{1,\,y}\right]+$$
$$+\frac{h^2}{64}\left[(Xw)^{n+1/2}_{2,\,j+1/2}-(Xw)^{n+1/2}_{1,\,j+1/2}\right]. \tag{A36}$$

Otherwise,

$$B^{n+1/2}_{i,\,j+1/2}\simeq hr_i\left[(Xw)^{n+1/2}_{i,\,j+1/2}\,(1-\varepsilon^n_{i,\,y})+\varepsilon^n_{i,\,y}\,(Xw)^n_{i,\,y}\right]+$$
$$+h\begin{cases}\frac{1}{24}\left[r_{i+1}\,(Xw)^{n+1/2}_{i+1,\,j+1/2}-2r_i\,(Xw)^{n+1/2}_{i,\,j+1/2}+r_{i-1}\,(Xw)^{n+1/2}_{i-1,\,j+1/2}\right], & \text{if}\quad 1<i<I\\ \frac{1}{12}\left[r_{I-1}\,(Xw)^{n+1/2}_{I-1,\,j+1/2}-r_I\,(Xw)^{n+1/2}_{I,\,j+1/2}\right], & \text{for}\quad i=I\end{cases} \tag{A37}$$

where

$$y=\begin{cases}j, & \text{if}\quad w^n_{i,\,j+1}+w^n_{i,\,j}\geqslant 0\\ j+1, & \text{if}\quad w^n_{i,\,j+1}+w^n_{i,\,j}<0\end{cases} \tag{A38}$$

and

$$\varepsilon^n_{i,\,y}=\varepsilon_0\frac{|w^n_{i,\,y}|\,\Delta t}{h}. \tag{A39}$$

Here the dominant term is $(Xw)^{n+1/2}_{i,\,j+1/2}$; and, for $i=I$ it is assumed that $r_{I+1}\,(X\,w)^{n+1/2}_{I+1,\,j+1/2}=r_{I-1}\,(X\,w)^{n+1/2}_{I-1,\,j+1/2}$.

The advance in time of variables at primary netpoints is determined by difference formulas derived from the conservation of mass, momentum, and energy, use being made of the difference analogue for the divergence. Let us begin with the formula for advancing the density ϱ

$$\varrho^{n+1}_{i,\,j}=\varrho^n_{i,\,j}-\Delta t^{n+1/2}\times(\nabla\cdot\varrho\mathbf{U})^{n+1/2}_{i,\,j}=\varrho^n_{i,\,j}-\Delta t^{n+1/2}\times$$
$$\times\left\{\left[\frac{1}{r}(r\varrho u)_r\right]^{n+1/2}_{i,\,j}+\left[(\varrho w)_z\right]^{n+1/2}_{i,\,j}\right\}. \tag{A40}$$

After computing density, the device which controls the free-moving boundaries is applied; i.e.,

$$\text{if}\quad \varrho^{n+1}_{i,\,j}<|\varepsilon|,\begin{cases}\varrho^{n+1}_{i,\,j}=0,\\ u^{n+1}_{i,\,j}=0,\\ w^{n+1}_{i,\,j}=0,\\ P^{n+1}_{i,\,j}=0,\end{cases} \tag{A41}$$

The *density cutoff* $|\varepsilon|$ is usually set to 10^{-6} in units where the initial central stellar density is *one*; this value strikes a balance between machine running-time and mass loss. The effect on running-time comes about as follows: When $|\varepsilon|$ is changed from 10^{-6} to 10^{-7}, the number and size of spurious velocity fluctuations increase in certain regions of lowest densities ($10^{-6} \gtrsim \varrho > 10^{-7}$). The larger velocity peaks cause smaller time steps Δt due to the Courant condition, which is necessary for stability [cf. Equation (A70)]. On the other hand, the device of Equations (A41) aids in decreasing running-time because it serves as a criterion for defining the active regions where the fluid density is nontrivial, and beyond which the difference calculations need not be extended.

The calculation of the von Neumann-Richtmyer artificial viscosity $q_{i,j}^{n+1/2}$ is carried out according to the expression

$$q_{i,j}^{n+1/2} = \begin{cases} 0, & \text{if} \quad (\nabla \cdot \mathbf{U})_{i,j}^{n+1/2} \geqslant 0 \\ + q_0 h^2 \varrho_{i,j}^{n+1/2} [(\nabla \cdot \mathbf{U})_{i,j}^{n+1/2}]^2 & \text{otherwise.} \end{cases} \tag{A42}$$

The constant q_0 lies in the range $0 < q_0 < +3$.

Pressure is advanced by means of an equation based on the local conservation of energy [cf. Equation (A11)]

$$P_{i,j}^{n+1} = P_{i,j}^{n} - \Delta t^{n+1/2} \times \\ \times [(\nabla \cdot P\mathbf{U})_{i,j}^{n+1/2} + (\gamma - 1)(\bar{P}_{i,j}^{n+1/2} + q_{i,j}^{n+1/2})(\nabla \cdot \mathbf{U})_{i,j}^{n+1/2}], \tag{A43}$$

where $P_j^{n+1/2}$ is set to *zero* whenever the above equation yields a value less than zero. The quantity $\bar{P}_j^{n+1/2}$ is an average computed from

$$\bar{P}_{i,j}^{n+1/2} = \begin{cases} \frac{1}{4}\left(P_{i+1/2,j}^{n+1/2} + P_{i-1/2,j}^{n+1/2} + P_{i,j+1/2}^{n+1/2} + P_{i,j-1/2}^{n+1/2} + \right. \\ \qquad \left. + \dfrac{P_{i+1/2,j}^{n+1/2} - P_{i-1/2,j}^{n+1/2}}{6i-6}\right), \quad \text{if} \quad 1 < i < I \\ \frac{1}{4}\left(\dfrac{9P_{3/2,j}^{n+1/2} - P_{5/2,j}^{n+1/2}}{4} + P_{1,j+1/2}^{n+1/2} + P_{1,j-1/2}^{n+1/2}\right) \quad \text{for} \quad i = 1, \\ \frac{1}{3}\left(\dfrac{I - \frac{3}{2}}{I-1} P_{I-1/2,j}^{n+1/2} + P_{I,j+1/2}^{n+1/2} + P_{I,j-1/2}^{n+1/2}\right) \qquad \text{for} \quad i = I. \end{cases} \tag{A44}$$

These relations apply for all j, $1 \leqslant j \leqslant J$, if it is understood that $P_{i,1/2}^{n+1/2} = P_{i,3/2}^{n+1/2}$ and $P_{i,J+1/2}^{n+1/2} = P_{i,J-1/2}^{n+1/2}$ [cf. Equations (A19) and (A22)]. The top expression in Equation (A44) results from the cylindrically weighted average of quantities assumed to vary linearly between netpoints. The first part of the middle expression (i.e., for $i=1$) was derived by fitting a second-degree polynomial through values of P at $i=\frac{3}{2}$ and $\frac{5}{2}$ subject to the condition that $P_r(0)=0$ [cf. Equation (A16)].

It is significant that $-q_{i,j}^{n+1/2}(\nabla \cdot \mathbf{U})_{i,j}^{n+1/2} \geq 0$ in Equation (A43). Thus, q acts only to increase the internal energy, which is given by $\varrho E = P/(\gamma - 1)$ per unit volume. In this way, when q and other small dissipative terms are properly adjusted, they

work to induce very nearly the correct entropy jump across a simulated shock front (von Neumann and Richtmyer, 1950).

The gravitational potential Φ is calculated (cf. Section 5) by a summation like

$$\Phi_{i,j}^{n+1} = \sum_{l,m} \varrho_{l,m}^{n+1} \cdot g_{i,l,j,m} \tag{A45}$$

where

$$g_{i,l,j',m'} = g_{i,l,j,m} = g_{i,l,k} \quad \text{if} \quad |j' - m'| = |j - m| = k - 1 .$$

The $g_{i,l,k}$ are calculated in advance and stored for subsequent use. When only one quadrant of the physical space is handled by the difference scheme, the calculations of gravitational field must, of course, be adjusted to yield results corresponding to the complete space. In this case, the above equation takes the form

$$\Phi_{i,j}^{n+1} = \sum_{l=1}^{I} \varrho_{l,m=1}^{n+1} g_{i,l,k=j} + \sum_{\substack{l=1 \\ m=2}}^{I,J} \varrho_{l,m}^{n+1} \left(g_{i,l,k'=|j-m|+1} + g_{i,l,k''=j+m-1} \right). \tag{A46}$$

The $g_{i,l,k'}$ belong to sources lying above the lateral symmetry plane and the $g_{i,l,k''}$ below. In Equation (A46) the summation over source points l, m of non-zero density must be carried out for each active netpoint i, j. Since this is a time-consuming process, the summation subroutine has been optimized (Paul Schneck) using basic assembly language.

The formulas for advancing the momentum components ϱu and ϱw are set out below

$$(\varrho u)_{i,j}^{n+1} = (\varrho u)_{i,j}^{n} - \Delta t^{n+1/2} \left\{ \left[\frac{1}{r} (r\varrho u^2 + rP)_r \right]_{i,j}^{n+1/2} + \left[(\varrho uw)_z \right]_{i,j}^{n+1/2} + \right.$$
$$\left. + \frac{1}{h} \left[- \varrho_{i,j}^{n+1/2} \times (h\Phi_r)_{i,j}^{n+1/2} - \frac{\bar{P}_{i,j}^{n+1/2}}{i-1} + \tfrac{1}{2} (q_{i+1,j}^{n+1/2} - q_{i-1,j}^{n+1/2}) \right] \right\} \tag{A47}$$

and

$$(\varrho w)_{i,j}^{n+1} = (\varrho w)_{i,j}^{n} - \Delta t^{n+1/2} \left\{ \left[\frac{1}{r} (r\varrho wu)_r \right]_{i,j}^{n+1/2} + \left[(\varrho w^2 + P)_z \right]_{i,j}^{n+1/2} + \right.$$
$$\left. + \frac{1}{2h} \left[- \varrho_{i,j}^{n+1/2} (\Phi_{i,j+1}^{n+1/2} - \Phi_{i,j-1}^{n+1/2}) + q_{i,j+1}^{n+1/2} - q_{i,j-1}^{n+1/2} \right] \right\} \tag{A48}$$

where

$$\varrho_{i,j}^{n+1/2} = \tfrac{1}{2} (\varrho_{i,j}^{n+1} + \varrho_{i,j}^{n}) \tag{A49}$$

$$\Phi_{i,j}^{n+1/2} = \tfrac{1}{2} (\Phi_{i,j}^{n+1} + \Phi_{i,1}^{n}) \tag{A50}$$

and

$$(h\Phi_r)_{i,j}^{n+1/2} = \tfrac{1}{2} (\Phi_{i+1,j}^{n+1/2} - \Phi_{i-1,j}^{n+1/2}) + \frac{\Phi_{i+1,j}^{n+1/2} - 2\Phi_{i,j}^{n+1/2} + \Phi_{i-1,j}^{n+1/2}}{12(i-1)} . \tag{A51}$$

The latter comes from the cylindrically weighted average of quantities (viz., $\Phi_{i+1,j}^{n+1/2} - \Phi_{i,j}^{n+1/2}$), which are assumed to vary linearly between netpoints.

Finally, values of the fluid velocity are obtained as follows:

$$u_{i,j}^{n+1} = (\varrho u)_{i,j}^{n+1} / \varrho_{i,j}^{n+1}$$

and

$$w_{i,j}^{n+1} = (\varrho w)_{i,j}^{n+1} / \varrho_{i,j}^{n+1} \tag{A52}$$

Next, consider the variables at secondary netpoints nested midway between the primary points along both the r and z directions, the primary variables being $X^n_{i,j}$, the secondary variables $X^{n+1/2}_{i+1/2,j}$ and $X^{n+1/2}_{i,j+1/2}$. The latter are evaluated at intermediate times $t^{n+1/2}=\frac{1}{2}(t^{n+1}+t^n)$ using difference formulas derived from the conservation laws. The starting values $\bar{X}^n_{i+1/2,j}$ and $\bar{X}^n_{i,j+1/2}$ in these formulas are obtained by averaging values of $X^n_{i,j}$ [cf. Equations (A62) and (A63)]. The secondary variables constitute the first step in obtaining primary variables to second-order precision. The procedure is consistent with a two-dimensional difference scheme proposed by Lax and Wendroff (1964). However, the stencil of netpoints is not quite the same as for Richtmyer's two-dimensional two-step method (cf. p. 361ff., Richtmyer and Morton, 1967), where provisional values are obtained at the intermediate times $t^{n+1/2}$ from starting values like

$$\bar{X}^n_{i+1/2,j}=\tfrac{1}{4}\left(X^n_{i,j}+X^n_{i+1/2,j-1/2}+X^n_{i+1,j}+X^n_{i+1/2,j+1/2}\right).$$

Two sets of formulas are given below, one for the variables $X^{n+1/2}_{i+1/2,j}$, the other for the $X^{n+1/2}_{i,j+1/2}$; their combined evaluation corresponds to the first step of Richtmyer's method. However, before they are calculated it is found that smoother values result if the von Neumann-Richtmyer artificial viscosity is advanced; i.e.,

$$q^n_{i,j}=\begin{cases}0, & \text{if} \quad (\delta U)^n_{i,j}\geqslant 0\\ q_0\varrho^n_{i,j}\left[(\delta U)^n_{i,j}\right]^2, & \text{if} \quad (\delta U)^n_{i,j}<0\end{cases} \tag{A53}$$

where

$$(\delta U)^n_{i,j}=\begin{bmatrix}\dfrac{(i-\frac{1}{2})\,\bar{u}^n_{i+1/2,j}-(i-\frac{3}{2})\,\bar{u}^n_{i-1/2,j}}{(i-1)}\\ \text{or}\\ +4\bar{u}^n_{3/2,j}, \quad \text{if} \quad i=1\\ -2\dfrac{I-\frac{3}{2}}{I-1}\,\bar{u}^n_{I-1/2,j}, \quad \text{if} \quad i=I\end{bmatrix}+\begin{bmatrix}\bar{w}^n_{i,j+1/2}-\bar{w}^n_{i,j-1/2}\\ \text{or}\\ +2\bar{w}^n_{i,3/2}, \quad \text{if} \quad j=1\\ -2\bar{w}^n_{i,J-1/2}, \quad \text{if} \quad j=J\end{bmatrix} \tag{A54}$$

To simplify the equations involving momentum let

$$\xi=\varrho u \quad \text{and} \quad \zeta=\varrho w. \tag{A55}$$

Then the equations for the $X^{n+1/2}_{i+1/2,J}$ variables are

$$\xi^{n+1/2}_{i+1/2,j}=\bar{\xi}^n_{i+1/2,j}-\frac{\Delta t^{n+1/2}}{2h}\times$$

$$\times\left\{\frac{i}{i-\frac{1}{2}}u^n_{i+1,j}\bar{\xi}^n_{i+1,j}-\frac{i-1}{i-\frac{1}{2}}u^n_{i,j}\bar{\xi}^n_{i,j}+\begin{bmatrix}(\bar{w}\bar{\xi})^n_{i+1/2,j+1/2}-(\bar{w}\bar{\xi})^n_{i+1/2,j-1/2}\\ +2\,(\bar{w}\bar{\xi})^n_{i+1/2,3/2} \quad \text{if} \quad j=1\\ -2\,(\bar{w}\bar{\xi})^n_{i+1/2,J-1/2} \quad \text{if} \quad j=J\end{bmatrix}+\right.$$

$$\left.+P^n_{i+1,j}+q^n_{i+1,j}-P^n_{i,j}-q^n_{i,j}-\bar{\varrho}^n_{i+1/2,j}\left(\Phi^n_{i+1,j}-\Phi^n_{i,j}\right)\right\}, \tag{A56}$$

where $1\leqslant i\leqslant I-1$. In the case of the z-momentum component, for $1<j<J$,

$$\zeta^{n+1/2}_{i+1/2,j} = \bar{\zeta}^{n}_{i+1/2,j} - \frac{\Delta t^{n+1/2}}{2h} \times$$
$$\times \left\{ \frac{i}{i-\frac{1}{2}} u^{n}_{i+1,j}\zeta^{n}_{i+1,j} - \frac{i-1}{i-\frac{1}{2}} u^{n}_{i,j}\zeta^{n}_{i,j} + (\bar{w}\bar{\zeta})^{n}_{i+1/2,j+1/2} - (\bar{w}\bar{\zeta})^{n}_{i+1/2,j-1/2} + \right.$$
$$+ (\bar{P}+\bar{q})^{n}_{i+1/2,j+1/2} - (\bar{P}+\bar{q})^{n}_{i+1/2,j-1/2} -$$
$$\left. - \bar{\varrho}^{n}_{i+1/2,j}(\bar{\Phi}^{n}_{i+1/2,j+1/2} - \bar{\Phi}^{n}_{i+1/2,j-1/2}) \right\}, \tag{A57}$$

whereas $\zeta^{n+1/2}_{i+1/2,j} = 0$ for $j=1$ and $j=J$.

$$P^{n+1/2}_{i+1/2,j} = \bar{P}^{n}_{i+1/2,j} - \frac{\Delta t^{n+1/2}}{2h} \times$$
$$\times \left\{ \frac{i}{i-\frac{1}{2}} u^{n}_{i+1,j}P^{n}_{i+1,j} - \frac{i-1}{i-\frac{1}{2}} u^{n}_{i,j}P^{n}_{i,j} + \begin{bmatrix} (\bar{w}\bar{P})^{n}_{i+1/2,j+1/2} - (\bar{w}\bar{P})^{n}_{i+1/2,j-1/2} \\ +2(\bar{w}\bar{P})^{n}_{i+1/2,3/2} \quad \text{if} \quad j=1 \\ -2(\bar{w}\bar{P})^{n}_{i+1/2,J-1/2} \quad \text{if} \quad j=J \end{bmatrix} + \right.$$
$$+ (\gamma-1)(\bar{P}^{n}_{i+1/2,j} + \bar{q}^{n}_{i+1/2,j}) \times$$
$$\left. \times \left(\frac{i}{i-\frac{1}{2}} u^{n}_{i+1,j} - \frac{i-1}{i-\frac{1}{2}} u^{n}_{i,j} + \begin{bmatrix} \bar{w}^{n}_{i+1/2,j+1/2} - \bar{w}^{n}_{i+1/2,j-1/2} \\ +2\bar{w}^{n}_{i+1/2,3/2} \quad \text{if} \quad j=1 \\ -2\bar{w}_{i+1/2,J-1/2} \quad \text{if} \quad j=J \end{bmatrix} \right) \right\} \tag{A58}$$

where we set $P^{n+1/2}_{i+1/2,j} = 0$ whenever the calculated value is less than *zero*.

The equations determining the $X^{n+1/2}_{i,j+1/2}$ are

$$\xi^{n+1/2}_{i,j+1/2} = \bar{\xi}^{n}_{i,j+1/2} - \frac{\Delta t^{n+1/2}}{2h} \times$$
$$\times \left\{ \frac{i-\frac{1}{2}}{i-1}(\bar{u}\bar{\xi})^{n}_{i+1/2,j+1/2} - \frac{i-\frac{3}{2}}{i-1}(\bar{u}\bar{\xi})^{n}_{i-1/2,j+1/2} + w^{n}_{i,j+1}\xi^{n}_{,j+1} - w^{n}_{i,j}\xi^{n}_{i,j} + \right.$$
$$+ (\bar{P}+\bar{q})^{n}_{i+1/2,j+1/2} - (\bar{P}+\bar{q})^{n}_{i-1/2,j+1/2} -$$
$$\left. - \bar{\varrho}^{n}_{i,j+1/2}(\bar{\Phi}^{n}_{i+1/2,j+1/2} - \bar{\Phi}^{n}_{i-1/2,j+1/2}) \right\}, \tag{A59}$$

where $1 \leqslant j \leqslant J-1$; while $\xi^{n+1/2}_{i,j+1/2} = 0$ for $i=1$ and $i=I$.

$$\zeta^{n+1/2}_{i,j+1/2} = \bar{\zeta}^{n}_{i,j+1/2} - \frac{\Delta t^{n+1/2}}{2h} \times$$
$$\times \left\{ \begin{bmatrix} \frac{i-\frac{1}{2}}{i-1}(\bar{u}\bar{\zeta})^{n}_{i+1/2,j+1/2} - \frac{i-\frac{3}{2}}{i-1}(\bar{u}\bar{\zeta})^{n}_{i-1/2,j+1/2} \\ +4(\bar{u}\bar{\zeta})^{n}_{3/2,j+1/2} \quad \text{if} \quad i=1 \\ -2\frac{I-\frac{3}{2}}{I-1}(\bar{u}\bar{\zeta})^{n}_{I-1/2,j+1/2} \quad \text{if} \quad i=I \end{bmatrix} + w^{n}_{i,j+1}\zeta^{n}_{i,j+1} - w^{n}_{i,j}\zeta^{n}_{i,j} + \right.$$
$$\left. + P^{n}_{i,j+1} + q^{n}_{i,j+1} - P^{n}_{i,j} - q^{n}_{i,j} - \bar{\varrho}^{n}_{i,j+1/2}(\Phi^{n}_{i,j+1} - \Phi^{n}_{i,j}) \right\}, \tag{A60}$$

$$P^{n+1/2}_{i,j+1/2} = \bar{P}^{n}_{i,j+1/2} - \frac{\Delta t^{n+1/2}}{2h} \times$$

$$\times \left\{ \left[\begin{array}{l} \dfrac{i-\frac{1}{2}}{i-1} (\bar{u}\bar{P})^{n}_{i+1/2,j+1/2} - \dfrac{i-\frac{3}{2}}{i-1} (\bar{u}\bar{P})_{i-1/2,j+1/2} \\ +4(\bar{u}\bar{P})^{n}_{3/2,j+1/2} \quad \text{if} \quad i=1 \\ -2\dfrac{I-\frac{3}{2}}{I-1} (\bar{u}\bar{P})^{n}_{I-1/2,j+1/2} \quad \text{if} \quad i=I \end{array} \right] + \right.$$

$$+ w^{n}_{i,j+1} P^{n}_{i,j+1} - w^{n}_{i,j} P^{n}_{i,j} + (\gamma-1)(\bar{P}^{n}_{i,j+1/2} + \bar{q}^{n}_{i,j+1/2}) \times$$

$$\left. \times \left(\left[\begin{array}{l} \dfrac{i-\frac{1}{2}}{i-1} \bar{u}^{n}_{i+1/2,j+1/2} - \dfrac{i-\frac{3}{2}}{i-1} \bar{u}^{n}_{i-1/2,j+1/2} \\ +4\bar{u}^{n}_{3/2,j+1/2} \quad \text{if} \quad i=1 \\ -2\dfrac{I-\frac{3}{2}}{I-1} \bar{u}^{n}_{I-1/2,j+1/2} \quad \text{if} \quad i=I \end{array} \right] + w^{n}_{i,j+1} - w^{n}_{i,j} \right) \right\}, \tag{A61}$$

where $P^{n+1/2}_{i,j+1/2} = 0$ whenever the value calculated by the above equation is less than *zero*.

The calculations of all secondary variables start from average quantities; and, the formulas for the several kinds of averages are set out below. In deriving these formulas the variables are assumed to vary linearly between successive netpoints. Moreover, along the r-direction averaging is of the form

$$\bar{x} = \int x(r)\, r\, dr \Big/ \int r\, dr,$$

Formulas for the averages are [cf. Equations (A44) and (A51)]:

$$\bar{x}_{i+1/2,j} = \tfrac{1}{2}(x_{i+1,j} + x_{i,j}) + \frac{x_{i+1,j} - x_{i,j}}{12i-6} \tag{A62}$$

$$\bar{x}_{i,j+1/2} = \tfrac{1}{2}(x_{i,j+1} + x_{i,j}) \tag{A63}$$

and

$$\bar{x}_{i+1/2,j+1/2} = \tfrac{1}{4}(x_{i,j} + x_{i+1,j} + x_{i+1,j+1} + x_{i,j+1}) + \\ + \frac{x_{i+1,j} + x_{i+1,j+1} - x_{i,j} - x_{i,j+1}}{24i-12}, \tag{A64}$$

5. Numerical Representation of the Gravitational Field

Calculation of the gravitational field is based on an integral formulation for the solution of Poisson's equation [cf. Equation (A6)]. This approach affords a straightforward treatment at moving boundaries as well as elsewhere. Moreover, it apparently results in smaller spurious fluctuations near moving boundaries than was found in attempts using difference analogues of the Poisson differential equation. The main difficulty with the current method lies in its considerable use of machine time.

According to the integral representation, the gravitational potential Φ at any primary netpoint is the sum of contributions from all parts of the physical space

where the density is non-zero. The source elements of the field are extensions of cells such as in Figure A1, generated by rotation around the z-axis. Hence, except for the innermost ones, which consist of small cylinders, the source elements are concentric rings having the thickness $\Delta r = \Delta z = h$. It is assumed, moreover, that inside any ring the density remains constant and can only vary discontinuously from ring to ring; this differs from the hydrodynamical equations, where linear variations are imagined to take place between successive netpoints.

When symmetry exists across the lateral plane at $z=0$, difference operations need only be applied to points in the first quadrant; but, the gravitational field must be the same as that arising from all four quadrants. The field is determined in this case by associating two rings with each netpoint i, j; the first contains the point itself and the other, located below $z=0$, contains the mirror image of the point. Throughout the first ring as well as its image the density is assumed to be $\varrho^n_{i,j}$; and, both rings are included in the summation determining the gravitational field [cf. Equation (A46)].

A numerical procedure for computing the gravitational potential Φ at an arbitrary netpoint i, j can be derived from an exact expression for the approximate model:

$$\Phi^n_{i,j} \equiv \Phi(r_i, z_j, t^n) = G \int^{V^n} \frac{\varrho(r, z, t^n)}{|\mathbf{r} - \mathbf{r}_{ij}|} \, dV(r, z) =$$

$$= G \sum_{\substack{l=1 \\ m=1}}^{I,J} \int_{r_{l-1/2}}^{r_{l+1/2}} \int_{z_{m-1/2}}^{z_{m+1/2}} \int_{\theta=0}^{2\pi} \frac{\varrho(r, z, t^n)\, r \, d\theta \, dz \, dr}{[r^2 + r_i^2 - 2rr_i \cos(\theta) + (z - z_j)^2]^{1/2}} \simeq$$

$$\simeq 4G \sum_{\substack{l=1 \\ m=1}}^{I,J} \varrho^n_{l,m} \int_{r_{l-1/2}}^{r_{l+1/2}} \int_{z_{m-1/2}}^{z_{m+1/2}} \frac{r \, dz \, dr}{[(r + r_i)^2 + (z - z_j)^2]^{1/2}} \times \tag{A65}$$

$$\times \int_0^{\pi/2} \frac{d\psi}{\left[1 - \dfrac{4rr_i}{(r + r_i)^2 + (z - z_j)^2} \sin^2 \psi\right]^{1/2}},$$

where the indices l, m identify the source point and the ring containing this point. Evidently, the expression consists of a time-dependent and time-independent part. The latter includes an integral over ψ which is the well-known complete elliptic integral of the first kind.

Comparing the above expression with Equation (A46) it is apparent that

$$g_{i,l,k} = 4G \int_{r_{l-1/2}}^{r_{l+1/2}} \int_{\zeta_{k-1/2}}^{\zeta_{k+1/2}} \frac{r \, d\zeta \, dr}{[(r + r_i)^2 + \zeta^2]^{1/2}} \int_0^{\pi/2} \frac{d\psi}{\left[1 - \dfrac{4rr_i}{(r + r_i)^2 + \zeta^2} \sin^2 \psi\right]^{1/2}}, \tag{A66}$$

where ζ has replaced $z - z_j$. When the source point l, m lies above the lateral symmetry plane at $z=0$, $\zeta = |z - z_j| = |m - j|h = (k-1)h$; while, for the mirror image below

$z=0$, $\zeta=z+z_j=(m-1+j-1)\cdot h=(k-1)\cdot h$. Hence, either $k=|m-j|+1$ or $k=m+j-1$, the index k being used to reduce the number of g coefficients.

Since the $g_{i,l,k}$ are time-independent, they can be calculated beforehand and stored for subsequent use. However, in practice the computing facilities must have considerable storage and rapid data-handling capabilities. As an example, the required number of g coefficients equals $I^2\cdot(2J-1)$, where I and J are the numbers of primary netpoints in the r- and z-directions respectively. Currently, $I=J=128$; hence, $I^2\cdot(2J-1)=4\,177\,920$ words.

The $g_{i,l,k}$ are calculated in one of four ways depending upon the relative locations of the source point l, m and the field point i, j. The various procedures are set out below.

The first way of calculating the g coefficients is employed if the field point lies on the z-axis, viz., $r_i=0$. In this case, Equation (A66) can be integrated exactly resulting in closed forms valid for all l and k.

Secondly, suppose the source element l, m is centered on the z-axis (viz., $r_l=0$) and the field point lies elsewhere. Then the $g_{i,l,k}$ are calculated by a series expansion in terms of even Legendre polynomials; i.e.,

$$g_{i>1,l=1,k}=2\pi G\left(\frac{h}{2}\right)^2\sum_{n=0}^{\infty}a_{2n}\left(\frac{h}{2s}\right)^{2n+1}P_{2n}(\mu), \tag{A67}$$

where $s=[r_i^2+(z_m-z_j)^2]^{1/2}=(r_i^2+\zeta_k^2)^{1/2}$ denotes the radius vector extending from the center of the source element to the field point i, j; and, $\mu=\zeta/s$ is the cosine of the angle subtended by the radius vector and the z-axis. The values worked out for the coefficients a_{2n} are as follows:

$a_0=1$	$a_{10}=+0.088\,955\,965$	
$a_2=+1/12$	$a_{12}=-0.316\,631\,61$	
$a_4=-7/40$	$a_{14}=-0.175\,077\,305$	
$a_6=-27/448$	$a_{16}=+0.669\,999\,07$	
$a_8=+0.186\,631\,94$	$a_{18}=+0.403\,499\,81$	etc.

The third method is applied when $r_i>0$ and the field point coincides with the center of the source element (viz., both $r_i=r_l$ and $z_j=z_m$). A series expansion has been set up for this case; i.e.,

$$\begin{aligned}g_{i,i,1}=\;&Gh^2\ln\left(\frac{r_i}{h}\right)\left[2-\frac{1}{24}\left(\frac{h}{r_i}\right)^2-0.001\,204\,426\left(\frac{h}{r_i}\right)^4-\right.\\&\left.-0.000\,059\,581\left(\frac{h}{r_i}\right)^6-0.000\,007\,284\,3\left(\frac{h}{r_i}\right)^8\ldots\right]+\\&+Gh^2\left[6.281\,233\,93-0.098\,610\,39\left(\frac{h}{r_i}\right)^2-0.001\,498\,36\left(\frac{h}{r_i}\right)^4-\right.\\&\left.-0.000\,056\,322\left(\frac{h}{r_i}\right)^6-0.000\,006\,537\,7\left(\frac{h}{r_i}\right)^8\ldots\right],\end{aligned} \tag{A68}$$

which is valid when $r_i\geqslant h$ (viz., $i\geqslant 2$).

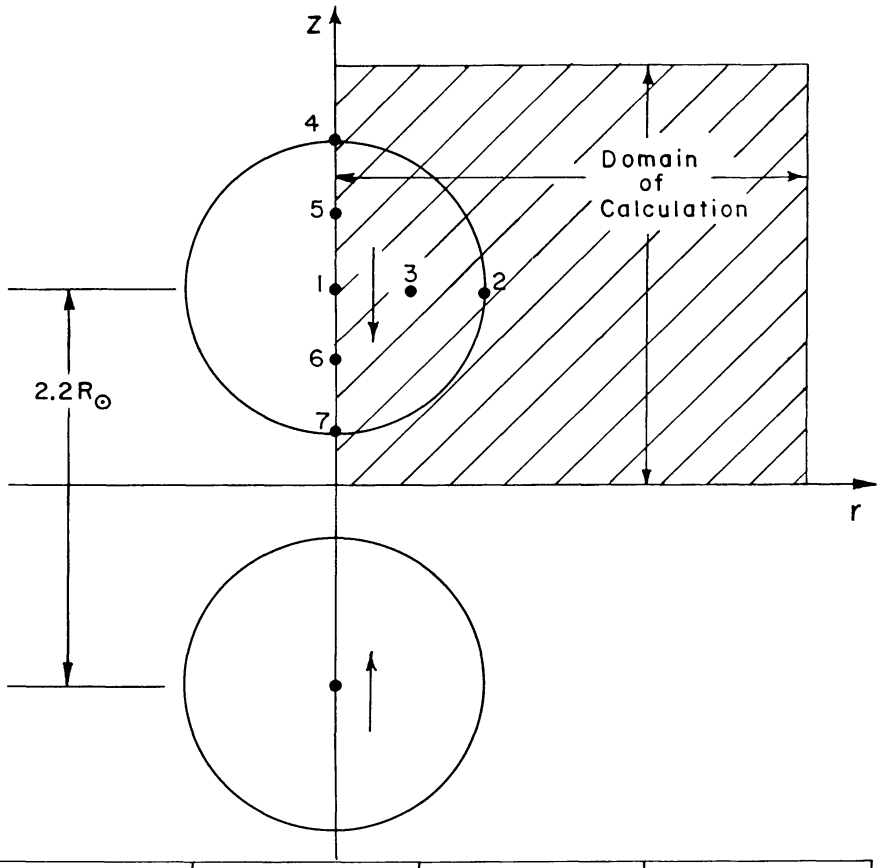

Point No.	Φ (numerical) 20 zones per $R_\odot$	Φ (numerical) 40 zones per $R_\odot$	Φ (numerical) 60 zones per $R_\odot$	Φ (exact)
1	5.70399	5.70299_5	5.70277	5.70259
2	1.66044_5	1.65628	1.65551	1.65490
3	2.83451	2.82774	2.82647	2.81316_5
4	1.54146	1.53761	1.53689	1.53632
5	2.74890	2.74236	2.74113_5	2.74016
6	3.00477	2.99759	2.99625	2.99517
7	2.15315	2.14777_5	2.14677	2.14597

Fig. A3. Numerical and exact calculations of the gravitational potential Φ for a configuration of two polytropes of index 3.0 separated by 2.2 $R_\odot$.

If none of the above conditions apply, the fourth way is used, which involves numerical integrations over the region $r_{l+1/2} \geqslant r \geqslant r_{l-1/2}$, $z_{m+1/2} \geqslant z \geqslant z_{m-1/2}$. The number of points per integration decreases with the increase in the separation of i, j and l, m; i.e., 49-point integration, 16-point integration, and 1-point integration. The weighting factors of the points are obtained by standard methods (e.g., Isaacson and Keller, 1966). In particular, Lagrange interpolation polynomials are used to determine the weighting factors in 49-point integrations.

The gravitational-field routine, as described above [Equations (A46), (A66), etc.], was checked as follows: For an *undistorted* polytrope the gravitational potential as well as the gravitational energy is given by exact equations (Chandrasekhar, 1939). In particular, the total gravitational potential Φ can be determined analytically at any point inside of or in the vicinity of two undistorted polytropes separated by $2.2\,R_\odot$ (the usual machine-zero configuration for stellar-collision calculations). Figures A2 and A3 show how well the numerically-determined values of Φ and the gradient of Φ approach the exact values as the mesh width h decreases. Furthermore, machine-zero values of the total gravitational energy have been found to agree with the exact values to within nearly 0.1% provided the mesh width is $h = R_\odot/40$ or less.

A second check of the gravitational-field routine was obtained by comparing two stellar-collision runs identical in every way except for the method of calculating Φ. The one run always employed the integral method based on Equation (A46). The other only made use of the integral method along an outer rectangular boundary and everywhere within this boundary resorted to a five-point difference analogue of Poisson's equation. From time to time the rectangular boundary was adjusted so that it always enclosed all regions of non-zero density. The difference analogue of Poisson's equation was solved by a standard line-iterative over-relaxation method. Although the numerical results were found to be highly consistent, the method which employed the integral exclusively was superior both from the standpoint of energy conservation and machine time. Regions near the moving fluid boundaries (not to be confused with the overall rectangular boundary) were subject to greater spurious fluctuations when the field was partly determined by the difference analogue of Poisson's equation; and, since the fluctuations involved peaks in fluid velocity, the difference program was automatically forced by the Courant condition [Equation (A70)] to go to smaller time steps Δt.

6. Controls Needed for Stability

In order to attain stability using the current program, it is necessary both to limit the size of the time steps Δt and add another form of artificial viscosity besides that first used by von Neumann and Richtmyer (1950). The latter is not sufficient, with our present difference equations, to prevent spurious fluctuations from building up at certain points along a moving boundary.

Effective additional smoothing is provided by terms introduced by Lapidus (1967) to approximate the artificial viscosity suggested by Lax and Wendroff (1960). In the

present instance, this means subtracting small damping terms from $A^{n+1/2}_{i+1/2,j}$ and $B^{n+1/2}_{i,j+1/2}$, the quantities used to form the difference analogue of the divergence [cf. Equations (A33) through (A39)]. Formulae demonstrating the procedure are set out below; the first expression holds when $1 \leqslant i \leqslant I-1$ and $1 \leqslant j \leqslant J$, the second and third for $1 \leqslant j \leqslant J-1$:

$$A^{n+1/2}_{i+1/2,j} = \text{undamped } A - \kappa_0 h r_{i+1/2} |u^n_{i+1,j} - u^n_{i,j}|(X^n_{i+1,j} - X^n_{i,j})$$

$$B^{n+1/2}_{1,j+1/2} = \text{undamped } B - \kappa_0 \frac{h^2}{8} |w^n_{1,j+1} - w^n_{1,j}|(X^n_{1,j+1} - X^n_{1,j}), \text{ for } i = 1 \qquad \text{(A69)}$$

$$B^{n+1/2}_{i,j+1/2} = \text{undamped } B - \kappa_0 h r_i |w^n_{i,j+1} - w^n_{i,j}|(X^n_{i,j+1} - X^n_{i,j}), \text{ if } i > 1 .$$

The constant κ_0 is fixed at some optimum value in the range $0.1 < \kappa_0 < 0.2$.

The necessary limitation of time steps is carried out by two controls. The first and most important is a form of the stability condition due to Courant *et al.* (1928). The second merely restricts Δt so that no decrease in density from cycle to cycle ever exceeds, say, 40%. A quantitative formulation of the first Δt control is

$$\Delta t = \mathfrak{f} h / \hat{s} , \qquad \text{(A70)}$$

where h denotes the mesh spacing, $\hat{s} = \{\max_{i,j}[(u^n_{i,j})^2 + (w^n_{i,j})^2 + P^n_{i,j}/\varrho^n_{i,j}]\}^{1/2}$, and $\mathfrak{f}$ is an empirically determined constant somewhat less than unity.

Equation (A70) ensures that the domain of dependence of the difference scheme shall include that of the basic differential equations, particularly as the difference steps Δx, Δt approach zero (cf., Courant *et al.*, 1928). In one respect this requirement is already satisfied; viz., the numerical method for calculating the gravitational field depends upon the values of density ϱ at all netpoints within the domain of calculation. However, the treatment of the hydrodynamic variables (i.e., ϱ, ϱu, ϱw, and P) remains to be examined. Consider small portions of the domains of dependence for both difference and differential systems starting from an arbitrary point x, t^{n+1} and going back a small interval to time t^n. For the difference scheme, the values at x, t^{n+1} depend upon values at netpoints included in the range approximately $(x+\Delta x, x^n) \gtrsim$ $\gtrsim (x, t^n) \gtrsim (x-\Delta x, t^n)$, where $t^n = t^{n+1} - \Delta t^{n+1/2}$. Similarly, going back another time step to t^{n-1}, the values at $x+\Delta x, t^n$; x, t^n; and $x-\Delta x, t^n$ depend upon netpoints lying approximately in the region $(x+2\Delta x, t^{n-1}) \gtrsim (x, t^{n-1}) \gtrsim (x-2\Delta x, t^{n-1})$, etc. Thus, in the difference scheme the domain of dependence for the point x, t^{n+1} seems to be contained within a conoid drawn downward from x, t^{n+1} in $x-t$ space, where x may represent more than one space dimension (e.g., r and z). An analogous concept should exist for the domain of dependence of the differential system. Anyway, at the slightly earlier time t^n the domain of dependence for the point x, t^{n+1} in the differential system cannot extend over an appreciably greater range of x than $x \pm \Delta t^{n+1/2}[(u^2+w^2)^{1/2}+c]$, u and w being the components of fluid velocity and c the sonic velocity (e.g., in an ideal gas $c^2 = \gamma P/\varrho$). This view implies that the system is essentially hyperbolic and that variations are propagated at a maximum speed of $(u^2+w^2)^{1/2}+c$. Hence,

the local domain of dependence of the difference scheme is expected to be sufficiently large if

$$\Delta x > \Delta t[(u^2 + w^2)^{1/2} + c]. \tag{A71}$$

Courant *et al.* (1928), Lax and Wendroff (1964), Isaacson and Keller (1966, p. 485), as well as others have discussed this idea more carefully.

Before describing the results of an empirical determination of the constant f appearing in Equation (A70), consider an approximate analytic treatment which examines the stability of difference solutions against short-wavelength fluctuations in regions where point-to-point changes are relatively small. Excluded are the troublesome boundary regions largely controlled by the artificial damping terms of Equations (A69) etc. The treatment involves the first variation of the difference scheme expressed as a system of linear equations for the variations [i.e., $\delta\varrho$, δP, $\delta(\varrho u)$, and $\delta(\varrho w)$] of variables defined at primary netpoints. All variations at secondary netpoints and that of the gravitational potential are eliminated by means of their determining equations [viz., Equations (A56) through (A61) and (A46)]. The variations or fluctuations, when they appear, seem to be unwanted parts of solutions of the difference equations themselves.

Imagine that, in the small, the fluctuations are linearly related by the system of first-variational equations and that an arbitrary fluctuation is expandable in a Fourier series (von Neumann and Richtmyer, 1950; Richtmyer and Morton, 1967); e.g.,

$$\delta X = \xi_{\alpha,\beta}^{n-n_0}\,\delta X_0 \exp\{i[\alpha(r - r_0) + \beta(z - z_0)]\}. \tag{A72}$$

Time dependence enters by means of the factor $\xi_{\alpha,\beta}$, and the component α, β will not build up if

$$|\xi_{\alpha,\beta}| \leqslant 1 + O(\Delta t). \tag{A73}$$

This is the so-called von Neumann condition, which we take as a measure of stability. Moreover, since on the linear view no wavelength smaller than the net spacings can be represented by the difference scheme, no oscillation or fluctuation determined by the difference equations can include a component of wavelength λ less than twice the smallest net spacing; i.e., $\lambda \geqslant \lambda(\min) = 2h$ or $\alpha(\max) = \beta(\max) = 2\pi/\lambda(\min) = \pi/h$. It is, in fact, just the $\lambda(\min)$ component which is found to dominate most numerical instabilities.

To simplify the algebra, suppose that (1) the flow-bias is set to zero, (2) all artificial damping terms are very small, (3) the cylindrical curvature effects can be neglected, and (4) only the $\lambda(\min)$ components are appreciable. The last supposition implies that the variations obey relations like

$$\delta\varrho_{i+1,j}^{n+1} = \xi e^{i\pi(r_{i+1} - r_i)/h}\delta\varrho_{i,j}^{n} = \xi e^{i\pi}\delta\varrho_{i,j}^{n}. \tag{A74}$$

Furthermore, in the case of the gravitational potential [cf., Equations (A45), (A46)]

$$\delta\Phi_{i,j}^{n} = g_{i,i,j,j}\delta\varrho_{i,j}^{n} + \sum_{\substack{l,m \\ l\neq i,\, m\neq j}} g_{i,l,j,m}\delta\varrho_{l,m}^{n} \approx g_{i,i,j,j}\delta\varrho_{i,j}^{n}. \tag{A75}$$

Using the above approximations the equations of first variation become

$$\begin{aligned}
&[\xi - 1 - 2\lambda^2(u^2 + w^2 + 2\varrho g)]\,\delta\varrho + 4\lambda^2\delta P + 4\lambda^2 u\,\delta(\varrho u) + 4\lambda^2 w\,\delta(\varrho w) \simeq 0\\
&-4\lambda^2 c^2(u^2 + w^2 + \varrho g)\,\delta\varrho + [\xi - 1 + 2\lambda^2(u^2 + w^2 + 2c^2)]\,\delta P +\\
&\qquad + 6\lambda^2 c^2 u\,\delta(\varrho u) + 6\lambda^2 c^2 w\,\delta(\varrho w) \simeq 0\\
&-2\lambda^2 u(2u^2 + 2w^2 + c^2 + 3\varrho g)\,\delta\varrho + 8\lambda^2 u\,\delta P +\\
&\qquad + [\xi - 1 + 2\lambda^2(4u^2 + w^2 + c^2)]\,\delta(\varrho u) + 6\lambda^2 wu\,\delta(\varrho w) \simeq 0\\
&-2\lambda^2 w(2u^2 + 2w^2 + c^2 + 3\varrho g)\,\delta\varrho + 8\lambda^2 w\,\delta P +\\
&\qquad + 6\lambda^2 uw\,\delta(\varrho u) + [\xi - 1 + 2\lambda^2(u^2 + 4w^2 + c^2)]\,\delta(\varrho w) \simeq 0
\end{aligned} \tag{A76}$$

where, $\lambda = \Delta t/h$ and $c^2 = \gamma P/\varrho$. A non-trivial solution of these equations requires that the determinant of the coefficients shall vanish; this in turn determines the allowed values of ξ, viz., the eigenvalues. The object is to find the condition on $\lambda = \Delta t/h$ such that the eigenvalues obey Equation (A73).

A first eigenvalue can be separated out easily, leaving a cubic equation whose three roots yield the remaining eigenvalues. Thus

$$\xi_1 = 1 - 2\lambda^2(u^2 + w^2 + c^2), \tag{A77}$$

where $\lambda = \Delta t/h$; whereas, for $i = 2, 3, 4$,

$$\begin{aligned}
&(\xi_i - 1)^3 + (\xi_i - 1)^2\, 2\lambda^2[4(u^2 + w^2) + 3c^2 - 2\varrho g] +\\
&\qquad + (\xi_i - 1)(2\lambda^2)^2[3(u^2 + w^2)^2 + 2c^4 - 4(u^2 + w^2)\varrho g - 2c^2\varrho g] +\\
&\qquad + (2\lambda^2)^3(u^2 + w^2)^2(c^2 - 2\varrho g) = 0\,.
\end{aligned} \tag{A78}$$

Considerable simplification is obtained if, as is usually true in practice,

$$\varrho g \ll c^2\,. \tag{A79}$$

Then, with the aid of some numerical work it is found that

$$|\xi_i| < 1\,; \quad i = 1, 2, 3, 4\,; \quad \text{if} \quad \Delta t \leqslant \frac{h}{[4(u^2 + w^2) + 3c^2]^{1/2}}, \tag{A80}$$

where $c^2 = \gamma P/\varrho$. This result may be compared with Equation (A70).

If using Equations (A76) or (A78) one considers the special cases (1) $u^2 + w^2 \to 0$ and (2) $u^2 + w^2 \gg c^2 > \varrho g$, it turns out that

$$\begin{aligned}
&(1) \qquad \text{when } u^2 + w^2 \to 0\,, \quad \Delta t \leqslant \frac{h}{[2(c^2 - \varrho g)]^{1/2}};\\
&(2) \qquad \text{when } u^2 + w^2 \gg c^2 > \varrho g\,, \quad \Delta t \leqslant \frac{h}{[3(u^2 + w^2)]^{1/2}}\,.
\end{aligned} \tag{A81}$$

The above relations suggest that the inequality in (A80) may be a bit too severe. However, a study of regions where $u^2 + w^2 \approx c^2$ indicates that (A80) cannot be relaxed if the whole range of $(u^2 + w^2)/c^2$ is to be included. It is interesting to compare these results with what is found in practice.

Numerical stability becomes evident mainly in two ways: (1) the mass and total energy summed over all netpoints remain nearly constant over many thousands of time steps; and, (2) whenever large spurious peaks occur, say in fluid velocity, they are subsequently damped out. In the case of stellar collision calculations, stability is found to be maintained if

$$\Delta t \leqslant 0.7\, h/\hat{s}\,, \tag{A82}$$

which is close to $\Delta t \leqslant (1/\sqrt{2})\cdot h/\hat{s}$. The critical value of the Courant factor $\tilde{\mathfrak{f}}$ is dependent, at least to some extent, upon the level of artificial damping; but, the relationship in our case has not been worked out at this time, except to note that stability throughout a collision calculation apparently cannot be preserved without the use of some artificial viscosity.

When stability is marginal, certain characteristic effects appear; e.g., using a Courant factor just below or slightly greater than the critical value $\tilde{\mathfrak{f}}=0.7$, stellar-collision calculations acquire large spurious peaks in fluid velocity which are most intense immediately following maximum impact, and at times rise above the average levels by factors of 100 or 1000. These peaks almost always occur along the trailing edges of moving boundaries in regions of very low densities and at netpoints located on or near the axis of symmetry (viz., $r=0$). If a calculation is stable, the peaks are subsequently damped out by the artificial dissipation. When $\tilde{\mathfrak{f}}>0.7$, the peaks appear more often, are of greater height, and continue to occur until divergence is triggered. The time lapse before blowup decreases somewhat as $\tilde{\mathfrak{f}}$ is increased above its critical value. However, this interval does not rapidly approach zero as $\tilde{\mathfrak{f}}\to 1.0$ from below because, acting through the Courant condition [Equation (A70)], the large spurious velocity peaks always tend to reduce the time steps Δt. A related effect due to the Courant condition appears on comparing runs identical except for $\tilde{\mathfrak{f}}=0.7$ and $\tilde{\mathfrak{f}}=0.5$. Having larger time steps initially, the run with greater $\tilde{\mathfrak{f}}$ allowed the first spurious velocity peaks to rise higher, thus a marked reduction in Δt ensued which in turn favored the suppression of these peaks. Thereupon, Δt again increased to be followed almost immediately by larger spurious fluctuations with another reduction of Δt, etc. The overall result was a run with $\tilde{\mathfrak{f}}=0.7$ and highly erratic values of Δt. On the other hand, for $\tilde{\mathfrak{f}}=0.5$ the time steps were more uniform, larger on the average, and resulted in faster smoother execution.

7. Evidence for Convergence of the Difference Scheme

The convergence of solutions obtained by the present difference scheme was tested for the case of uniform translation of an isolated polytropic density distribution. Such a distribution, of course, is one of a family of possible configurations in which self-gravitation is balanced by hydrostatic pressure (Chandrasekhar, 1939). Given an initial uniform velocity and otherwise left alone, the density configuration should remain unchanged as it moves continuously across the network at the prescribed

velocity. Any departures from uniform motion or from the initial density distribution are attributable to computational errors.

The density distribution investigated was that of a polytrope of index 3.0 and of solar mass and radius – the same model as used in the current stellar-collision studies. The initial velocities prescribed for the various runs were 213.0 km s^{-1}, 294.3 km s^{-1}, 580.2 km s^{-1}, and 1042.4 km s^{-1}. Calculations were made with difference zoning of 20 steps per $R_\odot$ and 40 steps per $R_\odot$; the former allowed a greater movement within the domain of calculation (cf. Figure A5). Typical numerical results are shown in Figures A4 and A5, where initial and final density distributions are shown for a polytrope moving towards the left at 580.2 km s^{-1}.

The numerical transport of the center of mass was handled very nearly correctly. The most extreme case was a displacement across a distance of about 4.7 $R_\odot$ (cf. Figure A5), involving 4140 time steps, which was calculated correctly to within 0.5%. In addition, total mass was conserved within *one* part in 200. However, conservation of total energy was less precise, there being a slow continual *increase* in the case of

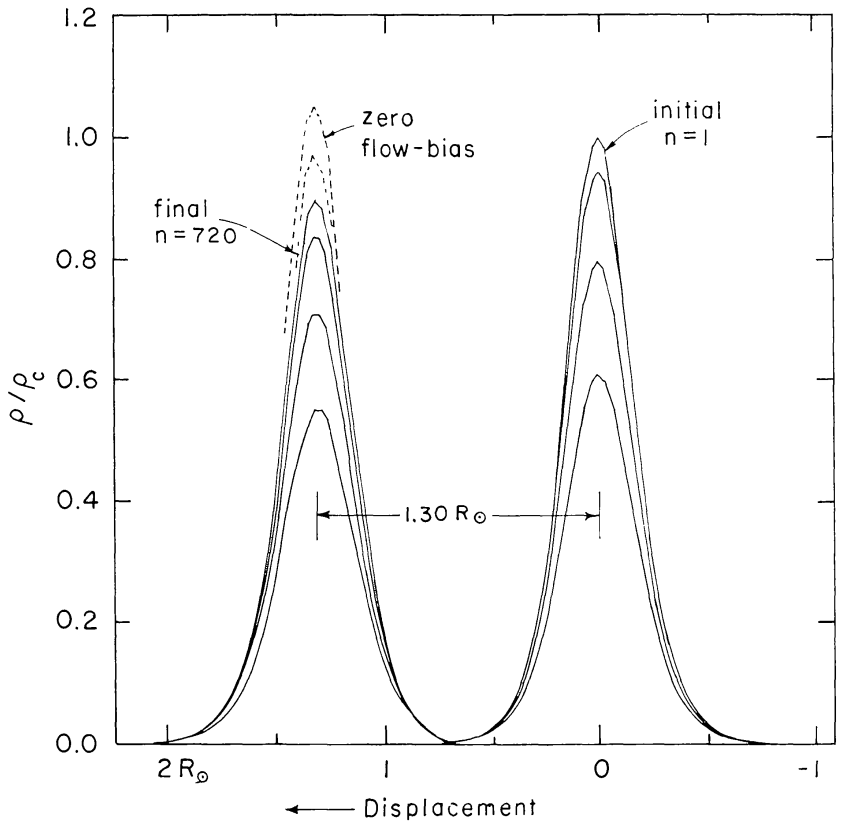

Fig. A4. An example of the numerical translation of a stellar density distribution (viz., polytrope of index 3.0, zoned into 40 steps per $R_\odot$, and moving at 580.2 km s^{-1}). The final center lies at $j = 36.2$ compared to the correct value of $j = 36.00$. Calculated total mass remained constant to better than one part in 200. Some spurious gain in total energy occurred, ultimately amounting to 2.2% of the gravitational binding energy. The dashed outline above the final peak denotes the result when flow-bias was set to zero; in this case, change in total energy was negligible.

580.2 km s^{-1}: (1) When the mesh width h was $R_\odot/40$ and after 720 time steps or 26.0 min of motion in real time, the spurious cumulative energy increase had reached 2.2% of the gravitational binding energy (Figure A4). (2) Using $h=R_\odot/20$, after 4140 time steps or 93.1 min of real-time motion across a distance of 4.66 $R_\odot$ (Figure A5), the spurious increase in total energy amounted to 7.7% of the gravitational binding energy. Perhaps the most serious aberration was a continual degradation

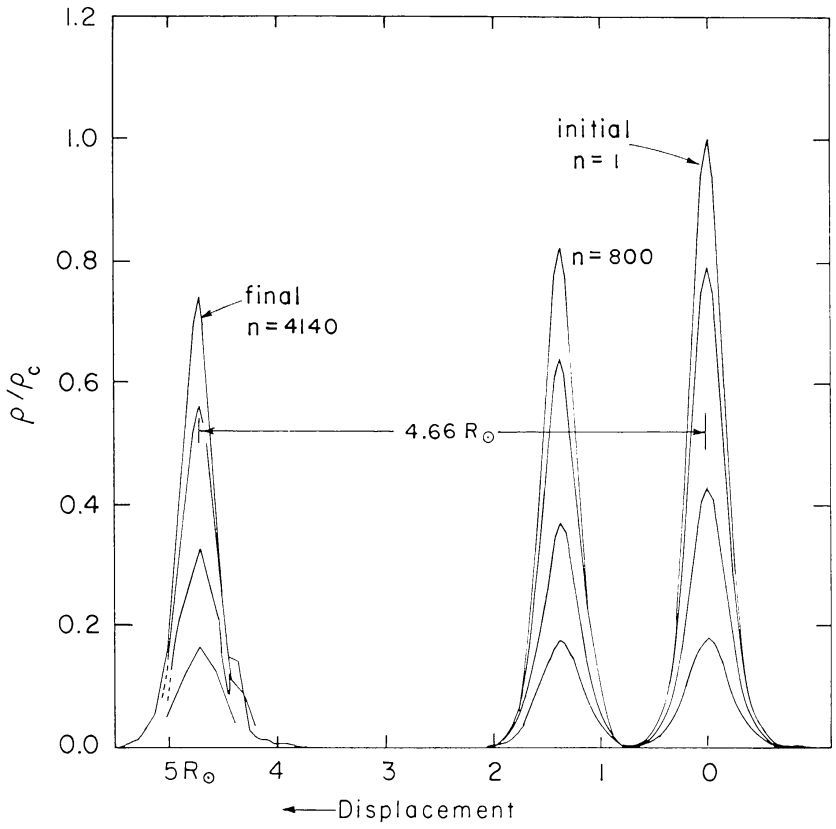

Fig. A5. Numerical translation of a coarse-zoned stellar density distribution (viz., polytrope of index 3.0, zoned into 20 steps per $R_\odot$, velocity 580.2 km s^{-1}). The calculated final center lies at $j=14.9$ compared to the correct value of 14.82. No appreciable degradation in total mass was observed; but, during the calculation the total energy suffered a cumulative spurious gain equal to 7.7% of the gravitational binding energy.

of the density distribution, the most obvious effect being a fall-off in peak height (Figure A5). As may be seen from Figures A4 and A5, the degree of degradation might be tolerable for a displacement of $\sim R_\odot$, which in almost all our collision calculations was the distance that the centers of the colliding polytropes had to travel from their machine-zero positions to where their centers merged at the center of impact. Evidence that this initial degradation did not appreciably affect our calculated results is obtained by comparing certain collision runs with an earlier calculation in which the machine-zero separation was 4.2 $R_\odot$ instead of the usual 2.2 $R_\odot$ (cf. Table I).

TABLE AI

Calculated quantities with and without flow-bias, case of a uniformly moving polytrope (40 netpoints per $R_\odot$)

Flow-bias factor	Machine time	Cycle number n	Displacement of center	Total energy summed over active region	Gravitational potential at center of star
1.20	0	1	0	0.024[a]	5.170489[b]
1.20	0.904	720	1.30 $R_\odot$	0.030	4.938946
zero	0	1	0	0.024[a]	5.170489[b]
zero	0.920	1560	1.32 $R_\odot$	0.024	5.177887

[a] In these units gravitational binding energy of a polytrope of index 3.0 is 0.271477.
[b] Exact value is 5.170528.

When the flow-bias was set to zero, both the spurious energy increase and the fall-off in peak height largely disappeared (Figure A4). As illustrated in Table AI, it is interesting to note how well the properties of the stellar model as a whole were preserved in this instance. In collision calculations, however, we currently find that flow-bias is necessary to maintain numerical stability during the intensely violent periods when compression and velocity reversal are maximum as well as to conserve energy in the large (cf. Tables AIV and AV), the more usual artificial viscosity terms not being enough in themselves. Referring again to Table AI and the case of zero flow-bias, the high cycle number n needed to reach a certain point in time is an indication of insufficient damping; i.e., the larger spurious velocity fluctuations, acting through the Courant condition [Equation (A70)], bring about a reduction in Δt and a corresponding increase in n.

In conclusion, there is evidence from these test calculations that our difference scheme yields solutions which converge to correct solutions. But, our method of damping or suppressing spurious fluctuations, particularly at moving boundaries, might be improved.

8. Nature of Errors in Collision Calculations

The primary objective of the present program was to calculate the mass that would escape from the compound system formed in a head-on collision between two solar-like stars. The escaping mass, termed *volatile mass*, was determined by summing the mass elements about netpoints i, j wherever local internal energy plus outgoing kinetic energy exceeded gravitational binding energy: i.e.,

$$M_v^n = 2\pi \sum_{i,j} \varrho_{i,j}^n \Delta V_{i,j}, \tag{A83}$$

in which M_v^n denotes the numerically calculated value of volatile mass at time t^n, $\varrho_{i,j}^n$ the numerically determined values of density, and the $\Delta V_{i,j}$ are fixed volume elements [the $\Delta V_{i,j}$ here equal the '$\Delta V_{i,j}/\Delta\theta$' of Equation (A27) except for $j=1$,

where $\Delta V_{i,j=1} = \frac{1}{2}\,'\Delta V_{i,j=1}/\Delta\theta'$]. Moreover, if the program handles only one quadrant of space, the summation formula must be adjusted to yield results correspondent with the entire space. In contrast to volatile mass, which is a partial sum, total mass M^n is the sum over all elements, viz.,

$$M^n = 2\pi \sum_{i=1,j=1}^{I,J} \varrho_{i,j}^n \Delta V_{i,j}\,. \tag{A84}$$

In this section the errors in volatile-mass calculations are examined in the following order: (A) machine round-off errors; (B) errors due to the low-level density cutoff; (C) effects of artificial dissipation; and (D) discretization errors. The discussion on discretization errors is largely concerned with justifying the position that

$$M_v^n = M_v(t^n) + a(t^n)\, h^2 + O(h^4), \tag{A85}$$

where $M_v(t^n)$ denotes the correct value of volatile mass for the system under investigation and $a(t^n)\, h^2 + O(h^4)$ the discretization error. By writing the coefficient of h^2 as $a(t^n)$ we mean to imply that it is sensibly independent of both the mesh width h and the time steps Δt, a property which allows both an estimation of our discretization error and the use of Richardson's method for extrapolation to zero mesh width (cf. Isaacson and Keller, 1966; Forsythe and Wasow, 1960; etc.).

(A) *Round-off Errors* are mainly determined by the nature of the computing machine but can be reduced to some extent by careful programming. In our case, use was made of double precision, except for the coefficients $g_{i,l,k}$ [cf. Equations (A46) and (A66)]. Since new round-off errors are introduced at each time step, the cumulative effect should increase with the number of time steps n, perhaps like $\sqrt{n}$. Tests of such an effect are available. All our significant calculations have been run through several times, many runs being identical except for average time step $\bar{\Delta}t$ and a simultaneous adjustment of the flow-bias factor ε_0 so as to maintain good energy conservation (cf. Table I). However, as exemplified by Table AII, no dependence on n has been detected. Because of simultaneous adjustments in flow-bias along with the changes in $\overline{\Delta t}$, it is well to note other evidence that round-off effects must be negligible; viz., the high accuracy with which total mass is preserved in the course of any calculation, particularly that of Figure A5 where a mass distribution was moved numerically over many times its own diameter. Initially the total mass in Figure A5 was 0.155 machine units; much later at $n = 3400$ and after a displacement of almost 4 times the initial radius, the total mass was still 0.155; while, after $n = 4140$, the total mass had dropped to 0.154, a fall-off readily attributable to the effects of a density cutoff. At the same time, the overall motion of the center of mass was calculated correctly to within a lag of 0.5%. In view of these tests, it is believe that round-off errors are negligible.

(B) *Errors due to the low-level density cutoff* must certainly be present as indicated by effects on the leveling-off value of volatile mass (Figure 12). In the case of the lowest-velocity collision calculations, a direct measure of such errors has been ob-

TABLE AII

Calculations of the low-velocity collision for various space and time steps (variables expressed in machine units)

h[b]	f[c]	Max density at center of impact			Max total internal energy			Early volatile mass[a]			Volatile mass		
		ϱ_c	Time	n	E	Time	n	M_v^n	Time	n	M_v^∞	Time	n
$R_\odot/20$	0.2	3.07[e]	1.10	700	0.364	1.13	720[d]	0.00120	1.33	850	0.00530	2.16	1260
$R_\odot/20$	0.5	3.06[e]	1.08	110	0.362	1.15	120				0.00528	2.06	400
$R_\odot/40$	0.25	3.43[e]	1.07	480	0.405	1.10	500	0.00388	1.33	700	0.00700	2.02	1720
		3.56[f]											
$R_\odot/60$	0.2	3.65[e]	1.09	700	0.428	1.11	720	0.00506	1.33	1120			
		3.93[f]											
		3.92[g]											

[a] Prior to leveling-off so as to include $R_\odot/60$ run which was only partially completed.
[b] $\Delta r = \Delta z = h$.
[c] $\Delta t = \mathfrak{f} h/\hat{s}$, cf. Equation (A99).
[d] Relatively large n (viz., number of cycles) due to reduction of Δt in order to satisfy the condition $\varrho_{i,j}^{n+1} \geqslant 0.6\, \varrho_{i,j}^{n}$.
[e] Value at $i=1, j=1$.
[f] at $i=1, j=2$.
[g] at $i=1, j=3$. Dip in ϱ at exact center is interpreted as due to locally increased temperature.

tained by comparing runs using the mesh width $h=R_\odot/20$ and differing only in density cutoff, either $\varrho_c \times 10^{-6}$ or $\varrho_c \times 10^{-7}$. For runs with $\varrho_c \times 10^{-7}$ the leveling-off value of volatile mass was found to be 1.07 times larger than for runs having $\varrho_c \times 10^{-6}$. In practice, when the cutoff was $\varrho_c \times 10^{-7}$, greater spurious fluctuations occurred in the very low-density regions near the fluid boundaries and caused the time steps Δt to be reduced [cf. Equation (A70)] thereby greatly increasing the machine running time. Similar runs with different density cutoffs were not made for the higher-velocity collisions. However, since total mass was always conserved to better than *one* percent, the cutoff mass loss could not have exceeded this value. In fact, *one* percent of the total mass must be too large for several reasons: (1) In most instances at the time that the calculated value of volatile mass had just leveled off, the total mass loss was found to be only about 0.6%. (2) The overall mass loss did not show any appreciable change with initial collision velocity. (3) Early in a calculation, the possibility existed of mass losses occurring elsewhere than from the volatile regions. Thus, we were led to assume for the higher-velocity collisions that, as a result of the density cutoff, the most likely error in the volatile-mass calculations is a loss approximately equal to 0.5% of the initial total mass or, in other words, equal to 10% of the value of volatile mass for the case where the initial collision velocity was *zero* at infinite separation. By comparison, a lower limit of 7% was actually found for the cutoff mass loss in the zero initial-velocity case (see above). Finally, in view of the lack of appreciable change in total mass loss with mesh width h, the density-cutoff errors were assumed to be independent of h.

(C) *Effects of artificial dissipation* – The artificial dissipation increases enormously at points of spurious fluctuations and also about shock fronts as well as at any point of rapid compression; elsewhere, it stays very small. Stated another way, the artificial dissipation may be either highly fluctuating in counteraction to the spurious fluctuations or largely reproducible from run to run. Included in the term 'artificial dissipation' are the following three forms: (1) the artificial viscosity of Equations (A42) and (A53), (2) the artificial viscosity defined by Equations (A69), and (3) the flow-bias as given by Equations (A35) and (A39).

Spurious fluctuations, in the case of stellar-collision calculations, are found most often between certain netpoints, along a free-moving fluid boundary where the density is extremely low. These fluctuations recur identically only for runs that are the same in every way; otherwise, they vary apparently at random from run to run, even between runs differing merely in the average size of Δt. Use has been made of this dependence on Δt to show that the fluctuating components of artificial dissipation have little effect on our results. Incidentally, sometimes in coarser-zoned calculations spurious fluctuations appeared at the center of impact, but only late in the calculations when the fluid velocities in these regions were relatively low and, hence, the resulting flow-bias and fluctuating artificial viscosity terms also small.

The fact that fluctuating components of artificial dissipation did not appreciably effect our numerical results is shown by the lack of dependence of these results on the average size of Δt or, in other words, on the number of time steps n used to reach any well-recognized point in the course of a collision calculation (cf. Table AII). This conclusion is substantiated by the fact that the calculated values of total mass [Equation (A84)] do not depend upon n, even in cases where the flow-bias was set to zero thereby allowing exceptionally large spurious fluctuations to occur along the trailing fluid boundary.

In contrast to regions of spurious fluctuations, values of artificial dissipation surrounding shocks and places of rapid compression such as the center of impact are largely reproducible from run to run. At least in the case of *artificial viscosity* [Equations (A42), (A53), (A69)], any errors which these effects contributed must be of $O(h^2)$ as the defining equations for artificial viscosity imply. The effects of flow-bias, which are somewhat less obvious, are considered below.

The radial component of the flow-bias term may be written as follows [cf. Equations (A33), (A34), and (A35)]:

$$\varepsilon^n_{x,j}\left[(\varrho u)^{n+1/2}_{i+1/2,j} - (\varrho u)^n_{x,j}\right] = h\,\frac{\varepsilon_0}{2}\,\chi^n_{x,j}\,(1-\chi^n_{x,j})\,\frac{r_x}{r_{i+1/2}}\,\frac{(\varrho u)^{n+1/2}_{i+1/2,j} - (\varrho u)^n_{x,j}}{\frac{1}{2}\left(h - |u_{x,j}|\,\Delta t^{n+1/2}\right)} \tag{A86}$$

where ϱ has been substituted for the generalized variable X and

$$\chi^n_{x,j} = \frac{|u^n_{x,j}|\,\Delta t^{n+1/2}}{h} = \tilde{\mathfrak{f}}\,\frac{|u^n_{x,j}|}{(\hat{s})^n} \tag{A87}$$

The symbol u denotes the r component of fluid velocity; and, except for small effects of displacement in the z direction, the quantity $\frac{1}{2}(h-|u^n_{i,j}|\Delta t^{n+1/2})$ is the separation

at time $t^{n+1/2}$ between the fluid particle located at $r_{i+1/2}, z_j, t^{n+1/2}$ and the particle which a very short time earlier was at r_x, z_j, t^n, x being either i or $i+1$ depending upon the direction of fluid flow. The right-hand side of Equation (A86) has the form

$$\text{flow-bias} \sim h \frac{\varepsilon_0}{2} \chi (1-\chi) \frac{u}{|u|} \frac{\partial (\varrho u)}{\partial r}, \tag{A88}$$

where

$$0 \leqslant \chi^n_{x,j} (1 - \chi^n_{x,j}) \leqslant \tfrac{1}{4} \tag{A89}$$

and it is assumed that $r_x/r_{i+1/2} \simeq 1$. Moreover, due to Equation (A70) an upper bound may be placed on the flow-bias terms; e.g., in the case of the difference equation for advancing ϱ

$$|\text{flow-bias}| < 2\varepsilon_0 \mathfrak{f} |\varrho u|. \tag{A90}$$

Similar relations hold for the z component of fluid velocity, w.

To assess the level of flow-bias, values of $\varepsilon_0 \Delta t/2h$ have been examined for all physically significant runs, and typical results are displayed in Table AIII. The values of h, ε_0, and $\mathfrak{f}$ were prescribed in advance for any run; while Δt was determined

TABLE AIII

Factor, $\varepsilon_0 \Delta t/2h$, which when multiplied by fluid velocity indicates the level of flow-bias

Initial relative velocity at infinity	Mesh width h	Flow-bias factor ε_0	Courant factor $\mathfrak{f}$	Cycle number n	Time in machine units	$\frac{\varepsilon_0 \Delta t}{2h}$ mach. units
zero	$R_\odot/20$	1.0	0.2	2	0.0040	0.0404
				520	0.838	0.0085
				540	0.865	0.0140
				640	1.03	0.0099
				660	1.06	0.0114
				720	1.13	0.0139
				1200	2.03	0.0208
zero	$R_\odot/20$	0.2	0.5	2	0.0040	0.0081
				80	0.890	0.0224
				100	1.03	0.0142
				110	1.08	0.0049
				120	1.15	0.0111
				380	2.03	0.0027
zero	$R_\odot/40$	1.0	0.25	2	0.0040	0.0808
				320	0.840	0.0139
				340	0.871	0.0280
				480	1.07	0.0492
				500	1.10	0.0244
				1740	2.03	0.0142
zero	$R_\odot/60$	1.0	0.2	3	0.0040	0.0807
				520	0.845	0.0432
				700	1.09	0.0378
				720	1.11	0.0366

automatically at each time step according to Equation (A70). As apparent from Table AIII, the values of $\varepsilon_0 \Delta t/2h$ occurring in practice were such that the flow-bias was always a small perturbation of the calculated change per time step [cf. Equation (A33) with (A35), and Equations (A36) and (A37) with (A39)] unless, of course, either $|u|$ or $|w|$ was much greater than unity.

The survey of our stellar-collision calculations shows that, for the most part, regions subject to sizable flow-bias effects had low densities (viz., $\varrho < \varrho_c \times 10^{-2}$, ϱ_c denoting the central density of a solar-like stellar model), and that relative to adjacent terms the greatest values of flow-bias occurred at points on the outer fluid surfaces where $\varrho \sim \varrho$ (cutoff) $\leqslant \varrho_c \times 10^{-6}$. The only significant exceptions were two surface-like regions of deceleration located either side of and close to the lateral plane of symmetry, which passes through the center of impact. These surfaces contained the set of all points where the gradient of fluid velocity underwent a sharp reversal from steady acceleration towards the center of impact to a rapid deceleration. The surfaces of deceleration persisted throughout early phases of the collision process and continued past the point of maximum compression, until the recoil shock fronts had swept by leaving all fluid elements moving outwards, with the possible exception of elements near the center of the residual core.

The process that took place along the deceleration surfaces was highly reproducible from run to run regardless of h, and involved a component of flow-bias error which may have affected the calculated values of volatile mass through the domain of dependence of the hydrodynamic variables. However, it is believed that this source of error was at worst no greater than of $O(h^2)$ for the following reason: Equation (A86) shows the flow-bias terms to be of $O(h)$; but, in the difference scheme such terms are paired together so as to contribute errors of order $O(h^2)$ at each time step [cf. Equation (A96)]. This contrasts with the artificial viscosity or better still the discretization errors which stepwise per pair contribute errors of $O(h^3)$. The magnitudes of the flow-bias terms, on the other hand, are more strongly bounded than those of artificial viscosity, and are found to be sizable in calculations of concern only along a small number of surfaces, like the surfaces of deceleration. Because flow-bias is only sizable along a few surfaces, the number of netpoints thus involved is of $O(R)$, viz., proportional to a surface of revolution defined by a curve of length $O(R)$ in r-z space, whereas discretization errors are present at all active netpoints, the number of these being of $O(R^2)$. Consequently, in mass summations and also in the cumulative effects which may have arisen by way of the domain of dependence, the number of points contributing discretization errors was greater than the number contributing appreciable flow-bias errors by $O(R) \sim 1/h$; thus, the overall effects of the several types of errors tended to equalize at the same order of h, viz., $O(h^2)$ as in Equation (A85).

The argument that errors due to the artificial dissipation are of $O(h^2)$ combined with the lack of dependence on the average Δt seems to imply that these errors are of the form

$$a_1(t^n)h^2 + O(h^4),$$

where $a_1(t^n)$ does not depend upon either h or Δt; however, there may still be some question regarding flow-bias. Fortunately, this probably has little importance because errors caused by flow-bias are apparently much less than discretization errors. The evidence comes from comparing machine runs which differed in flow-bias.

The high accuracy with which total mass was conserved throughout all runs, even runs with *zero* flow-bias (cf. Figures A4 and A5), strongly indicates by itself that those errors (e.g., round-off) which grow with the number of time steps or vary with $\overline{\Delta t}$ must have been negligible. While the first two runs of Table AII differed in the time steps involved, they also differed in the level of flow-bias, as indicated in Table AIII where properties of the same two runs are set out. Thus, agreement of the first two runs in Table AII is evidence that the flow-bias has little effect on the calculated results, particularly on the volatile mass. Similar agreement has been found in the cases of higher-velocity collisions. Unfortunately, the argument still contains a weakness; e.g., after almost any reinitialization, the flow-bias [viz., ε_0 in Equation (A86)] had to be adjusted by trial and error until good overall conservation of energy was obtained in the large; apparently, some sort of nonlinear relationship exists between the flow-bias and Δt. The energy degradation shown in Table AIV may be another example of this relationship.

TABLE AIV

Calculated values for volatile mass with and without flow-bias resulting from a low-velocity head-on stellar collision

Flow-bias factor	Initial total energy	Final total energy	Leveling-off value of volatile mass
0.2	−0.137	−0.137	0.00530[a]
zero	−0.137	−0.144	0.00480[a]

[a] Machine units; e.g., $2M_\odot = 0.155$ machine units

Further evidence of insensitivity to flow-bias comes from comparing a pair of runs which had the same initialization except that the flow-bias was set to *zero* in one. The case treated involved the head-on collision between two solar-type stars initially approaching at a speed corresponding to *zero* relative velocity at infinite separation. The calculated results are given in Table AIV, where it may be seen that the run with *zero* flow-bias suffered a certain amount of energy degradation. The lowered value of total energy correlates with a smaller value of volatile mass (see also Table AV). Despite the unsatisfactory energy conservation, it is evident that, at least for volatile mass, errors due to flow-bias are considerably less than discretization errors or errors which depend upon the mesh width h (cf. Table AII and AIV). It is, of course, hoped that further insight into the effect of artificial dissipation will clarify the connection between flow-bias and energy conservation.

Incidentally, the fact that the summations yielding total mass [Equation (A84)] have been found to be independent of flow-bias (e.g., Figure A4) does not necessarily

TABLE AV

Numerical values indicating relative effects of flow-bias on (1) maximum density at the center of impact and (2) maximum total internal energy

Flow-bias ε_0	Mesh width h	Courant factor $\mathfrak{f}$	Values at time of maximum impact[a]				
			Time	Central density	Total energy	Kinetic energy	Internal energy
1.00	$R_\odot/20$	0.2	1.13	3.07	−0.135[b]	0.0581	0.364
0.20		0.5	1.15	3.06	−0.138[b]	0.0538	0.362
0.00		0.5	1.14	3.25	−0.144[b]	0.0563	0.367
1.00	$R_\odot/40$	0.25	1.10	3.43	−0.130[c]	0.0654	0.405
1.00	$R_\odot/60$	0.2	1.11	3.65	−0.131[c]	0.0608	0.428

[a] Values are expressed in machine units.
[b] Initial total energy −0.137.
[c] Initial total energy −0.136.

imply a similar situation for volatile mass. The reason has to do with the nature of the terms $\varrho^n_{i,j}\Delta V_{i,j}$. Noting that the $\varrho^n_{i,j}$ are calculated according to Equation (A94), it follows that, except for the initial values $\varrho^{n=1}_{i,j}$ and along the boundaries of the regions of summation, an overall cancellation of terms takes place upon an i-j summation. Hence, the values of Equations (A83) and (A84) are determined largely by the time summation of quantities along the boundaries of the i-j summation regions. This telescoping of terms involves both the artificial viscosity and the flow-bias. In the case of total mass, the inner boundaries (lower summation indices) become the axis of symmetry ($r=0$) and the lateral plane of symmetry ($z=0$) where cancellation is complete, leaving only the quantities on the outer boundary subject to flow-bias error. Because of the extremely low densities at the outer boundaries, it is understandable why the total mass is highly insensitive to flow-bias. In the case of volatile mass, however, the inner boundaries are not such as allow perfect cancellation of terms. Although the inner boundaries of volatile-mass summations [Equation (A83)] generally pass through regions of slow smooth flow which should not induce appreciable flow-bias, the boundary values are vulnerable to flow-bias errors through their domains of dependence.

(D) *Discretization errors* are essentially those errors which arise in the course of introducing a discrete or finite-difference representation of a system defined by a set of differential equations. Expressions for these errors can be derived using Taylor expansions with respect to an underlying vector function which is close to the limiting solution of the difference scheme as $\Delta r=\Delta z=h\to 0$ and $\Delta t\to 0$. However, this function may stop short of the limit in the sense that necessary derivatives must always exist. The expansions involved are of the form

$$\begin{pmatrix} X^{n+1/2}_{i,j+1/2} \\ \text{or} \\ X^{n+1/2}_{i,j-1/2} \end{pmatrix} = X(r_i, z_j, t^{n+1/2}) \pm X_z(r_i, z_j, t^{n+1/2})\cdot h/2 + 1/2! \times \\ \times X_{z^2}(r_i, z_j, t^{n+1/2})\cdot h^2/4 \pm 1/3!\, X_{z^3}(r_i, z_j, t^{n+1/2})\cdot h^3/8 + \ldots \qquad \text{(A91)}$$

where $X(r, z, t)$ represents the underlying function, which is very nearly the correct solution for the model being investigated.

The assumption of differentiability may not be any more demanding than the arguments used to set up the Lax-Wendroff difference method; i.e., the solution is imagined to be expandable (Lax and Wendroff, 1960) to the extent that

$$u(x, t + \Delta t) = u(x, t) + \Delta t\, u_t + 1/2!\,(\Delta t)^2\, u_{tt} + O(\Delta^3) \tag{A92}$$

and, wherever possible t derivatives are replaced by x derivatives from the basic differential equations

$$u_t + f_x = 0. \tag{A93}$$

If Equations (A92) and (A93) are used to set up a difference analogue, some dissipation seems to be implied so that variables are differentiable across what otherwise would be jump discontinuities, such as can occur in the solutions when the system represented by Equation (A93) is hyperbolic. Moreover, differencing must be consistent with the differential equations. Numerical solutions obtained in this way have an important property described by the following theorem (Lax and Wendroff, 1960): If as Δx and Δt tend to zero the resulting difference solution converges boundedly almost everywhere to some function, the function must be a weak solution of the differential system.

We shall first show that discretization errors in values of the principal dependent variables (ϱ, ϱu, ϱw, and P) calculated according to our difference scheme have the form of Equation (A85). Then, we shall extend these considerations to the discretization errors in the values of volatile mass.

Errors in Density and Other Principal Dependent Variables – In the current program, based on the Lax-Wendroff method, the density at an arbitrary netpoint i, j is calculated cumulatively according to the formula

$$\varrho_{i,j}^{n+1} = \varrho_{i,j}^{1} - \sum_{k=1}^{n} \frac{\Delta t^{k+1/2}}{(i-1)\,h^3} \left(A_{i+1/2,j}^{k+1/2} - A_{i-1/2,j}^{k+1/2} + B_{i,j+1/2}^{k+1/2} - B_{i,j-1/2}^{k+1/2}\right) \tag{A94}$$

where the quantities $A_{i+1/2,j}^{k+1/2}$ and $B_{i,j+1/2}^{k+1/2}$ have been defined by Equations (A33), (A36), and (A37); note, certain modifications are made in Equation (A94) for $i=1$, I and $j=1$, J (cf. Section 4 of Appendix).

The error in the calculated density $\varrho_{i,j}^{n+1}$ may be expressed by the deviation $\varrho_{i,j}^{n+1} - -\varrho(r_i, z_j, t^{n+1})$, where the lateral correction terms appearing in $A_{i+1/2,j}^{k+1/2}$ and $B_{i,j+1/2}^{k+1/2}$, e.g.,

$$\frac{h^2}{24}\,\frac{(\varrho u)_{i+1/2,j+1}^{k+1/2} - 2(\varrho u)_{i+1/2,j}^{k+1/2} + (\varrho u)_{i+1/2,j-1}^{k+1/2}}{h^2},$$

make the difference operator more correct; while, the flow-bias and the artificial viscosity are considered part of the numerical error. Significant properties of $\varrho_{i,j}^{n+1} -$

$-\varrho(r_i, z_j, t^{n+1})$ are demonstrated below by an argument which combines induction with observed behavior of the numerical calculations.

Starting with the induction argument, suppose that at time t^n the components ϱ, ϱu, ϱw, and P of the vector function X satisfy the relation

$$X^n_{i,j} = X(r_i, z_j, t^n) + a(r_i, z_j, t^n)\cdot h^2 + O(h^4) \tag{A95}$$

where $X^n_{i,j}$ is the value calculated by the difference scheme using mesh width h; and, $X(r_i, z_j, t^n)$ denotes the solution of the difference scheme as h and Δt approach zero. In the spirit of the aforementioned theorem of Lax and Wendroff, $X(r, z, t)$ is conjectured to be very nearly a correct solution (or correct weak solution) of the basic system of equations.

Denoting the difference operator corresponding to our numerical program by $f(X^n_{l,m}, h, \Delta t)$, we proceed to advance $\varrho(r_i, z_j, t^n)$, the ϱ component of the correct solution, compensating for errors in the difference operator by means of Taylor expansions like Equation (A91) as well as similar expansions with respect to Δt. An essential property of these expansions is that, since they are based strictly on the ideal solution $X(r, z, t)$ and its derivatives, the resulting correction terms are independent of both h and Δt. Thus, the following expression is obtained:

$$\begin{aligned}
\varrho(r_i, z_j, t^{n+1}) = {} & \varrho(r_i, z_j, t^n) + f(X(r_l, z_m, t^n), h, \Delta t) - \\
& - \frac{\Delta t^{n+1/2}}{(i-1)\,h}\{(i-\tfrac{1}{2})\,\varepsilon^n_{x,j}[(\varrho u)^{n+1/2}_{i+1/2,j} - (\varrho u)^n_{x,j}] - \\
& - (i-\tfrac{3}{2})\,\varepsilon^n_{x',j}[(\varrho u)^{n+1/2}_{i-1/2,j} - (\varrho u)^n_{x',j}] + (i-1)\,\varepsilon^n_{i,y} \times \\
& \times [(\varrho w)^{n+1/2}_{i,j+1/2} - (\varrho w)^n_{i,y}] - (i-1)\,\varepsilon^n_{i,y'}[(\varrho w)^{n+1/2}_{i,j-1/2} - (\varrho w)^n_{i,y'}]\} - \\
& - h^2\kappa_0\frac{\Delta t^{n+1/2}}{(i-1)\,h}\left\{(i-\tfrac{1}{2})\frac{|u^n_{i+1,j} - u^n_{i,j}|}{h}\frac{(\varrho^n_{i+1,j} - \varrho^n_{i,j})}{h} - \right. \\
& - (i-\tfrac{3}{2})\frac{|u^n_{i,j} - u^n_{i-1,j}|}{h}\frac{(\varrho^n_{i,j} - \varrho^n_{i-1,j})}{h} + (i-1)\frac{|w^n_{i,j+1} - w^n_{i,j}|}{h} \times \\
& \times \frac{(\varrho^n_{i,j+1} - \varrho^n_{i,j})}{h} - \left.(i-1)\frac{|w^n_{i,j} - w^n_{i,j-1}|}{h}\frac{(\varrho^n_{i,j} - \varrho^n_{i,j-1})}{h}\right\} + \\
& + \frac{h^2}{6}\Delta t^{n+1/2}\left[\frac{1}{r}(r\varrho u)_{r^3} + (\varrho w)_{z^3}\right]^n_{i,j} + \frac{(\Delta t^{n+1/2})^3}{6}[\varrho_{t^3}]^n_{i,j} - \frac{h^2}{48} \times \\
& \times (\Delta t^{n+1/2})^2\,\frac{1}{h}\left(\frac{i-\frac{1}{2}}{i-1}C^n_{i+1/2,j} - \frac{i-\frac{3}{2}}{i-1}C^n_{i-1/2,j} + D^n_{i,j+1/2} - D^n_{i,j-1/2}\right) + \\
& + \frac{(\Delta t^{n+1/2})^4}{48}[\varrho_{t^4}]^n_{i,j} + \frac{h^4}{320}\Delta t^{n+1/2}\left[\frac{1}{r}(r\varrho u)_{r^5} + (\varrho w)_{z^5}\right]^n_{i,j} + \\
& + \frac{(\Delta t^{n+1/2})^5}{320}[\varrho_{t^5}]^n_{i,j} + \cdots,
\end{aligned} \tag{A96}$$

where $y_{x^n} \equiv \partial^n y/\partial x^n$ and

$$C^n_{i+1/2,j} = \left[\frac{1}{r}(r\varrho u^2)_{r^3} + 3(\varrho uw)_{r^2z} + 4(\varrho uw)_{z^3} + P_{r^3} - \varrho\Phi_{r^3} - 3\varrho_{r^2}\Phi_r\right]^n_{i+1/2,j} \tag{A97}$$

$$D^n_{i,j+1/2} = [4(\varrho wu)_{r^3} + 3(\varrho wu)_{rz^2} + (\varrho w^2)_{z^3} + P_{z^3} - \varrho\Phi_{z^3} - 3\varrho_{z^2}\Phi_z]^n_{i,j+1/2}\,. \tag{A98}$$

Note that in Equation (A96) the correct solution $X(r_l, z_m, t^n)$ is subject to the difference operator rather than the numerical solution $X^n_{l,m}$. Moreover, the terms involving $\varepsilon^n_{x,j}$, $\varepsilon^n_{x',j}$, etc. originate from the flow-bias; while, the factor κ_0 identifies the artificial viscosity defined by Equations (A69). The quantity

$$\frac{h^2}{6}\Delta t^{n+1/2}\left[\frac{1}{r}(r\varrho u)_{r^3} + (\varrho w)_{z^3}\right]^n_{i,j}$$

is one of the principal error terms arising from Taylor expansions about the correct solution; when written out more carefully it becomes

$$\frac{h^2}{8}\Delta t^{n+1/2}\left(\frac{1}{3}\left[\frac{1}{r}(r\varrho u)_{r^3} + (\varrho w)_{z^3}\right](r_i, z_j, t^{n+1/2}) + \right.$$
$$+\frac{1}{h}\left\{\frac{i-\frac{1}{2}}{i-1}[(\varrho u)_{r^2}](r_{i+1/2}, z_j, t^n) - \frac{i-\frac{3}{2}}{i-1}[(\varrho u)_{r^2}](r_{i-1/2}, z_j, t^n) + \right.$$
$$\left.\left. + [(\varrho w)_{z^2}](r_i, z_{j+1/2}, t^n) - [(\varrho w)_{z^2}](r_i, z_{j-1/2}, t^n)\right\}\right),$$

where evaluation at $t^{n+1/2}$ implies use of one or more of the Equations (A56) through (A61).

The relationship between $\Delta t^{n+1/2}$ and $\Delta r = \Delta z = h$ remains as before [cf. Equation (A70)], viz.,

$$\Delta t^{n+1/2} = \mathfrak{f}h/(\hat{s})^n \tag{A99}$$

where

$$(\hat{s})^n = \{\max_{i,j}[(u^n_{i,j})^2 + (w^n_{i,j})^2 + P^n_{i,j}/\varrho^n_{i,j}]\}^{1/2} \tag{A100}$$

and $\mathfrak{f}$ is usually either 0.2, 0.25, or 0.5. In practice it turns out that

$$\Delta t^{n+1/2} \lesssim \tfrac{1}{10}h/\bar{s}^n \tag{A101}$$

where

$$\bar{s}^n = \{\operatorname{ave}_{i,j}[(u^n_{i,j})^2 + (w^n_{i,j})^2 + P^n_{i,j}/\varrho^n_{i,j}]\}^{1/2}\,. \tag{A102}$$

The above condition suggests that, as the error terms of Equation (A96) accumulate cycle after cycle, those with higher powers of $\Delta t^{n+1/2}$ contribute relatively little to the overall error.

Empirical evidence verifies the conjecture that terms containing $(\Delta t)^m$, where $m>1$, make up only a small part of the total error. For, if such terms were important, the numerical results would exhibit a dependence upon the sizes of the time steps; i.e., on n, the number of cycles needed to bring a calculation up to a certain point in time; moreover, this effect would be particularly apparent when other factors are held constant. However, calculations on the same initial-value problem are found

to be sensibly independent of n (e.g., Table AII), although their results do vary with the spatial increment h. Consequently, we neglect terms containing Δt raised to a power greater than one.

Having worked out an expression for $\varrho(r_i, z_j, t^{n+1})$, viz. Equation (A96), consider an analogous expression for the numerical quantity $\varrho_{i,j}^{n+1}$. In the difference program, the density is advanced by a formula such as

$$\varrho_{i,j}^{n+1} = \varrho_{i,j}^{n} + f(X_{i,m}^{n}, h, \Delta t) \tag{A103}$$

Subtracting Equation (A96) from the above yields

$$\begin{aligned}\varrho_{i,j}^{n+1} - \varrho(r_i, z_j, t^{n+1}) = \varrho_{i,j}^{n} - \varrho(r_i, z_j, t^{n}) \\ + f(X_{l,m}^{n}, h, \Delta t) - f(X(r_l, z_m, t^{n}), h, \Delta t) \\ + \text{flow-bias} + \text{artificial viscosity} \\ + \Delta a(r_i, z_j, t^{n})\, h^2 + \Delta t^{n,+1/2}\, O(h^4)\end{aligned} \tag{A104}*$$

in which

$$\Delta a(r_i, z_j, t^{n}) = -\frac{\Delta t^{n+1/2}}{6}\left[\frac{1}{r}(r\varrho u)_{r^3} + (\varrho w)_{r^3}\right]_{i,j}^{n}. \tag{A105}*$$

But, strong empirical evidence has already been presented to the effect that any appreciable contribution due to flow-bias and artificial viscosity is of the form

$$a_1(t^{n})\, h^2 + \boldsymbol{O}(h^4)$$

Moreover, if Equation (A95) is true at some time step n, then the group of terms $\varrho_{i,j}^{n} - \varrho(r_i, z_j, t^{n}) + f(X_{l,m}^{n}, h, \Delta t) - f(X(r_l, z_m, t^{n}), h, \Delta t)$ must also be of the form

$$a_2(t^{n})\, h^2 + O(h^4)$$

Therefore, if Equation (A95) holds at some time step n, it follows from Equation (A104) that at the next time step

$$\varrho_{i,j}^{n+1} = \varrho(r_i, z_j, t^{n+1}) + a(r_i, z_j, t^{n+1})\, h^2 + O(h^4) \tag{A106}$$

and, similarly for other components of the vector function X. The argument is completed by noting that Equation (A95) is true initially viz.,

$$X_{i,j}^{n=1} = X(r_i, z_j, 0) \tag{A107}$$

hence, by induction Equation (A95) holds for all time steps.

Discretization errors in volatile mass arise from (1) the cumulative effect of errors in values of the density $\varrho_{i,j}^{n}$ and (2) inaccuracies in determining the limits of summation [cf. Equation (A83)]. The first contribution must be of the form of Equation (A85) since it has been shown that errors in the $\varrho_{i,j}^{n}$ are of this form, any possible exceptions due to flow-bias are ruled out by empirical evidence that the effects of flow-bias are relatively small, at least in values of volatile mass.

* Explicit display of $\Delta t^{n+1/2}$ is consistent with the correspondence of Equation (A94) to a time integral.

The limits of summation in Equation (A83) are a finite-difference representation of the boundaries of the volatile regions, and as such include all the volatile-mass elements and no more, a mass element $\varrho^n_{i,j}\Delta V_{i,j}$ being considered volatile or energetically capable of escape from gravitational binding if

$$F^n_{i,j} = \{[(\varrho u)^n_{i,j}]^2 + [(\varrho w)^n_{i,j}]^2\}/2\varrho^n_{i,j} + P^n_{i,j}/(\gamma - 1) - \varrho^n_{i,j}\Phi^n_{i,j} > 0, \quad \text{(A108)}$$

where the $(\varrho u)^n_{i,j}$ and $(\varrho w)^n_{i,j}$ are set to zero unless both fluid velocity components u and w are directed outwards. The present considerations concern late stages of collision calculations, when the numerical values of volatile mass have largely leveled off and there exists only one simply-connected region per quadrant of space which contains all the volatile-mass elements of that quadrant. Then, the lower summation limits in Equation (A83) definitely correspond to the inner boundary of the volatile region, the upper limits to the outer boundary. At this stage of a stellar-collision calculation, imagine the values of $F^n_{i,j}$ to be points on a surface $F(r, z, t)$ in the three-dimensional space r, z, F. The calculations place F below the r-z plane for small values of r, z and above for large values. In any quadrant, the intersection of F and the r-z plane determines the inner boundary of the volatile region; while, the outer boundary of this region coincides with the moving surface of the stellar fluid itself. In fact late in a collision calculation, the outer boundaries (the upper limits of summation) for the volatile-mass sum are largely identical with those of the total-mass sum, the only dissimilarity being that the upper limits for volatile mass do not always include the entire outer surface. As in considerations involving flow-bias, the fact that total mass remains highly constant during all numerical calculations implies that effects due to the upper limits of summation must be negligible. For, if such errors were appreciable, they certainly would have appeared sometime or somewhere as a degradation in total-mass conservation. The effects of the lower limits, however, remain to be investigated; and, an approximate formula will be derived for estimating the errors due to small shifts in the lower boundary of the volatile region.

Consider the upper righthand quadrant of the r-z plane, and successively number the netpoints composing the inner boundary of the volatile region in this quadrant starting from a convenient initial point on the z-axis and proceeding clockwise around the boundary. Let the index for this boundary sequence be $\sigma = 1, 2, \cdots$, where each value of σ implies a netpoint i_σ, j_σ and a pair of coordinates r_σ, z_σ. In the late stages of a calculation the boundary sequence can be made to enclose the entire gravitative *non*-volatile region, and the area S of this region is given by

$$S = \tfrac{1}{2}\left[z_1 h + \sum_{\sigma>1} z_\sigma (r_{\sigma+1} - r_{\sigma-1})\right], \quad \text{(A109)}$$

while to a good approximation the corresponding volume of revolution is

$$\zeta \simeq \pi\left[z_1 h^2/4 + \sum_{\sigma>1} r_\sigma z_\sigma (r_{\sigma+1} - r_{\sigma-1})\right] \quad \text{(A110)}$$

which now embraces the upper half of the r-z space.

Small variations in the inner boundary of the volatile region might be expressed most simply by a change of coordinates $r_\sigma, z_\sigma \rightarrow r_\sigma, z_\sigma + \delta z_\sigma$, the number of boundary points and their r-coordinates being held fixed as a first approximation. Then, according to Equation (A110), the corresponding variation in volume and in volatile mass respectively would be approximately given by the following summations, where from now on the upper summation limit is considered truncated at some $\sigma(\max)$ beyond which no variations in the r_σ, z_σ take place: namely,

$$\delta\zeta \simeq + 2\pi h^2 \left[\delta z_1/8 + \sum_{\sigma>1} (i_\sigma - 1)\, \delta z_\sigma\right] \tag{A111}$$

and for the full r-z space

$$\delta M_v \simeq - 4\pi h^2 \left[\varrho_1 \delta z_1/8 + \sum_{\sigma>1} (i_\sigma - 1)\, \varrho_\sigma \delta z_\sigma\right]. \tag{A112}$$

The latter enables us to estimate the magnitude of the error due to uncertainties in summation limits.

Let the first step involving Equation (A112) be an identification of the δz_σ with the probable position errors of points determining the inner boundary of the volatile region, as this exists in the later stages of head-on stellar-collision calculations. It has been found empirically in such calculations that the location of the inner boundary is generally insensitive to mesh width h; e.g., upon comparing two runs identical except that $h = h_1 = R_\odot/20$ in one and $h = h_2 = R_\odot/40$ in the other, the locations of the inner boundaries agree within $\sim h_2$, at least, during later periods of the calculations. Such observations are interpreted to mean that

$$|\delta z_\sigma| \sim h \tag{A113}$$

and, hence, the corresponding error $|\varepsilon_m|$ in volatile mass is estimated to be approximately

$$|\varepsilon_m| \simeq 4\pi h^3 \left[\tfrac{1}{8} + \sum_{\sigma>1} (i_\sigma - 1)\right] \bar{\varrho}\,, \tag{A114}$$

where $\bar{\varrho}$ denotes a sort of weighted average density along the inner boundary of the volatile region. Note however that, if the variation of ϱ_σ with σ is appreciable, points with larger i_σ would be favored.

For a pair of runs which represent a head-on stellar collision starting from *zero* relative velocity at infinite separation (cf. Table AII), it turns out that

$$h_1 = R_\odot/20, \quad M_v = 0.005\,30, \quad |\varepsilon_m| \lesssim 0.0008$$

and

$$h_2 = R_\odot/40, \quad M_v = 0.007\,00, \quad |\varepsilon_m| \lesssim 0.000\,28\,.$$

Particularly in the case of h_2, the above values of $|\varepsilon_m|$ are much smaller than the observed variations with h.

If it is not admissible to neglect the errors due to inaccurate summation limits, a relationship can be set up between the δz_σ of Equation (A112) and variations in

the surface $F(r, z, t)$, whose intersection with the r-z plane determines the curve which the variable part of the boundary sequence $\sigma = 1, 2, \cdots$ represents numerically. A variation δF in the neighborhood of the curve of intersection would cause this to shift by an amount

$$\delta s = \delta F / (F_r^2 + F_z^2)^{1/2}, \tag{A115}$$

or in terms of components along the r and z directions

$$\delta r = -\,\delta F\, F_r / (F_r^2 + F_z^2)$$

and

$$\delta z = -\,\delta F\, F_z / (F_r^2 + F_z^2). \tag{A116}$$

The minus signs are appropriate because the shift is opposite the small displacement which when multiplied by ∇F yields the change in F. A continuous variation δF near the curve of intersection would generate a strip-like area which is a measure of the change in the region of summation.

According to the defining equation for F [viz., Equation (A108)], a small variation in F is a function of the small variations in the variables ϱ, ϱu, ϱw, and P. If variations of these variables are associated with numerical errors, they should be of the form

$$\delta X_{i,j}^n = a(r_i, z_j, t^n)\, h^2 + O(h^4), \tag{A117}$$

Hence, we can write

$$\delta F = a_F h^2 + O(h^4), \tag{A118}$$

and then by Equations (A116)

$$\delta z = a_z h^2 + O(h^4), \tag{A119}$$

where the above relations apply to a small shift in the curve of intersection between the surface F and the r-z plane. Because of their origin, the coefficients of h^2 in Equations (A118) and (A119) are sensibly independent of both h and Δt. Before these values of, say, $\delta z_{i,j}$ can be identified with the δz_σ in Equation (A112) a certain discretization must be performed; i.e.,

$$\begin{aligned} \delta z_\sigma &= h \left[\frac{\delta z_{i_\sigma, j_\sigma}}{h} \right] \\ &= h \left[-\,F_z \delta F_{i_\sigma, j_\sigma} / h (F_r^2 + F_z^2) \right]; \end{aligned} \tag{A120}$$

the brackets denoting truncation down to the nearest integer. Given a fine enough network of points so that the above considerations are statistically meaningful, the combination of Equations (A112) and (A120) would imply that

$$\varepsilon_m = a_2(t^n)\, h^2 + O(h^4), \tag{A121}$$

where ε_m denotes the error in volatile mass due to uncertainties in the limits of summation. However, as illustrated by the estimates obtained using Equation (A112), this component of error generally tends to be relatively small.

The above discussion completes the argument that discretion errors in our calculated values of volatile mass are of the form expressed by Equation (A85).

Order of Magnitude of Discretization Errors. – Having justified the formula

$$M_v^n = M_v(t^n) + a(t^n)\,h^2 + O(h^4), \tag{A85}$$

where M_v^n denotes the numerical value of volatile mass at time t^n and $M_v(t^n)$ the correct value, consider an estimate of the error terms $a(t^n)\,h^2$ and $O(h^4)$. Some appreciation for these may be gained by fitting an expression of the form

$$x_i = x + ah_i^2 + bh_i^4 \tag{A122}$$

to the numerically-determined results listed in Table AII; i.e., results from stellar-collision calculations using mesh widths $h_1 = R_\odot/20$, $h_2 = R_\odot/40$, and $h_3 = R_\odot/60$. This procedure is valid to the extent that the coefficients of h^2 and h^4 can be treated as being independent of both h and the time steps Δt. Incidentally, the run with h_3 remains incomplete because of the large machine expense that would have been necessary for its completion.

The variables whose h-variations were fitted to Equation (A122) are: (1) maximum density at the center of impact, (2) maximum total internal energy, and (3) the volatile mass prior to leveling off. The first two are evaluated at maximum compression; however, the justification that their numerical values satisfy an expression like Equation (A85) may be less convincing than in the case of the leveling-off value of volatile mass. The uncertainty arises because of the effects of flow-bias in certain regions lying near the center of impact where incoming fluid is sharply decelerated during compression. This process takes place for a time starting just after first contact between the colliding objects and continues just beyond maximum compression, but its duration is much less than the time required to achieve leveling-off in the volatile mass. Each run is affected similarly regardless of mesh width h or Δt.

Support for the view that cumulative flow-bias errors are generally small comes from examining runs having *zero* or very little flow-bias, although the strength of the evidence is compromised by a failure of these runs to satisfy the conservation of energy. Certain details with and without flow-bias are shown in Table AV, where it is seen that variations with respect to h are much greater than changes resulting from the different levels of flow-bias. It should be noted that, since the flow-bias level is essentially controlled by the product of terms $\frac{1}{2}\varepsilon_0|u_{x,j}^n|\Delta t^{n+1/2}/h = \frac{1}{2}\varepsilon_0\tilde{f}|u_{x,j}^n|/(\hat{s})^n$ [cf. Equations (A86) and (A87)], the largest change in flow-bias occurred when ε_0 was dropped from 0.20 to 0.00 while holding $h = R_\odot/20$ and $\tilde{f} = 0.5$.

If the three maximum densities obtained from Table AII for $h_1 = R_\odot/20$, $h_2 = \frac{1}{2}h$, and $h_3 = \frac{1}{3}h_1$ are substituted successively into Equation (A122), three simultaneous equations result; i.e.,

$$\begin{aligned} 3.07 &= x + ah_1^2 + bh_1^4, \\ 3.56 &= x + \tfrac{1}{4}ah_1^2 + \tfrac{1}{16}bh_1^4, \\ 3.93 &= x + \tfrac{1}{9}ah_1^2 + \tfrac{1}{81}bh_1^4, \end{aligned} \tag{A123}$$

which yield when solved for x, ah_1^2, and bh_1^4

$$\begin{aligned} x &= +4.289, \\ ah_1^2 &= -3.481, \\ bh_1^4 &= +2.262; \end{aligned} \tag{A124}$$

the units being such that the initial central density of the solar-like stellar model is unity. From a similar set of relations for maximum internal energy, one obtains the following values expressed in terms of machine units:

$$\begin{aligned} x &= +0.4499, \\ ah_1^2 &= -0.2107, \\ bh_1^4 &= +0.1248. \end{aligned} \tag{A125}$$

If $E(\max)$ is introduced to denote the maximum internal energy of the system and the above numbers are transformed into *ergs*, the values of Equations (A125) become

$$\begin{aligned} E(\max) &= +1.884 \times 10^{+49} \text{ ergs}, \\ ah_1^2 &= -0.8824 \times 10^{+49} \text{ ergs}, \\ bh_1^4 &= +0.5227 \times 10^{+49} \text{ ergs}, \end{aligned} \tag{A126}$$

where the computational error in $E(\max)$, considered our best value for the maximum internal energy in the course of a *zero* initial-velocity collision, is somewhat less than $ah_3^2 + bh_3^4 = -0.092 \times 10^{+49}$ ergs.

For the case of the volatile mass at a certain time prior to leveling off, the solution of the three simultaneous equations obtained by substituting values from Table AII into Equation (A122) is

$$\begin{aligned} x &= +0.006\,16, \\ ah_1^2 &= -0.010\,50, \\ bh_1^4 &= +0.005\,54: \end{aligned} \tag{A127}$$

here the units are such that 0.155 equals $2M_\odot$. Of the three, (1) maximum central density, (2) maximum internal energy, or (3) early volatile mass, the latter is subject to greatest uncertainties, perhaps because it falls on the rapidly rising part of the curve of volatile mass *vs.* time where the program is being required to handle large dynamic changes.

Convergence of the error terms is certainly poor for the coarse-zoned calculations (viz., $h = h_1 = R_\odot/20$), suggesting that this mesh size does not include enough detail. When $h = h_2 = \frac{1}{2}h_1$ or better still $h = h_3 = \frac{1}{3}h_1$, the error terms are more acceptable, in the case of $h_3 = \frac{1}{3}h_1$, for maximum density

$$\begin{aligned} x &= +4.289, \\ ah_3^2 &= -0.387, \\ bh_3^4 &= +0.028; \end{aligned} \tag{A128}$$

and for maximum internal energy

$$\begin{aligned} x &= +\,0.4499\,, \\ ah_3^2 &= -\,0.0234\,, \\ bh_3^4 &= +\,0.0015\,. \end{aligned} \tag{A129}$$

It would be convenient to be able to identify the above values of x with correct values, but they still contain an unknown margin of error. Some measure of this residual error might be obtained if it were possible to evaluate the terms x_0, $a_0h_i^2$, $b_0h_i^4$, and $c_0h_i^6$ of the higher-order expansion

$$x_i = x_0 + a_0h_i^2 + b_0h_i^4 + c_0h_i^6\,. \tag{A130}$$

But, this would require results from a run at yet another mesh width; e.g., $h_4 = \frac{1}{4}h_1$. While such results are not available, an attempt has been made to locate the upper and lower bounds for reasonable extrapolations of maximum central density and maximum internal energy to the smaller mesh width $h = \frac{1}{4}h_1$. From bounds thus estimated, together with the numerical results for h_1, h_2, and h_3, a corresponding range of values for x_0 has been calculated. Then assuming that $x_0\,(\min) \lesssim x \lesssim x_0\,(\max)$, we write for maximum density at center of impact

$$x = +\,4.29 \pm 0.12 \tag{A131}$$

and for maximum internal energy

$$\begin{aligned} &x = +\,0.450 \pm 0.007 \\ \text{or} \qquad &E(\max) = +\,(1.88 \pm 0.03) \times 10^{+49}\ \text{ergs}\,. \end{aligned} \tag{A132}$$

Taking the above values of x as standard, consider the degree of improvement obtainable by applying Richardson's method (cf. Forsythe and Wasow, 1960; Isaacson and Keller, 1966; et al.) to pairs of results from calculations with mesh widths $h_1 = R_\odot/20$ and $h_2 = \frac{1}{2}h_1$. This question is interesting because calculations of the leveling-off values of volatile mass are only available for mesh widths h_1 and h_2, and from these the best possible values should be obtained. Since the coefficient $a(t^n)$ in Equation (A85) is sensibly independent of both mesh width h and the time steps Δt, the error term $a(t^n)h^2$ can be eliminated using the results of two runs which are identical except for mesh width; this is the essence of Richardson's method for deferred extrapolation to zero mesh width. When the error terms satisfy Equation (A85), the formula for the improved value is

$$\tilde{x} = (4x_2 - x_1)/3\,, \tag{A133}$$

where x_2 denotes the result for mesh width $h_2 = \frac{1}{2}h_1$ and x_1 for $h = h_1$.

On the other hand in the case of the quantities which have been fitted to Equation (A122), x is the best value available; moreover, a relationship exists between x and the $\tilde{x}$ defined above; i.e.,

$$\tilde{x} = (4x_2 - x_1)/3 = x - bh_1^4/4\,. \tag{A134}$$

Let x be taken as a sort of standard; then the error in $\tilde{x}$ is $bh_1^4/4$, and the results according to Richardson's method are:

$$\begin{aligned} &\varrho(\max) = +\,3.72^{+0.57}_{-0.00} \quad \text{mach. units}, \\ &E(\max) = +\,0.419^{+0.031}_{-0.000} \quad \text{mach. units}; \\ \text{or} \quad &E(\max) = (1.754^{+0.130}_{-0.000}) \times 10^{+49} \ \text{ergs}, \\ &M_v(\text{early}) = +\,0.0048^{+0.0014}_{-0.0000} \quad \text{mach. units}. \end{aligned} \tag{A135}$$

The errors quoted come directly from Equation (A134); and, the improvement gained by Richardson's method can be gauged by comparing $bh_1^4/4$ in each case with $ah_2^2+bh_2^4$, the latter being the error in x_2. For the case of $\varrho(\max)$, $bh_1^4/4=0.57$ and $ah_2^2+bh_2^4=-0.73$; for $E(\max)$, $bh_1^4/4=0.031$ and $ah_2^2+bh_2^4=-0.045$; while for $M_v(\text{early})$, $bh^4/_1^4=0.0014$ and $ah_2^2+bh_2^4=-0.0023$.

Thus, by analyzing the changes with respect to mesh width h, we are able to acquire some idea of the magnitudes of the discretization errors contained in our current numerical results, which rely for the most part on calculations using only the two mesh widths $h=h_1=R_\odot/20$ and $h=h_2=R_\odot/40$.

Acknowledgments

The computer programming was initially carried out by (Mrs) Judith A. Copeland. Her work was outstanding. Later, the principal programming details were assumed by Lewis Nowitz, who subsequently contributed significant refinements and improvements. Early in the total effort, a basic-assembly-language subroutine was developed by Paul Schneck for the purpose of achieving more rapid calculations of the gravitational potentials. The routine for generating displays of the fluid-velocity fields by means of many small arrows was written by George Kleiner. Improvements in these displays have been made by Lewis Nowitz and Jonathan Levi. We are most grateful to these people for their contributions. It is also a great pleasure to thank Dr Arnold Lapidus, and other colleagues at Programming Methods Inc., for many helpful discussions.

References

Chandrasekhar, S.: 1939, *Stellar Structure*, Dover Publications, New York.
Courant, R., Friedrichs, K. O., and Lewy, H.: 1928, *Math. Ann.* **100**, 32.
English transl. 1967, *IBM J. Res. Develop.* **11**, 215.
Courant, R. and Hilbert, D.: 1962, *Methods of Mathematical Physics*, Vol. II, *Partial Differential Equations*, Interscience Pub., New York.
Forsythe, G. E. and Wasow, W. R.: 1960, *Finite-Difference Methods for Partial Differential Equations*, John Wiley and Sons, New York.
Isaacson, E. and Keller, H. B.: 1966, *Analysis of Numerical Methods*, John Wiley and Sons, New York.
Kasahara, A. and Houghton, D. D.: 1969, *J. Comp. Phys.* **4**, 377.
Kreiss, H. O.: 1964, *Comm. Pure Appl. Math.* **17**, 335.

Kreiss, H. O.: 1966a, *Numerical Solution of Partial Differential Equations* (ed. by J. H. Bramble), Academic Press, New York, p. 51.
Kreiss, H. O.: 1966b, *Numerical Solutions of Nonlinear Differential Equations* (ed. by D. Greenspan), John Wiley and Sons, New York, p. 141.
Kreiss, H. O.: 1968, *Math. Comp.* **22**, 703.
Landau, L. D. and Lifshitz, E. M.: 1959, *Fluid Mechanics*, Pergamon Press, London.
Lapidus, A.: 1967, *J. Comp. Phys.* **2**, 154.
Lax, P. D.: 1954, *Comm. Pure Appl. Math.* **7**, 159.
Lax, P. D.: 1957, *Comm. Pure Appl. Math.* **10**, 537.
Lax, P. D. and Wendroff, B.: 1960, *Comm. Pure Appl. Math.* **13**, 217.
Lax, P. D. and Wendroff, B.: 1964, *Comm. Pure Appl. Math.* **17**, 381.
Neumann, J. von and Richtmyer, R. D.: 1950, *J. Appl. Phys.* **21**, 232.
Richtmyer, R. D.: 1962, *A Survey of Difference Methods for Non-Steady Fluid Dynamics*, NCAR Tech. Note 63-2, Nat' 1 Center for Atmos. Res., Boulder, Colo.
Richtmyer, R. D., and Morton, K. W.: 1967, *Difference Methods for Initial-Value Problems*, Interscience Pub., New York.
Strang, G.: 1964, *Num. Math.* **6**, 37.
Zel'dovich, Y. B. and Raizer, Y. P.: 1967, *Physics of Shock Waves and High-Temperature Hydrodynamic Phenomena*, Vol. II (ed. by W. D. Hayes and R. F. Probstein), Academic Press, New York.